Stony Brook University

Numerical Modeling of Hydrodynamic Instabilities and their Impact on Mix in Inertial Confinement Fusion

A Dissertation Presented

by

Jeremy Melvin

to

The Graduate School

In Partial Fulfillment of the

Requirements

for the Degree of

Doctor of Philosophy

in

Applied Mathematics and Statistics

Stony Brook University

August 2016

Stony Brook University

The Graduate School

Jeremy Melvin

We, the dissertation committee for the above candidate for the
Doctor of Philosophy degree, hereby recommend
acceptance of this dissertation.

James Glimm - Dissertation Advisor

Distinguished Professor, Department of Applied Mathematics and Statistics

Xiangmin Jiao - Chairperson of Defense

Associate Professor, Department of Applied Mathematics and Statistics

Roman Samulyak - Member

Professor, Department of Applied Mathematics and Statistics

Michael Zingale - Outside Member

Associate Professor, Department of Physics and Astronomy

This dissertation is accepted by the Graduate School.

Charles Taber

Dean of the Graduate School

Abstract of the Dissertation

Numerical Modeling of Hydrodynamic Instabilities and their Impact on Mix in Inertial Confinement Fusion

by

Jeremy Melvin

Doctor of Philosophy

in

Applied Mathematics and Statistics

Stony Brook University

2016

The simulation campaign to model Inertial Confinement Fusion (ICF) capsules has come a long way since experiments with the potential to achieve net energy gain began in 2010. A remaining area of uncertainty is the modeling of instability growth and mixing of ablator material into the core, degrading the capsules. We explore the instability growth by applying techniques that have led to a proven track record of validation: the addition of a front tracking (FT) algorithm and physical diffusion models.

For the first time, we have integrated our FT algorithm through an API into an external Rad-Hydro code FLASH, from the University of Chicago. With FT coupled into a code capable of simulating ICF experiments with a full suite of physics, we conduct a parameter study on 2D simulations in spherical geometry to explore the impact FT has on modeling the instability growth. We find the instability growth during the shock generated Richtmyer-Meshkov phase is suppressed by a lingering capsule acceleration, providing a stabilizing mechanism. Thus, FT does not impact the growth of these instabilities, since they are suppressed. We find the late time deceleration phase Rayleigh-Taylor instabilities are strongly radially dependent, occurring at inner regions of the shell, but not reaching the ablator-fuel interface. In an Eulerian simulation methodology, numerical diffusion of ablator

material into the fuel is shown to penetrate far enough on reasonable computational grids, that strong instability growth captures it, amplifying the mixing. With FT coupled in, this numerical diffusion is prevented. We analyze simulations with a physical diffusion model coupled into the hydro equations to represent a physically consistent penetration of ablator material.

To capture these effects, a 1D Buoyancy-Drag analysis is proposed to model the penetration of ablator material and amplification due to instability growth. We compare the 1D model, analyzed off a 1D simulation, to actual growth observed in the 2D simulations, to explore the predictive capabilities of this model. We find that ICF capsules are stable but near a performance cliff where small perturbations or coupling effects between different instability drivers has the potential to cause enough of a change in the dynamics to allow ablator material to penetrate into the hot spot. In closing, we discuss the impact of a lack of physical diffusion and FT models on the current state of ICF simulations.

To my family and friends

Table of Contents

List of Figures

List of Tables

Acknowledgments

I want to first and foremost thank my advisor Professor James Glimm. His guidance and encouragement has been invaluable during my studies. His dedication and enthusiasm for his research will forever motivate me to work harder. I am honored to have been his student and have learned a great deal from him.

I also want to thank Professor Roman Samulyak, Professor Xiangmin Jiao and Professor Michael Zingale for being on my dissertation committee.

I would like to thank Dr. Baolian Cheng, who has been a mentor for my research and my career. Also, Dr. David Sharp, whose guidance and ideas have helped to focus my work. I also owe a great deal to Dr. Doug Wilson, Dr. Marty Marinak and Dr. Dan Clark for their help with getting access to and running HYDRA.

I want to thank Los Alamos National Lab who have supported my research through Contract No. JL3K00 NYSB0000, Inertial Confinement Fusion Campaign.

I also want to thank all my fellow group members and colleagues throughout these years who have helped me when I got stuck and provided fresh perspectives on my work. I would like to especially thank Pooja Rao, HyunKyung Lim and Verinder Rana who I have worked most closely with and learned a great deal from.

Lastly, I want to thank my family, whose support has always kept me grounded and who have always been there for me.

Chapter 1

Introduction

Inertial Confinement Fusion (ICF) is an approach to fusion in which a small plastic capsule typically filled with Deuterium and Tritium isotopes (DT) is strongly compressed, until temperatures and densities rise enough to generate a self-sustaining fusion burn which produces a net energy gain [42]. ICF first began being heavily studied as a possible approach to generating energy back in the late 1950s and early 1960s, through work done at Lawrence Livermore National Laboratory (LLNL) by John Nuckolls [56]. Over the decades that followed, theoretical analysis, computational simulations and experiments at various laser facilities worked together to develop an ICF design that would lead to ignition (net energy gain). Up until 2009, no experimental laser facility in the world was strong enough to create the conditions necessary for an ICF experiment to achieve ignition [44]. When the National Ignition Facility (NIF) opened, the expectation was that within 3 years the first ignition ICF experiments would be carried out [43]. However, nearly 7 years into the experimental campaign at NIF and ignition experiments are still eluding researchers.

The first phase of ignition experiments was under a directive known as the National Ignition Campaign (NIC) [43]. The NIC lasted from 2009 until 2012 and experimental shots were characterized as "low foot". In a low foot shot, the laser power profile is designed to achieve a low adiabat (the ratio of pressure to an approximation of the Fermi degenerate pressure [29]) for the cold shell (≈ 1.65), which allows for better compression of the capsule

at the stagnation phase. Unfortunately, these shots largely underperformed expectations, despite matching specified theoretical design specs and despite pre-shot simulations matching design criteria which suggested the capsules should be able to achieve ignition [43, 13].

Alongside the experimental campaign is a computational campaign aimed at trying to resolve discrepancies between numerical simulations and ICF experiments. A key aspect of this campaign was to match as best as possible the in-shot conditions of each experiment, with the hopes that this would improve the experiment to simulation discrepancies. To accomplish this, these simulations, known as post-shot simulations, utilize a variety of tools. Using a Velocity Interferometer System for an Arbitrary Reflector (VISAR) [5], which is an experimental diagnostic to capture shock timings and velocities during the early phases of the implosion, and a Convergent Ablator (ConA) platform [33], which measures the implosion trajectory and velocities during the later phases of the implosion, the radiation drive used for simulations of the ICF capsule can be tuned to match these in shot characteristics of the implosion [17]. Coupled with the shock timings is an accurate accounting of the surface roughness at the various material interfaces through the use of x-ray imaging and atomic force microscopy of the capsule [17]. A thorough description of the post-shot modeling framework is detailed in Clark et al. and the references therein [18]. For some experiments, such as ICF shot N120321 [8, 17], this framework, coupled with high resolution 3D simulations, improves the discrepancy in the neutron yield (a key observable in the experiments) to around 50% [18], down from 1000% or higher in prior 1D and 2D simulations [28].

While this achievement is without question a success, some additional questions still remain. These simulations are all run in the LLNL code HYDRA [48], which is at its heart a Lagrangian code (i.e., the mesh deforms and moves based on the velocity field). Coupled with the fact that simulations are run without a model to represent diffusion of materials, there is no mechanism by which the outer shell material can be mixed into the fuel during the implosion process except through the growth of perturbations at the DT-shell interface, which simulations suggest do not produce enough mix to explain the observed quantities

in the experiments. Since one of the major causes of the degradation of the experiments is due to the mixing of this material into the central core of the implosion, additional mix is needed in simulations to allow them to match experimental observations. To remedy this, simulations in HYDRA are typically initialized in a pre-mix fashion, where shell material is seeded in the inner regions of the capsule [17].

This dissertation will investigate ICF simulations which couple in a front tracking model [26] to an underlying Eulerian simulation framework (where the grid stays fixed and the material is advected thorough it). This computational model has had great success in prior work modeling the types of instabilities that generate the perturbation growth observed in ICF simulations [27, 41]. Through 2D simulations in a spherical geometry, we will explore how the growth of these perturbations which generate mixing are altered under the use of a front tracking model and what ramifications that may have for the current state of ICF simulations.

We find that the main advantage of adding front tracking is in the numerics relative to Eulerian simulations, where front tracking eliminates numerical diffusion of materials at interfaces. In order to achieve this through simulations that do not include front tracking, high levels of mesh refinement are needed that quickly become unfeasible for full 3D simulations. Compounding this error for ICF are the instabilities in the capsule which can amplify the length scales associated with this unphysical process, producing qualitatively different solutions.

We also detail the stabilization of instabilities during the Richtmyer-Meshkov (RM) stages of the implosion (details in Chap. 6 and 2.2) and discuss the mechanisms driving this phenomenon. We also show a strong coupling effect between the size of the innermost perturbation and the late time symmetry of the capsule, leading to smaller regions of hot fuel in the core of the compression. The main observation from this analysis is that the NIC capsules discussed here sit near a performance cliff in their design specifications. Thus, while currently stable to individual drivers of instabilities, the coupling between these drivers

and additional unmodeled effects can cause perturbations to the design which allow ablator material to reach the edge of the stable regime and mix into the hotspot.

1.1 ICF Capsule Details

The simulations carried out in this dissertation are simulations of the inner part of an ICF capsule. An ICF capsule is multi-layered with an inner region of DT gas, surrounded by a cryogenically frozen region of DT ice. These DT regions consist of the fuel where the initial fusion reactions are designed to take place. Surrounding the DT ice, is a thin shell, typically made of plastic (CH) and referred to as the ablator. This shell usually is multi-layered itself with each layer containing a different percentage (ranging from around 0-4%) of a heavy metal material which is designed to improve the performance of the capsules [43]. A schematic of an ICF capsule is provided in Fig. 1.1 top, showing the different regions. The capsule is around 1 mm in radius and sits inside of a cylindrical chamber (see Fig. 1.1 bottom) called a hohlrahm [43]. Lasers are shot into the hohlrahm to generate an x-ray field, which ablates away the majority of the outer plastic layer and produces a strong compression of the capsule. This approach is known as indirect drive and is the primary experimental configuration carried out at NIF.

Our simulations use a post-shot framework, briefly described in the prior section and detailed in Clark et al. [17]. We use experimental shot N120321 for our study and conduct 1D simulations in both HYDRA and the University of Chicago code FLASH [23] as well as 2D simulations in FLASH. Our capsule models are initialized to match as best as possible the detailed description of shot N120321 provided in Table 1.1.

The entire ICF experiment lasts approximately 22-23ns and the capsule is driven to achieve temperatures exceeding 4-5 keV, densities of nearly 1000 g/cc and pressures exceeding 200 Gbar in the hotspot (inner core region of the compressed capsule). As our simulations are of the capsule only, we use an external radiation source to represent the x-ray field generated by the laser-hohlrahm interaction. This allows us to achieve higher resolutions

Table 1.1: Experimental capsule configuration for NIF experimental shot N120321. Length scales of the individual layers and the material percentages are provided.

Region	Radius	Density	D %	T %	H %	C %	O %	Si %
DT gas	875.84μm	0.0003425 g/cc	60.91%	28.38%	2.33%			
DT ice	945.64μm	0.2445013 g/cc	50.35%	49.35%	0.30%			
Ablator 1	951.56μm	1.0465000 g/cc			57.20%	42.30%	0.50%	
Ablator 2	958.48μm	1.0872090 g/cc			55.90%	41.34%	0.49%	2.28%
Ablator 3	992.35μm	1.1145280 g/cc			55.02%	40.69%	0.48%	3.81%
Ablator 4	1002.62μm	1.0797100 g/cc			56.14%	41.51%	0.49%	1.86%
Ablator 5	1140.56μm	1.0465000 g/cc			57.20%	42.30%	0.50%	

inside the capsule as opposed to simulations which model the entire hohlrahm as well.

1.2 Outline of Dissertation

In Chap. 2 we provide the reader with some background on the key instabilities which drive the growth of the perturbations and lead to mixing of ablator material into the hotspot. We also introduce the front tracking method and detail the successful history of front tracking when it comes to modeling these instabilities.

In Chap. 3 we detail the numerical model used for our simulations and provide details on both HYDRA and FLASH. In order to couple a front tracking model into our 2D simulations in FLASH, we adapted a previously developed Application Programming Interface (API) for our existing front tracking library [38] and implemented the client side functionality. The steps necessary to complete this installation process and the details of the implementation are also provided in this chapter.

In Chap. 4 we use HYDRA to run 1D simulations of N120321 while adding an energy

source to the DT ice region just prior to shock passage. This is designed to capture the impact preheating of this region can have on the adiabat of the DT ice region as the capsule is compressing. We also conduct 1D simulations in FLASH of this same phenomenon to establish a baseline error for FLASH's reduced physical model relative to HYDRA and verify that FLASH is able to still observe meaningful simulation trends in this reduced capacity.

In Chap. 5 we conduct 1D simulations in FLASH with and without the use of front tracking. We carry out a convergence study in 1D and discuss the impact numerical concentration diffusion has on ICF simulations in an Eulerian framework. Since front tracking also prevents numerical diffusion across an interface that is tracked, we add a physical mass diffusion model to investigate the difference between physical mass diffusion and numerical mass diffusion at various grid levels. We also establish a baseline for our 2D simulations.

In Chap. 6 we carry out 2D simulations in FLASH with and without front tracking and mass diffusion models and quantify the impact these computational models have on the simulations. We focus on the various stages of the simulation, where different instabilities drive the dynamics and discuss the overall implications these models have on each stage. Using a buoyancy-drag 3D mix model, coupled into 1D simulations, to predict instability growth, we compare the model to the 2D simulations and examine the performance cliff for mix of ablator material into the hot spot.

Finally, in Chap. 7 we summarize the results we found and discuss possible areas where the work could be extended. We also discuss the impact front tracking and mass diffusion models may have on ICF simulations and other numerical simulations conducted in the high energy density physics regimes.

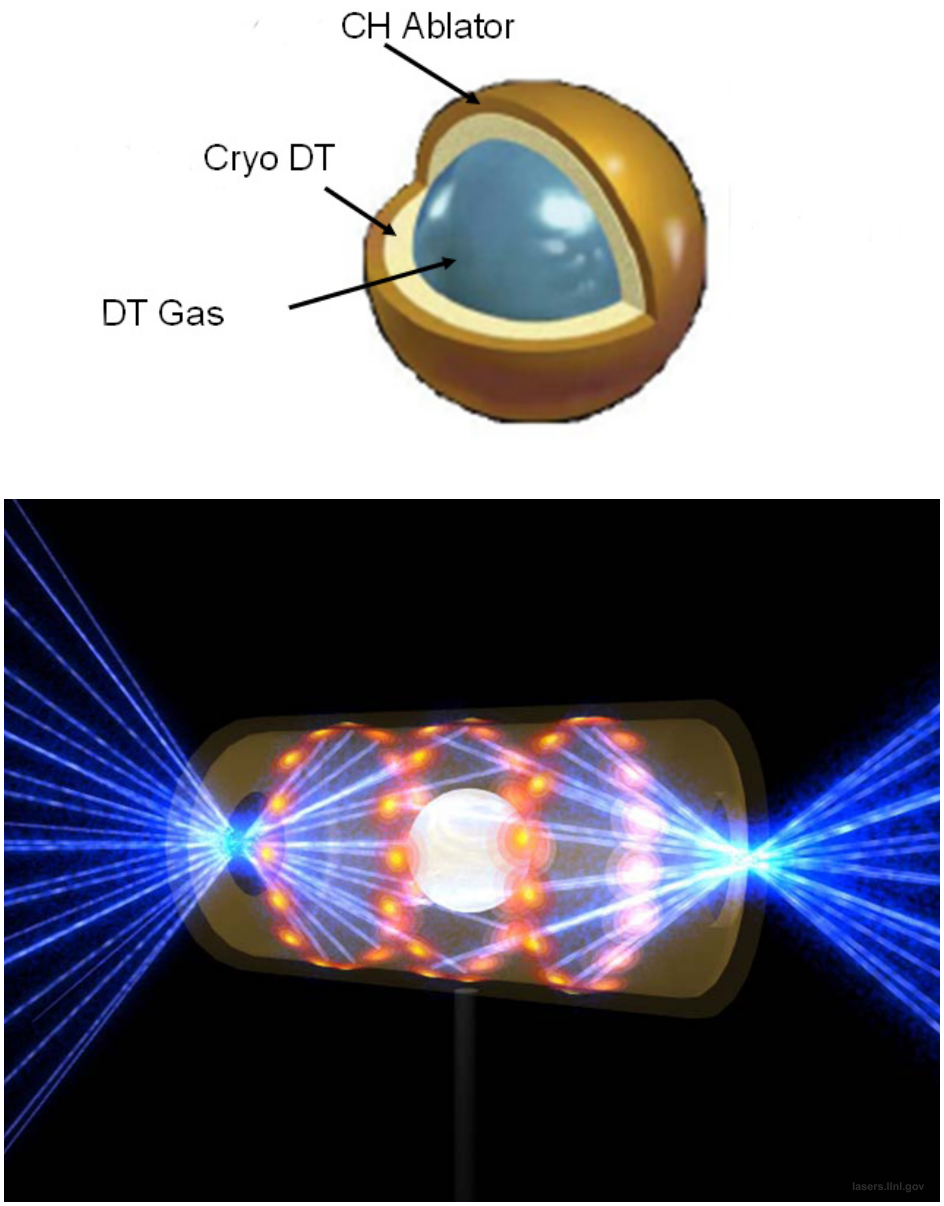

Figure 1.1: Top: A schematic of a typical ICF capsule used in indirect drive experiments. Multiple layers of DT are contained within a plastic shell, which also consists of multiple dopant layers. Image Credit: James Hager [30] Bottom: A capsule contained within a hohlrahm, a cylindrical container which supports the capsule and is used by lasers to generate an x-ray field to drive the implosion. Image Credit: lasers.llnl.gov

Chapter 2

Numerical Modeling of Hydrodynamic Instabilities

As described in Sec. 1.1, an ICF capsule consists of layers of different phases and fluids. At each boundary between layers lies a material interface where instabilities can present themselves when the interface is accelerated. The two classical interfacial instabilities that are of main interest to ICF are the Rayleigh-Taylor (RT) instability and Richtmyer-Meshkov (RM) instability. In this chapter we provide the reader with some background on the RM and RT instabilities and their relevance to ICF capsules. In addition, we discuss efforts to numerically simulate the growth of these instabilities and the benefit front tracking has for these simulations.

2.1 Rayleigh-Taylor Instability

At the boundary between two fluids of different densities lies a material interface. If the light fluid accelerates into the heavy fluid, any small perturbations that were present at that interface will begin to grow. This configuration is known as the Rayleigh-Taylor (RT) instability [65]. The classical form of the RT instability is one in which the acceleration is induced by gravity. When the material on top has a higher density than the one below it, localized perturbations in the interface will cause the light fluid to accelerate into the heavy, as it has more pressure than the hydrostatic equilibrium requires [65]. The RT instability was first studied by Lord Rayleigh in the late 19th century [45] and by Taylor [70] in the 1950s.

Taylor observed that this setup was equivalent to one in which an artificial acceleration was introduced to accelerate a light fluid into a heavy one. Perturbation analysis was used on the linearized Navier-Stokes equations to study what is known as the linear regime of the RT instability. Fig. 2.1 shows a simulation of a single mode RT instability using Frontier [15]. The instability is in the non-linear regime and one can see the development of secondary instabilities on the spike (heavy fluid (top) flowing into the light fluid region (bottom)) edges.

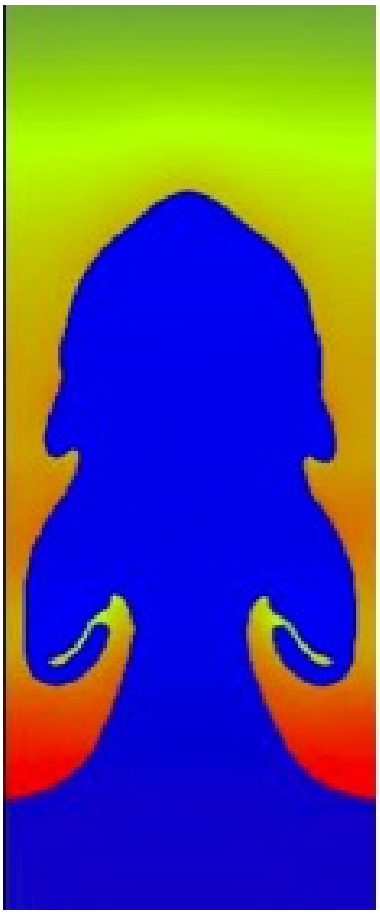

Figure 2.1: A single bubble Rayleigh-Taylor simulation using FronTier. This is well into the non-linear regime. The heavy fluid is on top and the light fluid on bottom. The bubble is still coherent, with secondary instabilities forming on the edges of the spike. This is before full breakup and the turbulent mixing regime.

The RT instability can be observed in naturally occurring phenomenon such as nebulas

and gas clouds in space [68], as well as in atmospheric applications [34]. It also shows up in many engineering applications such as ICF [42] capsules. For ICF, RT instabilities (RTI) occur during two phases of the implosion.

2.1.1 Ablative Rayleigh-Taylor

The first RTI arises at the edge of the capsule, between the heavy remaining ablator material and the lighter ablator material due to it being vaporized. As the acceleration at the edge of the capsule is inward, the configuration is RT unstable. The ablation process itself is a stabilizing mechanism and so the growth of the RTI during this phase differs than that observed in the classical RT instability [69]. The perturbation growth during this phase leads to deviations in the symmetry of the shock waves and carries through to the remaining interfaces and instabilities throughout the rest of the implosion. This RTI growth is studied both numerically [20] and experimentally [7], and the hope is that with tuning of the laser drive and materials, this instability can be largely suppressed in the ICF experiments.

2.1.2 Deceleration Phase Rayleigh-Taylor

The most pronounced mixing during the ICF implosion occurs during the late time deceleration phase. This phase consists of the approximately 500 picoseconds between the point of maximum implosion velocity and bang time. During this phase, the compression of the capsule has built up enough pressure inside the core that the pressure gradient dP now points inward, i.e. the higher pressure region is inside the core and the lower pressure region is outside. This causes a rapid deceleration of the capsule as it approaches stagnation. The stagnation of the capsule converts the kinetic energy into thermal energy, rapidly heating the core and bringing the temperature and density into the regime where the fusion burn begins to occur. The configuration of the capsule during this burn phase is paramount to the successful ignition of the experiment. If the core were perfectly symmetric and pure (consisting of only deuterons and tritons) the conditions necessary for ignition would be

nearly satisfied [18]. However, the deceleration of the capsule, coupled with the density gradient $d\rho$ pointing outward (higher density in the cold shell), makes this phase highly RT unstable and perturbations at the interface begin to grow rapidly. As the RT instability grows, it causes asymmetries in the configuration of the hot core, as well as potentially bringing cold DT and ablator material into the hot spot. These work against the success of the burn and are one of the primary areas of study to explain the under performance of NIC capsules [43].

Since this is the most critical phase of the implosion, understanding the development of the RTI and the mixing it produces is of high importance. In ICF experiments, x-ray radiography is used to determine the final shape of the hotspot at bang time, which identifies low mode asymmetries, which through RTI growth are responsible for distortions in the final shape [62]. To determine the amount of mixing bringing ablator material into the hotspot, x-ray spectroscopy can be used to get a ballpark figure on the mass of ablator material present [60]. This gives an estimate for both simulations and theory to shoot for when trying to model this instability. Theoretical estimates, by design, must use heavily simplified models and have had varying success in matching experimental observations across the board [3]. However, in high resolution, high fidelity 2D and 3D post-shot simulations, a strategy of seeding initial amounts of ablator material, based on experimental observations, into the inner regions of the DT fuel is still required in order to get the desired late time mix [18]. This instability and the ensuing mix will be the focus of the simulations carried out in this dissertation. Through the use of front tracking and a physical mass diffusion model, we will investigate whether improving the accuracy of the numerical models can have an impact on the amount of mix present during simulations of this RTI.

2.2 Richtmyer-Meshkov Instability

The Richtmyer-Meshkov (RM) instability is similar to the RT instability but instead of a continuous acceleration field, the interface is subjected to a single impulsive acceleration.

The impulsive acceleration is typically in the form of a shock wave, which as it interacts with the interface deposits vorticity causing the initial perturbations to grow. The RM instability was first characterized theoretically by Richtmyer [61] and experimentally verified by Meshkov [50]. RM instabilities occur in a wide variety of engineering applications from ICF [42] to hypersonic flight scramjets [75]. They can also be inferred in astrophysical phenomenon such as supernova explosions [37].

The RM instability can occur for any density discontinuity, whether the shock travels from the heavy to the light fluid or the light to the heavy. Under a heavy-to-light configuration, the interface will initially compress and the phase will reverse while from a light to heavy configuration the perturbations will begin to grow directly [6]. In ICF, the primary shocks travel from the heavy to the light fluid, while reflected shocks which may reshock the interfaces may travel from light to heavy. As there are multiple shock waves in ICF and multiple interfaces, the wave structure quickly becomes quite complicated and thus will be best studied using numerical simulations, as we carry out in this dissertation.

2.2.1 Shock Transit Richtmyer-Meshkov Phase

For N120321 and the low foot shots carried out during NIC, the laser drive generates a series of four shocks that propagate through the capsule [29]. These shocks vary in strength, scaling up from weakest to strongest, with the first having a shock speed of $\approx$ 10 km/s and the final having a shock speed upwards of 35 km/s in the plastic ablator. As a result, the subsequent shocks overtake the prior ones at various locations in the capsule. In the simulations carried out here, which are tuned to match N120321, the final 3 shocks coalesce before interacting with the fuel-ablator interface and all four coalesce before interaction with the DT ice-gas interface. As the shocks cross the interfaces they deposit vorticity and provide the mechanisms needed for initial perturbations to begin to grow.

The RM phase of the ICF implosion is where the initial seeds for the more critical deceleration phase RTI takes place. There is a carryover effect from the initial perturbations

generated due to laser inhomogeneities [35], which feed into the perturbations generated during the RM phase and eventually seed the RTI instability at late time. Thus it is important to quantify the growth of these RM instabilities. Our 2D instability simulations start from the point right before the first shock interaction with the fuel-ablator interface and carry through to bang time (time of largest neutron production), to model the entire instability regime. These simulations will be detailed in Chap. 6.

2.3 Numerical Modeling of Interfacial Instabilities

While theoretical models can give quite accurate representations of macro observables such as growth rates during both the linear and non-linear regimes [65, 9], numerical simulations provide detailed data on all aspects of the dynamics driving these instabilities. Even relative to experiments, the researcher is at the mercy of the diagnostic resolution level and availability at the time of the experiment. Thus, it has been a heavy area of research for decades to produce accurate and predictive simulations of both RM and RT instabilities.

2.3.1 Verification and Validation

A key step for any numerical simulation is to verify itself against established theories by comparing their simulation results to theoretical models. In addition, a numerical simulation should be validated via comparison to experimental quantities when setup to model a specific experiment. If a code can pass both verification and validation without the need for extensive parameter tweaking, it is capable of predictive simulations which can greatly reduce the costs associated with engineering and design.

For RM and RT instabilities a long standing debate had been focused on whether there was a universal growth rate α_b for the evolution of bubbles. Experiments had long observed an α_b of $0.05 - 0.07$, while numerical simulations suggested an α_b of $0.02 - 0.03$ [22]. In an extensive code collaboration study, the α-group paper of Dimonte et al. [22] hypothesized

that one of the main reasons numerical simulations were unable to match experiments is due to long wavelength initial perturbations present in the experimental data, but unaccounted for in the numerical simulations. However, this was shown to only be a $5-10\%$ effect for the numerical simulations in question [27, 36]. The main reason put forth by Glimm et al. [27] for the discrepancy between RT growth rates in simulations versus experiments, was the excessive numerical diffusion occurring at material interfaces. With the use of a front tracking algorithm [26], Glimm and his co-authors have a long history of success [27, 41, 24] matching their simulated growth rates with that of experiments. In addition, in Lim et al. [41], they conclude the experiment to experiment variability in α_b is due to differences in physical transport properties, such as molecular viscosity and species diffusion.

In ICF, a similar discrepancy in mixing has been the focus of extensive research and it is believed that simulations may be predicting lower than observed growth of RM and RT instabilities [28]. This lends itself to the focus of this dissertation, which is to determine if front tracking can play a role for the growth of these instabilities in the high energy density physics regime, where a much more complicated interaction of various physical processes takes place.

2.4 Front Tracking

The idea behind front tracking is to couple a lower-dimensional surface, which is dynamically tracked with a standard Eulerian solver. In a typical Eulerian simulation, the mesh stays fixed and the fluid is advected through the domain typically by calculating fluxes at the grid cell boundaries. Since the solution is updated by interactions of a cell with its neighbors, at areas of steep gradients, where the material or phase may change, i.e. at a material interface, there is an unwanted mixing between neighboring cells. Front tracking discretizes and advects a surface representing this material interface which can then be used to adjust solution steps, so that the unwanted mixing between neighboring cells of different materials is prevented.

The front tracking algorithm used in this dissertation has been in development for over 30 years [15], and has been extensively verified and validated in turbulent mixing problems [27]. A high level overview of the front tracking algorithm can be broken down into 3 main steps.

1. The front is propagated in the normal direction by calculating the normal velocity from a 1D Riemann solution. The input to the Riemann solution is taken via an interpolation from the grid cells representing a single material bounding the front. By design, the front represents the interface between two fluids, so this provides two interpolated states which are the input states for the Riemann problem. Using only the normal velocity, a resulting velocity of the contact wave can then be calculated, which is used to advect the front point following Eq. 2.1, where $\mathbf{X}$ represent the position, $\mathbf{V}_n$ the normal velocity and dt, the computational timestep.

$$\mathbf{X}_{new} = \mathbf{X}_{old} + \mathbf{V}_n * dt \tag{2.1}$$

2. After the front has been moved to its new location, any grid cells where the front crossed their center, now have the wrong material for the side of the front they reside on. Thus they are updated through the solution to another Riemann problem.

3. Finally, the interior solver can be applied where any stencil that crosses the front is adjusted to replace the incorrect material state with a ghost cell extrapolated state from the correct material [4].

The immediate benefits of front tracking are two-fold. Firstly, since there is no mixing of materials at a tracked interface, no non-physical diffusion is introduced. Secondly, as the front has a subgrid resolution, i.e. it provides a detail below the actual resolution of the underlying grid, it can perform better at coarser resolutions. In the remainder of this dissertation, we will investigate the impact front tracking has on ICF simulations.

Chapter 3

Simulation Methodology

3.1 Model Equations

The computational model used for the ICF simulations conducted in this dissertation starts with the well known Navier-Stokes equations for fluid flows, with the addition of a species concentration equation for the coupling of the various ion species (See Eq. 3.1). Here, ρ is the density, $\mathbf{u}$ is the velocity vector, E_{tot} the total specific energy, P_{tot} the total pressure and $\boldsymbol{\psi}$ is the species mass concentration vector. κ is the thermal conductivity, D is the mass diffusivity and the viscous stress tensor $\tau = \mu((\nabla\mathbf{u}) + (\nabla\mathbf{u})^T - \frac{2}{3}(\nabla\cdot\mathbf{u})\mathbf{I})$, where μ is the dynamic viscosity.

$$\begin{aligned} \frac{\partial\rho}{\partial t} + \nabla\cdot(\rho\mathbf{u}) &= 0 \\ \frac{\partial\rho\mathbf{u}}{\partial t} + \nabla\cdot(\rho\mathbf{u}\mathbf{u}) + \nabla P_{tot} &= \nabla\cdot\tau \\ \frac{\partial\rho E_{tot}}{\partial t} + \nabla\cdot(\rho E_{tot}\mathbf{u} + P_{tot}\mathbf{u}) &= \nabla\cdot\kappa\nabla T \\ \frac{\partial\rho\boldsymbol{\psi}}{\partial t} + \nabla\cdot(\rho\boldsymbol{\psi}\mathbf{u}) &= \nabla\cdot D\nabla\boldsymbol{\psi} \end{aligned} \tag{3.1}$$

For all the simulations carried out here, we set the dynamic viscosity coefficient μ to 0. It has long been believed that viscosity plays a minor role in the ICF process and it is typically left out of simulation models [72]. Recent work by Weber et al. [74, 73] investigated the importance of viscosity models in ICF simulations and found that in 3D

they helped to damp out turbulent structures in the hot spot, however had no major impact on the thermodynamics of the hot spot and thus the performance of the capsule. In 2D, the turbulent structures are not present and viscosity was found to have little to no impact on simulations conducted in HYDRA by Clark et al. [18], thus reinforcing the assumption that viscosity does not play an important role in ICF simulation models.

For our radiation-hydro simulations the total internal energy is broken into three components to allow for separate modeling of the ion, electron and radiation energy fields, $e_{tot} = e_{ion} + e_{ele} + e_{rad}$. Additional equations are then needed to extend the Navier-Stokes to a $3T$ framework to allow the ion, electron and radiation temperatures to vary individually. These additional equations are detailed in Eq. 3.2 where e is specific internal energy, P is pressure, T is temperature, c_v is the specific heat and τ_{ei} is the electron-ion equilibration time. The subscripts $_{ele}$, $_{ion}$ and $_{rad}$ are used to denote that variable for a specific component.

$$\begin{aligned}
\frac{\partial \rho e_{ion}}{\partial t} + \nabla \cdot (\rho e_{ion} \mathbf{u}) + P_{ion} \nabla \cdot \mathbf{u} &= \rho \frac{c_{v,ele}}{\tau_{ei}} (T_{ele} - T_{ion}) \ , \\
\frac{\partial \rho e_{ele}}{\partial t} + \nabla \cdot (\rho e_{ele} \mathbf{u}) + P_{ele} \nabla \cdot \mathbf{u} &= \rho \frac{c_{v,ele}}{\tau_{ei}} (T_{ion} - T_{ele}) \ , \\
\frac{\partial \rho e_{rad}}{\partial t} + \nabla \cdot (\rho e_{rad} \mathbf{u}) + P_{rad} \nabla \cdot \mathbf{u} &= 0
\end{aligned} \tag{3.2}$$

To model the radiation energy and its evolution, we use a flux-limited multigroup radiation diffusion (MGD) approach. In MGD, the radiation energy is broken into multiple energy groups and each energy group is evolved separately. The radiation energy is coupled into the matter through absorption and emission processes, which modify the electron energy. For further details on MGD and its implementation we refer the reader to the standard textbook by Mihalias and Mihalias [51] and the documentation for the FLASH [23] code.

3.2 FLASH Configuration

FLASH is a modular radiation hydrodynamics code designed for the simulation of a variety of astrophysical and HEDP applications. For our ICF simulations, we use the split

PPM hydrodynamics solver, coupled with multigroup radiation using 60 energy groups. The energy groups are logarithmically spaced in three bands, i) 25 groups from 30 eV to 1 keV, ii) 25 groups from 1 keV to 5 keV and iii) 10 groups from 5 keV to 100 keV.

Thermal conduction is also included in the FLASH distribution and was used for both ions and electrons. As the Lee-More model [40] is an electron thermal conduction model, it is not compatible with the ion transport module. Therefore, we use the FLASH Spitzer model for both ion and electron conduction. To show the impact of the thermal conduction, in Fig 3.1 we plot the same FLASH simulation midway through the deceleration phase as a wave is reflecting off of the origin. Three curves are shown, representing the Lee-More thermal conduction model with electron transport only (red dashed line), the Spitzer thermal conduction model for electron transport only (blue dotted line) and the Spitzer thermal conduction model for electron and ion transport (black solid line). The Lee-More and Spitzer models without ion conduction both show an unphysically high spike in the temperature as the wave reflects off the boundary. These elevated temperatures then remain throughout the remainder of the deceleration phase until just before bangtime (time of maximum neutron production rate) when the heat exchange unit nearly equilibrates the ion and electron temperatures. While the Lee-More model does a slightly better job for peak temperature, the effect of including ion conduction completely eliminates the unphysical spike. Thus the choice to use both ion and electron transport with the Spitzer model is clear.

The EOS used in our simulations is an ideal gas with a temperature dependent gamma for the ions, set to achieve a $\gamma(T) = 5/3$ in the hot spot and $\gamma(T) = 7/4$ in the cold shell, with a smooth transition between them. The value of 7/4 for the cold shell was chosen from calibration to the Sesame EOS [32, 63, 64]. The exact value for $\gamma(T)$ is calculated via Eq. 3.3, with T in keV. A and B set the range of $\gamma(T)$ values, while C controls the speed of the transition of $\gamma(T)$ and D sets the midpoint of the transition. The values of C and D are tunable and were chosen to maintain a γ of approximately 5/3 in any region where the

temperature is larger than 1 keV.

This simple ideal gas EOS is one of the areas where the FLASH has reduced physics and is thus a candidate for improvement in future work. It is the opinion of the authors that for the simulations carried out in this work, this reduced model is sufficient for the desired analysis. Thus, an implementation of a more advanced widely available EOS such as SESAME [46] was not undertaken.

$$\begin{aligned} \gamma(T) &= A - B * \mathrm{erf}[C * (T - D)] \\ A &= \frac{7/4 + 5/3}{2} \approx 1.7083 \\ B &= \frac{7/4 - 5/3}{2} \approx 0.0417 \\ C &= 15 \qquad D = 0.5 \end{aligned} \tag{3.3}$$

The FLASH simulations use 6 species (Deuterium, Tritium, Hydrogen, Carbon, Oxygen and Silicon). For each of these species, a separate tabulated opacity table is maintained. The opacities are generated from the Los Alamos TOPS Opacity database [47] using all temperatures contained in the database and 74 densities logarithmically spaced from .001 g/cc to 10000 g/cc.

3.2.1 Initialization and Boundaries

At early times, the physics of the ICF capsule is dominated by radiation transport and ablation. To take advantage of the more sophisticated models present in the HYDRA code, we run a 1D HYDRA simulation until approximately 14.5 ns, about 500 picoseconds before the first shock interacts with the DT-ablator interface. At this time, the state variables, radiation group energies and materials are dumped from the HYDRA simulation and used to initialize our FLASH simulation. While using FLASH to simulate the key RM and RT phases of the implosion, we are able to take advantage of the additional front tracking and mass diffusion models that we have added to the FLASH software during the key phases

of the ICF capsule where transport and mix occurs. As the underlying HYDRA data is 1D, perturbations are seeded at the DT ice-gas interface and DT-ablator interface using randomly assigned amplitudes and phases for spherical harmonics. Since ablation physics dominate the edge of the capsule and FLASH does not have an ablation package, we set the edge of our FLASH simulation to represent a Lagrangian point inside the first layer of doped ablator material, which does not ablate in the HYDRA calculation. The 1D HYDRA data is then tabulated for the remainder of the simulation at that specified Lagrangian cell and the Lagrangian position along with its states and radiation group energies are then used as a time and space dependent boundary condition in FLASH.

Since the HYDRA simulation uses a more complicated EOS model, QEOS [53], which is not available in FLASH, it is over-specified for the currently employed FLASH EOS which uses the simple ideal gas approximation discussed in Sec. 3.2. Thus, a choice between matching either pressure or temperature must be made. Since the pressure is used to drive the hydrodynamics, it is more important to match the pressures than the temperature profile, so only the pressures and densities in the initialization and boundary conditions are matched and the temperatures are set using a call to the FLASH EOS. In addition, this allows us to capture the remaining shock waves as they come across our imposed boundary location and achieve a similar shot trajectory as to the HYDRA simulation and the experimental shot, N120321, that the HYDRA simulation is tuned to match.

3.2.2 2D Spherical Implicit Diffusion Solver

In its current release, FLASH does not have a working implementation for the solution of an implicit diffusion equation in 2D spherical geometry. As our simulations require this capability, we modified the FLASH source code files associated with the setup of the matrix used for the 2D diffusion equation to contain the geometric terms that were currently missing from the 2D Cartesian setup. The derivation of these terms is carried out below.

We begin with the general form of the implicit solver solved by FLASH, where f is the

variable being diffused, A, B, C and D are coefficients and ∇_{sp} is the spherical del operator.

$$A\frac{\partial f}{\partial t} + Cf = \nabla_{sp} \cdot B\nabla_{sp} f + D \tag{3.4}$$

As we are using a finite volume approach, the entire equation is integrated over the computational cell volume V_i.

$$\int_{V_i} A_i \frac{\partial f}{\partial t} dV_i + \int_{V_i} C_i f dV_i = \int_{V_i} \nabla_{sp} \cdot B_i \nabla_{sp} f dV_i + \int_{V_i} D_i dV_i \tag{3.5}$$

In a finite volume approach, the state variables and coefficients are represented by volume average values over the cell volume, allowing us to integrate the majority of the terms.

$$A_i \frac{\partial f}{\partial t} V_i + C_i f V_i = \int_{V_i} \nabla_{sp} \cdot B_i \nabla_{sp} f dV_i + D_i V_i \tag{3.6}$$

Applying Gauss' theorem to the remaining volume integral turns it into a surface integral, where S_i represents the surface and $\mathbf{dS}_i = \mathbf{n}dS$.

$$A_i \frac{\partial f}{\partial t} V_i + C_i f V_i = B_i \int_{S_i} \nabla_{sp} f \cdot \mathbf{dS}_i + D_i V_i \tag{3.7}$$

The remaining integral amounts to the calculation of $B_i \nabla_{sp} f$ on each face of the computational cell. Since the del operator has a $1/r$ term in front of all θ derivatives, this was the only necessary change in the FLASH source code to enable the implicit diffusion solver to work in 2D spherical coordinates.

3.2.3 Physical Mass Diffusion

FLASH does not have a built in physical mass diffusion unit, so a diffusion unit was added using the HEDP diffusion model developed by Daligault [21]. Daligault's diffusion model is an interpolation fit to molecular dynamics simulations covering a large range of inverse screening lengths and plasma coupling parameters. The model consists of two regimes,

one model fit for small values of the coupling parameter and one model fit for large values of the coupling parameter (Γ). We choose a switching criteria of $\Gamma = 3$ based on analysis of the plots provided in Daligault's paper [21].

The work to implement this model in FLASH was largely undertaken by my colleague Verinder Rana and thus a further analysis of this model as well as a full discussion of the implementation will be contained in his dissertation. For additional reference, we refer the reader to Rana et al. [59], which contains additional details on this diffusion model and other physical transport models applicable to the ICF regime.

3.3 Front Tracking API

The importance of front tracking for hydrodynamic instability simulations was discussed in Sec. 2.4 and detailed in work led by Glimm and his students [27, 41, 24]. As our goal in this work is to study the development and modeling of these instabilities during an ICF implosion, it is important to consider their growth with and without the use of a front tracking algorithm in order to quantify the potential impact this may have on key experimental observables.

In order to allow us to couple the front tracking algorithm into our ICF Rad-Hydro simulations in FLASH we build on the work done by Kaufman et al. [38, 39] to develop a front tracking library which can be linked into any hydro code. In its current form this library (Application Programming Interface (API)) requires the user to develop a set of client functions to pass information back and forth to the front to determine the velocities of the front points and to receive information about where the front crosses the interior cells.

As this is the first time the front tracking API (FTAPI) has been coupled into a physics code, in this chapter we start by detailing the required client functions and their implementations in FLASH. A website where source code and other information on the API is available can be found at `http://fti.ams.stonybrook.edu/FTAPI.html`.

3.3.1 Client Functions (FrontTracking Module)

All functions listed in this section are part of the Front Tracking module, designed for the FLASH source tree. They are all named FrontTracking_* where * is replaced with the function name below. This follows the FLASH naming convention for module functions.

3.3.1.1 init

Summary: A simple interfacing function for the Front Tracking initialization routine. The initialization step consists of passing the required Grid information to the Front Tracking library so that it can properly initialize the front. A call to the propagate routine with a dt of 0.0 is needed to allow the front to simplify the surface that may have been created during an initialization. In addition, a call to initialize the component array is invoked.

Inputs: None

Outputs: None

Library Functions Called:

- FTAPI_init

3.3.1.2 updateComp

Summary: For efficiency, we maintain a data structure to store the components (material IDs) at each cell center in the domain. Thus the **updateComp** function is needed to update the components in each cell (if necessary) after the front is propagated.

When a cell center is passed by a moving front, the component changes in the process. Since the physical state stored at that cell center is supposed to be representative of the component of the cell, the state needs to be updated to reflect its new component. To

update the state in a physically consistent way, we solve a 1D Riemann problem in the direction of the front normal across the cell center. The direction of the front normal is found via interpolation from normals on the front, using front points nearby to the cell. The left and right input states for the Riemann problem are taken as the old state of the cell, prior to front movement and the component change, and the cell's ghost state, as defined in the **fillGhostStates** function, for the material it is becoming.

The contact wave solution p^* and u^* (converted back to grid velocities using the interpolated normal vector and tangential velocity of the ghost front state) are the new state pressure and velocity. The density for the new state is determined in a thermodynamically consistent way, using a wave curve expansion based on the difference in pressure between p^* and the ghost front state pressure.

Inputs:

- Ghost State Array calculated in **fillGhostStates**

Outputs:

- Component Array

Library Function Called:

- FTAPI_getComponent (material ID at a coordinate point)
- FTAPI_gridNormal (front normal vector interpolated to a grid point)

3.3.1.3 propagate

Summary: A simple interfacing function for the Front Tracking propagation routine. The propagation step consists of four main parts:

1. FillGhostStates,

2. UpdateGuardCells,

3. Propagate and

4. UpdateComp

. Updating guard cells is needed to allow for the ghost states set in the first step to be applied to any buffer cells, using the appropriate boundary conditions. The Propagate step, calls the API library function that invokes the propagation routine.

Included in the propagate routine is a subcycling loop, which can be needed if the front dt restriction is more severe than that calculated by FLASH. This is a rare occurrence, but can happen if the velocity at the front point is determined to be larger than those on the grid. An alternate option would be to build in an interface to allow the front dt and FLASH's dt to both be taken into account when the step dt is calculated, however that has not been implemented in this version. Instead, the front will propagate however many times are necessary to allow it to reach the same elapsed physical time as that of the underlying FLASH physics step. As long as the components and ghost states are updated in tandem with each propagation, this will be physically consistent during the subcycling steps.

Inputs:

- *dt* of the current timestep

Outputs: None

Library Functions Called:

- FTAPI_propagate

3.3.1.4 getVel

Summary: The **getVel** function is designed to fulfill a request by the front for the velocity of a front point (i.e. a location in the domain) so that it can be propagated. The front represents the Lagrangian propagation of an initial isoconcentration surface between two fluids. To be physically consistent in the Lagrangian propagation a Riemann problem is solved between a representative state for the materials which we refer to as a left state and right state. To determine the left and right states at the front point, we use a procedure adapted from Bo et. al [4], which reconstructs front states on the fly from an interpolation of a bounding box of cells relative to the front point. On the side of the interface where these are physical (real) states, the real state is taken and on sides where the other material is present, a ghost fluid state, obtained following the procedure outlined in the **fillGhostStates** function is used.

The velocities for the left and right front states are then decomposed into a velocity normal to the front and tangential to the front, by dotting with a normal vector for the front point of interest. This produces a 1-dimensional input state along the normal direction of the front, using the normal velocity.

The resulting 1-dimensional Riemann problem is solved, here using the built-in Riemann solver in FLASH (using the method of Collela and Glaz [19]) and the Riemann solution contact wave velocity, u^* is the desired front point's velocity. Note that since the front is only propagated in the normal direction [4, 15], this is the velocity to be returned back through the API to allow the Front Tracking library to move the points.

Inputs:

- Coordinates of the front point
- Left side component (material ID) at the front point
- Right side component (material ID) at the front point

- Ghost State Array calculated in **fillGhostStates**

Outputs:

- Velocity of the front point

Library Functions Called:

- FTAPI_normal (normal vector at a front point)

3.3.1.5 fillGhostStates

Summary: This function is a helper function in that it is not required to implement the front tracking API, but helps organize and simplify the implementation. In the **getVel** function, the velocity of a front point is obtained from the solution of a Riemann problem. The inputs to this Riemann problem are a representative state for each component. To obtain the representative state for component i, we interpolate from the nearby cells which match that component ID. The bounding box of cells centers for the front point will almost certainly not be all of the same component, as the interface surface must be between the cells. Thus, instead of trying to handle interpolation of each case accordingly, a two-step interpolation procedure is employed.

In the first step, which is carried out here in the **fillGhostStates** function, all cells nearby to the front calculate a double-valued state function, one for each component ID. For the component ID that matches the component of the cell being acted on, the physical state is copied into the ghost state. For the other component ID, the one that does not match the physical component in the cell, an average state is obtained from its neighbors with a physical component matching it. For example, for a cell which has physical component 2, GhostState2 would be set equal to the state in the current cell and GhostState1 would be set to be an average of the neighbors to the current cell which have physical component 1.

The definition of a neighbor is somewhat arbitrary and depends on the underlying structure of the mesh. For our implementation in FLASH, which uses a structured mesh,

we define the average state from the closest bounding box of cells which contains a cell with the desired physical component.

With the double-valued state function at every cell near the front, the second stage of the interpolation, carried out as part of the **getVel** function can be carried out using a standard bi-linear interpolation from a set of like component ghost states. The name fillGhostStates may be somewhat of a misnomer, in that they don't represent the ghost state as defined in Bo et. al [4], but rather an average state, used to aid in the process of calculating the front states.

The ghost states defined here are also used in the **updateComp** function, as the input to the Riemann problem used to determine the correct state for a cell which has had its component changed due to front propagation.

Inputs: None

Outputs:

- Ghost State Array

Library Functions Called: None

3.3.1.6 output

Summary: A simple interfacing function for the Front Tracking output routine. The output step consists of passing a request to the front to dump either a checkpoint file or a plot file.

Inputs:

- Flag for checkpoint or plotFile

Outputs: None

Library Functions Called:

- FTAPI_output
- FTAPI_writeRestart

3.3.2 Modified FLASH functions

In addition to developing a set of client functions to allow FLASH to interface with the FTAPI, modifications to existing FLASH files were needed to fully implement the front tracking algorithm. Front propagation and consistency of the front surface is all handled on the FTAPI side, but the other half of front tracking, which is the modification of stencils during the interior update, needs to be directly applied to the interior solvers implemented in the client code. The functions that were modified and a description of those changes are listed here.

3.3.2.1 hy_ppm_block

In the current version of the FLASH FTAPI, the full active front tracking algorithm is only implemented for the split PPM hydro solver. In an actively tracked algorithm, interior stencils which contain states from both components are modified so that when solving a cell for a particular component ID, only states which match that component ID are used in the stencil. Since those states are not always physical, i.e. when the stencil takes you across the front, they are replaced with a ghost cell state, determined from a Riemann solution between the physical left and right states at the front. This Riemann solution provides the pressure and velocity, the density is determined using a wave curve expansion for the particular component. The reader is referred to the seminal front tracking paper [15] for a full discussion of this algorithm.

In **hy_ppm_block** the stencils are set up for the interior solve, so this is the natural place to make adjustments to the stencil. Once the stencil has been corrected, the PPM algorithm can proceed as designed. To correct the stencil, the sweep is carried out from left to right only up to the point that the component changes. Once a component change is encountered (i.e. a front point has been crossed), a Riemann solution between the two distinct component cells bounding the front point is solved. This Riemann solution and its corresponding midstate density for the component being solved is then used to populate the rest of the stencil. This corrects the stencil and the PPM algorithm is allowed to proceed from there. After a call to **hydro_1d**, fluxes for each cell face are stored for use in the **hy_ppm_updateSoln** function. As these fluxes are only valid for the cells which had the primary component ID, those fluxes are stored and the rest are discarded. The sweep then continues starting from where it left off and working on this new component until a front point is encountered. Again, a Riemann solve is used to populate the remaining stencil on both the left and right sides and fluxes for only the valid component cells are stored. This procedure continues until the entire sweep has finished.

At cell faces where the two neighboring cells have different components, two fluxes, one for each component is calculated. A second array is created to flag the faces where the flux function is dual-valued and store the alternate flux for use during the update to the state variables carried out in the **hy_ppm_updateSoln** function. Having a double-valued flux function at these faces creates a small error in conservation, which is the focus of ongoing work [39, 66], and has been a known minor drawback of the current front tracking algorithm. However, a long and extensive track record of verification and validation [27, 41, 24] suggests that this should not have a meaningful impact on the current results.

3.3.2.2 hy_ppm_updateSoln

As detailed in the above section, the flux function is dual valued at cell faces which border two cells with different components. Only a small modification is carried out here

identifying when we have a face with a dual valued flux function and to choose the correct one. This is done by consistently making the flux for the cell which borders to the left the one that is stored in the alternate flux array.

3.3.2.3 rieman

The Riemann solver in FLASH uses the method of Collela and Glaz [19] and is configured to run directly with the hydro unit over a specified 1-dimensional region in the domain, taking a vector of inputs and producing a vector of outputs. For our added uses of the Riemann solver for front tracking we only have a single Riemann solution that is needed. A duplicate of this function was created and configured to take a single left and right state input vector and produce a single output solution without the use of additional step through functions to produce left and right extrapolated states.

In addition, instead of returning an average density, the function returns two densities, one for the left side contact and one for the right side contact from the Riemann wave expansion. To determine the correct densities for the left and right solutions, the input pressures are compared to the Riemann solution pressure, p^*. If $p_I > p^*$ the wave is a shock and if $p_I < p^*$ the wave is a rarefaction, where p_I is the respective input pressure for that side. Once the wave type is determined, a wave curve expansion can be calculated to determine the thermodynamically consistent density for each side of the contact wave.

3.3.2.4 Additional functions

Additional minor changes are made in **hy_ppm_interface** and **hy_ppm_sweep** to allow for the additional flux array structure. Since the major changes to the FLASH code impact only the sweep algorithm, only minor changes, mainly for the purposes of invoking the Front Tracking module functions described in Sec. 3.3.1, were also needed. A change was made to **Driver_evolveFlash** to add calls to **FrontTracking_propagate** at the beginning of each physics sequence. In addition, **Driver_initFlash** and **IO_output** were modified to add

Table 3.1: Initial conditions for the Sod shock tube problem.

	Right	Left
Density	1	0.125
Pressure	1	0.1
Velocity	0	0

a call to the FrontTracking module's **FrontTracking_init** and **FrontTracking_output**, respectively.

3.3.3 API Testing and Proof of Concept

Since the API consists of a major implementation upgrade to FLASH, a few tests were carried out to verify that the code was correctly solving the fluid equations and that there were no bugs present in the implementation. Since both FLASH and FronTier have been heavily verified and validated, simple A/B comparisons between FLASH with and without the front tracking algorithm turned on can provide a solid testing suite as well as allow for a proof of concept for the advantage of front tracking. We detail a few of the tests conducted here and discuss the advantages of the use of front tracking.

3.3.3.1 Sod Shock Tube

One of the first tests that any fluid code should be subjected to is the shock tube problem described by Gary Sod [67]. This is a basic test of a fluid solver modeled after a shock tube, where a density and pressure discontinuity is initialized in the center of the domain producing a shock wave, contact wave and rarefaction wave which propagate through the domain as time evolves. The shock tube problem has the benefit of an analytic solution to compare to [67]. The initial conditions for our problem follow those laid out in the FLASH manual and detailed in Table 3.1 where the domain is setup from $x = 0$ to 1.

The simulations are all run in 2D with a single symmetric interface at $x = 0.5$. This simplifies to a 1D physics computational model. In Fig. 3.2 we plot both the FLASH base simulation (blue, dotted) and the FLASH simulation with front tracking coupled in (red, dot-dash), along with the exact solution (black, solid). The resolution for the FLASH runs presented here is 250 grid cells. The exact solution is calculated at 1000 evenly spaced grid points, using the exact Riemann code found at `http://cococubed.asu.edu/code_pages/exact_Riemann.shtml`. In the left frame, we plot the full domain. Some differences, as expected between the exact solution and the FLASH solutions are evident at the shock and contact discontinuities. The shock, which is not tracked by FT, shows almost no differences between the two FLASH simulations, while the contact shows a much sharper interface captured by the FT version of FLASH relative to the base case. To emphasize these differences, the contact discontinuity is blown up in the right frame. The FLASH version with FT does a much better job of capturing the sharpness of the contact relative to the base simulation, even at this resolution of 250 cells.

For a quantitative analysis, we conduct a convergence study for both simulations ranging over resolutions between 50 cells and 1600 cells. In Table 3.2 we plot the average relative pointwise error in density for each simulation relative to the exact solution. The average relative L1 error is calculated in a pointwise fashion, comparing each grid cell value in the simulation to the exact solution at that point (see Eq. 3.8).

$$\overline{\text{Error}_{\text{L1}}} = \frac{1}{N} \sum_{i \in grid}^{N} \frac{|\text{sim}_{\text{i}} - \text{exact}_{\text{i}}|}{\text{exact}_{\text{i}}} \tag{3.8}$$

Table 3.2 shows that at the coarsest resolution, front tracking has about a 15% improvement over the base FLASH simulation and that as the resolution increases, the improvement decreases but for the most part is still maintained. As this comparison is taken over the whole domain and front tracking only has a major impact on the small region around the contact, we conduct the same analysis, calculating the relative L1 error only over the region in space between $x = 0.65$ and $x = 0.72$, which brackets the contact discontinuity which

occurs at 0.685 in the exact solution. A drastic improvement in the average L1 error is observed in the contact region where front tracking has the main effect. The FT simulation improves the average error by approximately 5 times throughout all resolution levels tested here. We also calculate the convergence orders in both Tables 3.2 and 3.3. The convergence order $p = log_2(E_c/E_f)$, where E_c and E_f represent the errors on consecutive grid levels with c the coarser grid and f the finer grid. The log_2 in the convergence order calculation is valid for resolution increases of a factor of 2. Over the full domain (Table 3.2), with the exception of the first comparison, the convergence order is roughly the same between the two simulations with some variability between them. For just the region near the contact discontinuity (Table 3.2), the FT simulation shows an improvement of nearly a 1st order convergence across all domain level, again with the exception of the 50 to 100 comparison. This is an improvement over the base FLASH simulation which has a dropping convergence order over the majority of the comparisons and is shy of 1 on all grids except for the first two. A convergence order of 1, despite using a PPM method in FLASH which is formally accurate to 2nd order for hydrodynamics, is to be expected for the shock tube problem as the presence of shocks and discontinuities tend to prevent the observance of higher than 1st order convergence.

3.3.3.2 Rayleigh-Taylor Single Mode

We conduct a 2D single mode RT simulation with periodic boundary conditions over a domain ranging from -0.25 to 0.25 in x and reflecting walls over a range of -0.75 to 0.75 in y. The initial perturbation is a velocity perturbation following the setup provide at `http://www.astro.princeton.edu/~jstone/Athena/tests/rt/rt.html` with $v_y = 0.0025(1 + \cos(4\pi x)(1 + \cos(3\pi y))$. The interface is at $x = 0$ with an upper density of $\rho_H = 2$ and lower density of $\rho_L = 1$. The pressures are initialized to maintain hydrostatic equilibrium with $P = 2.5 - 0.1 * \rho y$ with gravity = -0.1. The adiabatic index $\gamma = 1.4$. The resolution is 50 by 250 cells.

Table 3.2: Relative L1 errors for the entire domain between the FLASH base simulation and FT simulation relative to the exact solution. Resolution ranges from 50 cells to 1600 cells. The FT simulation seems to show a slight advantage over the base FLASH simulation.

Grid Resolution	Relative L1 error		Convergence Order	
	Base FLASH	FLASH with FT	Base FLASH	FLASH with FT
50	0.0183	0.0152	-	-
100	0.0108	0.0111	0.76	0.45
200	0.0057	0.0056	0.92	0.99
400	0.0031	0.0030	0.88	0.90
800	0.0019	0.0017	0.71	0.82
1600	0.0008	0.0005	1.25	1.77

Table 3.3: Relative L1 errors for the region bracketing the contact discontinuity. Resolution ranges from 50 cells to 1600 cells. The FT simulation has an average relative error around 5 times better than the base FLASH simulation for this region.

Grid Resolution	Relative L1 error		Convergence Order	
	Base FLASH	FLASH with FT	Base FLASH	FLASH with FT
50	0.1081	0.0201	-	-
100	0.0541	0.0145	1.00	0.47
200	0.0294	0.0076	0.88	0.93
400	0.0173	0.0038	0.77	1.00
800	0.0104	0.0019	0.73	1.00
1600	0.0055	0.0009	0.92	1.08

In Fig. 3.3 we plot the FLASH simulations with (right) and without (left) front tracking coupled in through the API. The plot is shown at a time corresponding to $t = 10$s, well into the non-linear regime. Both simulations show similar macro structures relative to growth of the instability and shape suggesting the API has been installed successfully. Some clear advantages of front tracking are observable when comparing the two simulaitons. The front tracking simulation has no numerical diffusion and is overlayed by the tracked front. Additional small scale details are visible in the front tracked solution, which as a result of the numerical diffusion in the base FLASH simulation are not resolved. Also, the front tracked solution has a better shape, a different length scale for the bubbles and spikes and eliminates the dip observed at the top of the bubble. These highlight some of the key reasons front tracking has been able to perform better with regard to RM and RT instability modeling.

3.3.3.3 Rayleigh-Taylor Multi Mode

Here we analyze A to B comparisons of a 2D multi mode RT simulation with an initial random perturbation. The domain is a square box with both x and y ranging from -0.25 cm to 0.25 cm. The configuration is similar to the single mode RT problem described above with densities of 1 g/cc and 2 g/cc, hydrostatic pressures and a gravity of -0.1 cm/s^2. The boundary conditions are periodic in x and reflecting in y with $\gamma = 1.4$.

The initial perturbation consists of random amplitudes, phases and mode numbers selected from a mode number range of 8 to 30. The amplitudes are scaled to produce a maximum initial perturbation amplitude of 0.003 cm. Since the smallest wavelength λ is 0.0167 cm, the amplitude is $\approx 0.2\lambda$ or starting just outside of the linear regime. The simulations are run with a grid resolution of 1000^2, providing ≈ 33 cells of resolution for the smallest initial wavelength.

In Fig. 3.4 we plot the FLASH simulation with (bottom) and without (top) front tracking coupled in. The plot is shown at $t = 2.75$s at which point bubble competition is beginning to start but the structures are still relatively coherent. It is immediately apparent one of

the major advantages of front tracking, as the top frame contains quite a bit of numerical diffusion acting at the interface between the two fluids. This numerical artifact is one of the primary concerns we are investigating in modeling of these instabilities in the ICF regime in Chapters 5 and 6.

Front tracking prevents this numerical diffusion and thus provides a role for a physical diffusion model to be coupled in to allow for physically consistent length scales associated with the diffusion processes in the problem of interest.

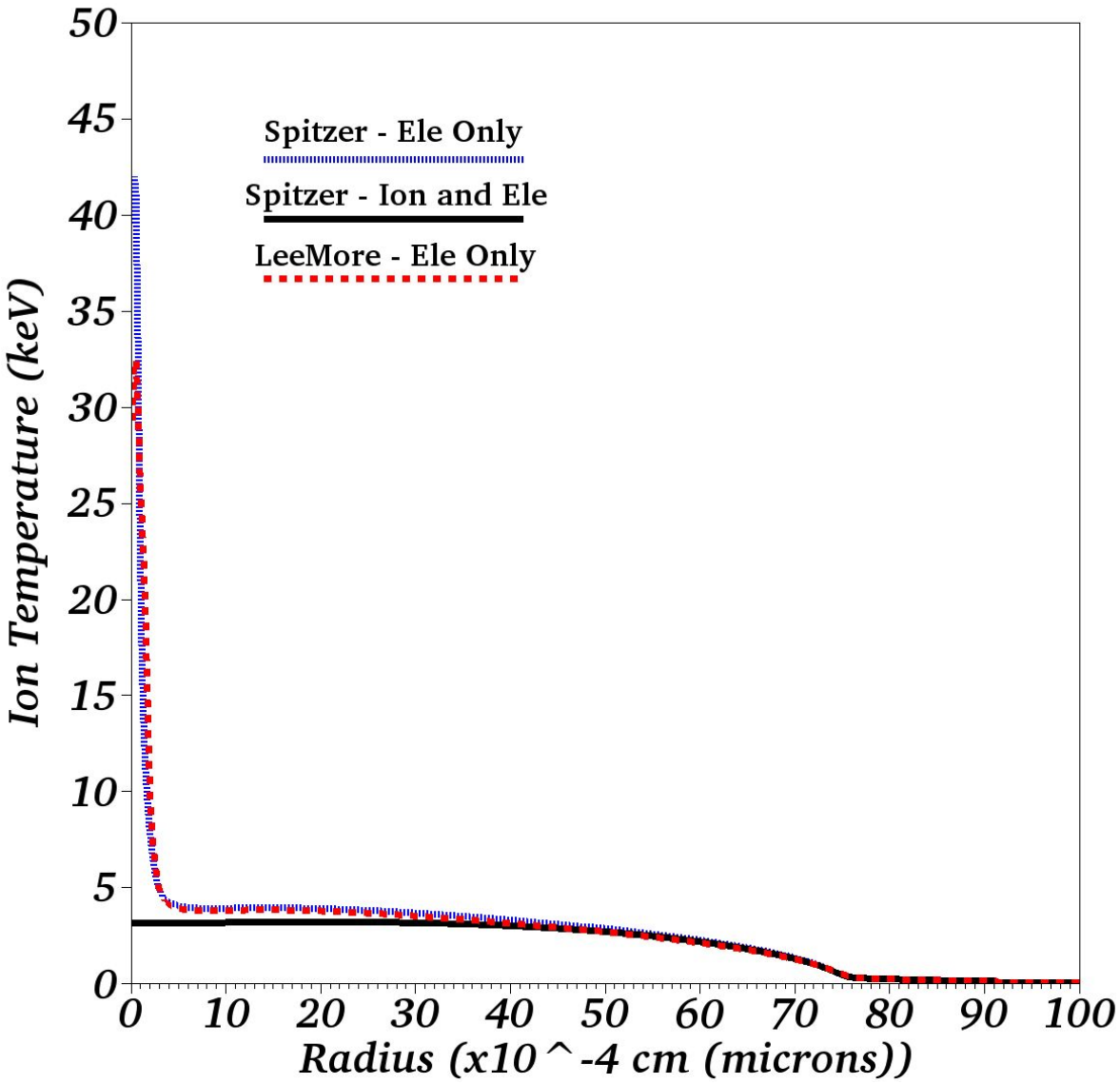

Figure 3.1: Comparison between thermal conduction models of Lee-More (red, dashed) and Spitzer (blue, dotted) for simulations run with only electron thermal conduction to the Spitzer model (black, solid) used for both electron and ion conduction. The use of the ion conduction model removes the unphysical spike in temperatures which persist from this point midway through the deceleration to nearly bang time. Since FLASH only has capabilities to use the Spitzer model for ion conduction and the inclusion of the ion conduction has a major impact, we use the Spitzer model in all simulations carried out in the remainder of this dissertation.

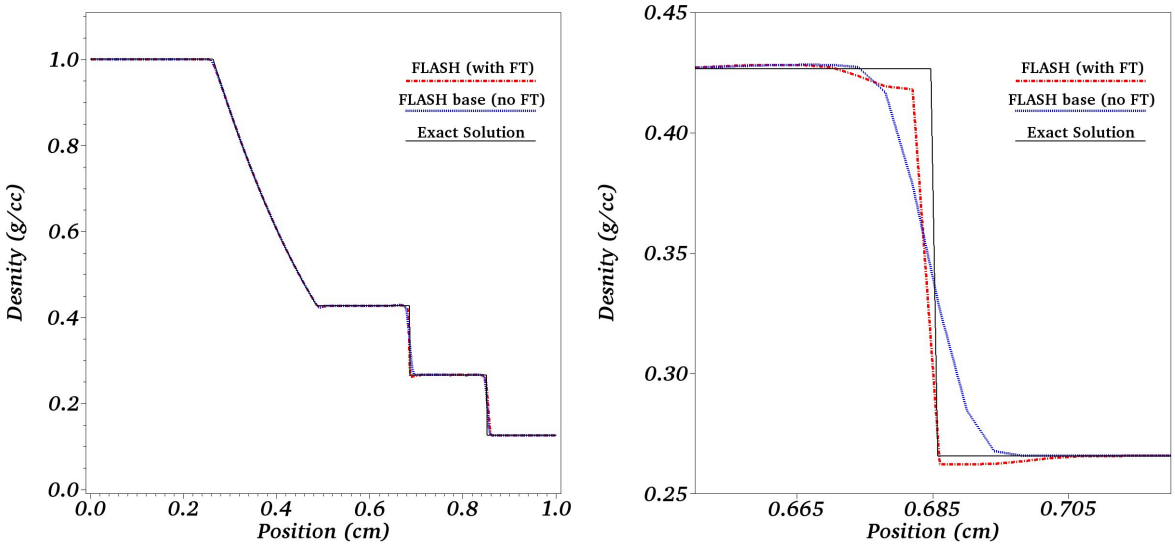

Figure 3.2: Sod shock tube simulation at t=0.2 using 250 grid cells in the x direction. The base FLASH simulation is the blue dotted line, the FLASH simulation with FT turned on is the red dot-dash line and the exact solution is the black solid line. Left: full domain and Right: zoomed in picture of the contact discontinuity, where front tracking has the major impact.

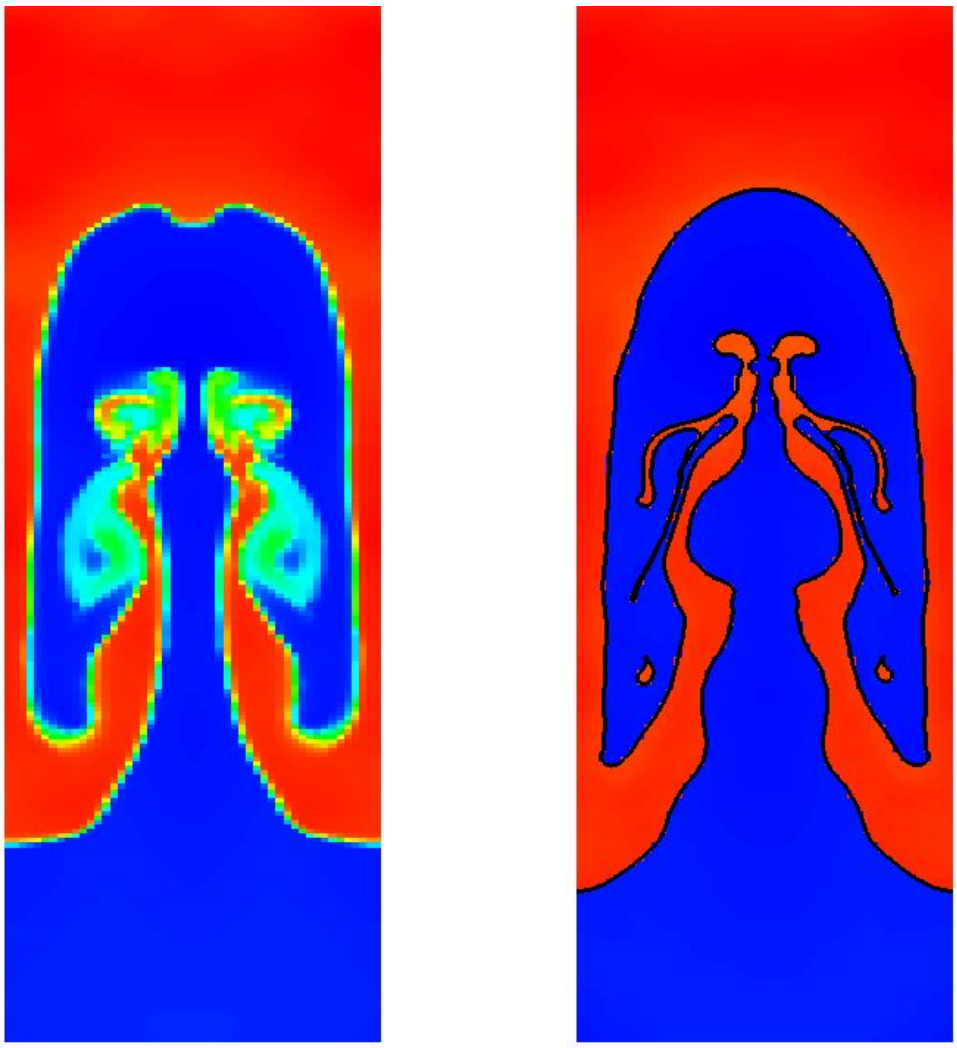

Figure 3.3: Rayleigh-Taylor single mode simulation at $t = 10$s. Comparison of FLASH run without front tracking (left frame) to a FLASH run with the use of the front tracking API (right frame). All diffusion occurring in the left frame is a result of numerical diffusion, prevented by the front tracking algorithm. The grid resolution is 50×250.

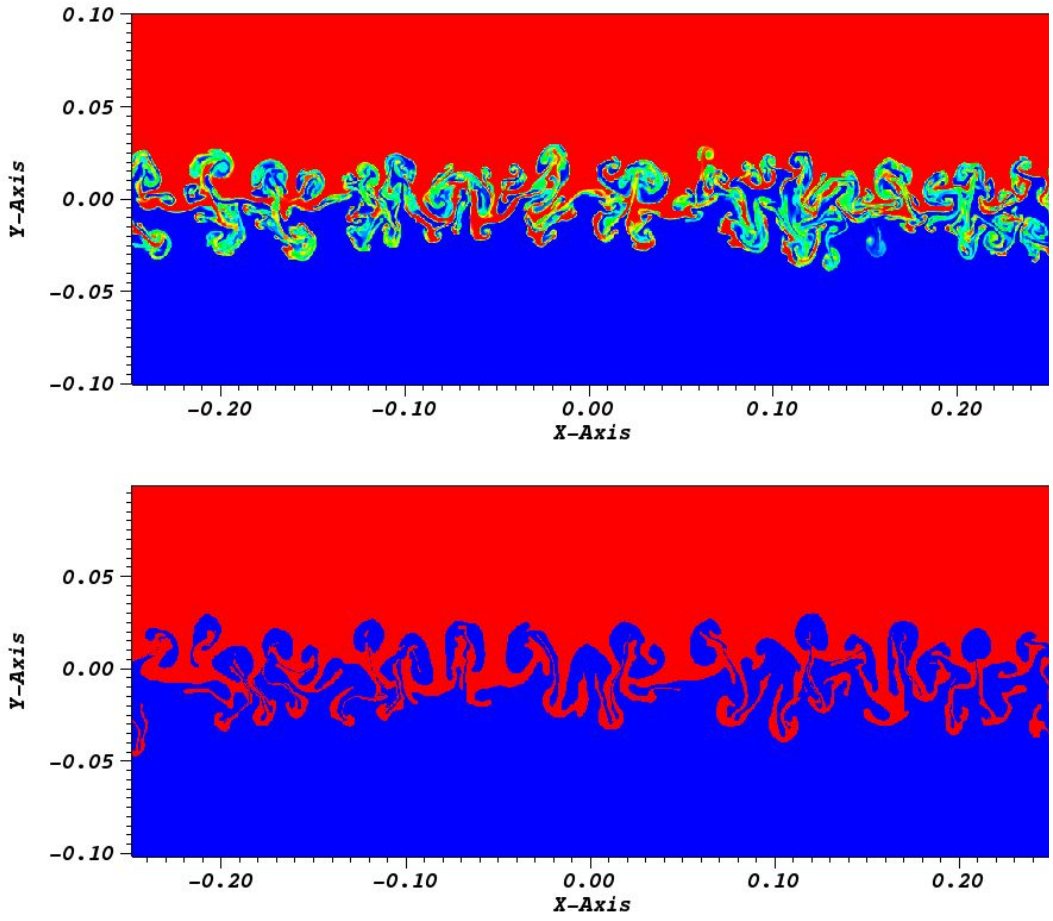

Figure 3.4: Rayleigh-Taylor multimode simulation at $t = 2.75$s. Comparison of FLASH run without front tracking (top frame) to a FLASH run with the use of the front tracking API (bottom frame). All diffusion occurring in the top frame is a result of numerical diffusion, prevented by the front tracking algorithm. The grid resolution is 1000×1000, providing ≈ 33 cells per smallest initial wavelength.

Chapter 4

Hot Spot Sensitivity to Adiabat

Our goal in this dissertation is to better understand the dynamics driving mix between the ablator material and the DT fuel during the ICF implosion and how they relate to observed discrepancies between simulation and experiment. Before we address those issues in Chap. 5 and 6, we analyze another possible cause of these discrepancies related to extra energy in the DT ice layer due to preheat in front of the shocks. The extra energy changes the adiabat and compressibility of the cold DT fuel, thus impacting the thermodynamics of the hot spot and potentially the mix. In numerical simulations, this effect is typically left out and Cheng et al. [11, 14] proposed it as a possible driver for thermodynamic differences between the simulations and experiments. We conduct simulations designed to understand the effects an added energy source can have on the thermodynamics and use this as a base of comparison between HYDRA simulations and the reduced physics model in FLASH. The first section, 4.1, has been reproduced from *Sensitivity of inertial confinement fusion hot spot properties to the deuterium-tritium fuel adiabat*, J. Melvin, H. Lim, V. Rana, B. Cheng, J. Glimm, D. H. Sharp and D. C. Wilson, Physics of Plasmas, **22**, 022708 (2015) [49], with the permission of AIP Publishing.

4.1 HYDRA simulations

4.1.1 Simulation Methodology

1D post shot HYDRA simulations of the ICF capsule were performed [17], with a radiation drive modified to match shot N120321 and a second set of simulations designed to match shot N120405. Initial simulations designed to match these shots were used to establish a baseline for the experimental quantities of interest. The baseline simulations (referred to as "Nominal" going forward) are run with a frequency dependent diffusion source and no premix initialized [17]. The radiation drives are designed to attempt to match key observables in the experiments.

In the entropy enhanced simulations, energy is added to the DT ice layer uniformly over the course of 2ns, between the third and fourth shocks. The energy is added spatially to the entire DT ice layer simultaneously per unit mass. The range of energy added is up to 100kJ/g. The goal of this added energy is to increase the adiabat (α) in the outer region of the DT fuel, typically referred to as the pusher [11] to the desired upper bound. The adiabat ($\alpha = P/P_{\text{cold}}$), which is defined as the ratio of DT pressure to the minimum DT pressure at a density of 1000g/cc (P_{cold}), can also be fit to the entropy, computed as part of the EOS package available in HYDRA, s [29].

$$\alpha = \left(1 + \exp\left(\frac{s - 0.455}{0.063}\right)\right)^{0.54} \tag{4.1}$$

Using this relationship, we find that the simulated adiabats increase in the outer region of the cold shell up to ≈ 2.30 for the highest entropy enhanced simulations relative to the nominal simulation values of ≈ 1.50. The adiabat is evaluated at the time of peak implosion velocity, defined dynamically within each simulation by a mass-weighted verge velocity over the DT fuel region. This increase in the adiabat, up to around 2.5 is required to match experimental data [11]. This higher adiabat in the experiment could be present from a

combination of sources. To name a few, hot electrons are believed to contribute in addition to plasma kinetic effects [1, 52], self generated electric fields [1, 52] and mixing between the DT fuel and ablator material [12]. Currently experiments are only able to verify the hot electrons but it is the opinion of the authors that the other effects contribute to drive the adiabat up as high as 2.6. In Fig. 4.1 left frame, we plot the fuel density at peak implosion velocity for the N120321 nominal simulation and in the right frame for the 50kJ/g added energy simulation. In the insets we show the adiabat as calculated in the outer region of the DT fuel. We see that the adiabat is increased in this pusher region under the addition of energy. The amount of energy added was chosen to allow the adiabat to range up to a value of around 2.5. In Sec. 4.1.2 we investigate the relationships between changes in the simulated adiabat, coupled with the nominal post shot simulations and the corresponding hot spot thermodynamics.

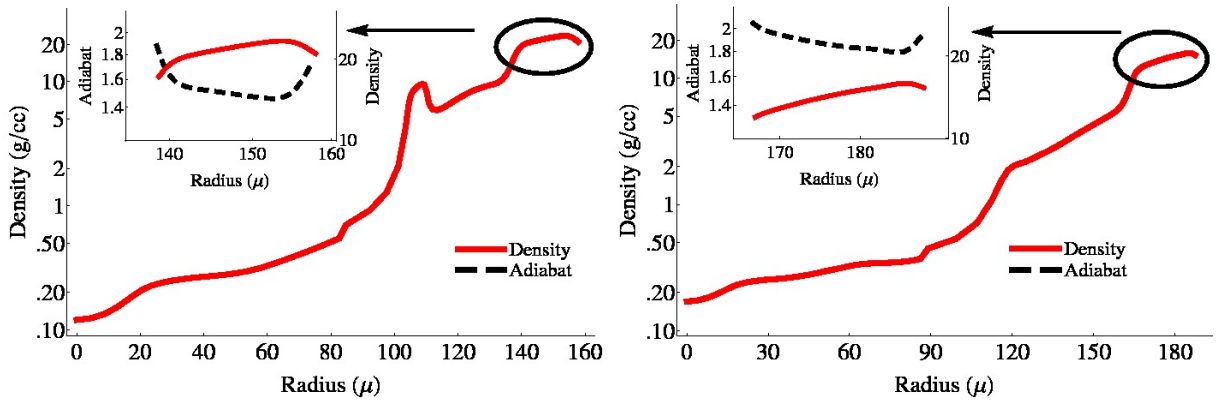

Figure 4.1: Fuel density profile at maximum implosion velocity for simulated shot N120321. Inset: Adiabat profile in the high density pusher. Left Frame: Nominal adiabat is approximately 1.5 for the high density pusher, Right Frame: 50 kJ/g increase to energy; adiabat is approximately 1.85 for the high density pusher.

4.1.2 Trends for Entropy Enhanced Simulations

We establish trends for the effects of initial entropy enhancement. Similar trends were observed between both the N120321 and N120405 sets of simulations. Since N120405 experienced a large amount of mix in its experiment, its nominal simulation is further away from experimental agreement. Since we do not couple a mix model into our 1D simulations, N120405 is not an ideal candidate to focus an analysis of the change in adiabat. Instead it would benefit more from the addition of a mix model and analysis to capture the capsule asymmetries. Thus, in this section we will focus our analysis on shot N120321. Instantaneous values are taken at bangtime (maximum neutron production rate), determined dynamically within each simulation from the burn calculation. The simulations are run without alpha heating, achieved by reducing the reactivity rates by three orders of magnitude. This is then rescaled at the end to represent a "no burn" bangtime and yield. This "no burn" calculation is chosen for our simulations to prevent the nominal case from achieving ignition. In addition, since the experiment chosen to model did not have significant yield to ignite, comparisons to a "no burn" calculation provide a better picture of the relationship between the experiment and the simulation. This methodology is consistent with other investigations into simulation to experiment discrepancies [17]. Our main result is the strong sensitivity of hot spot densities, pressures and yields, as well as predicted mix to additional entropy. Instantaneous ion temperatures decrease slightly and burn widths increase as the adiabat is increased. The size of the hot spot also increases as entropy is added. However, as this is affected by 3D mix, not coupled into the present simulations, a basis for direct comparison to experimental data is not apparent for the radius and thus we report, but do not draw any conclusions with regard to the behavior of the hot spot radius.

Fig. 4.2 shows the effects of added entropy into the cold shell relative to the nominal simulation of shot N120321. From Fig. 4.2 top, we observe clear trends towards lower densities in both the hot spot and the cold shell as the cold shell moves to a higher adiabat. In addition, an improved agreement of the hot spot density with the experimentally inferred

density is observed. To account for these density trends, we note that added energy in the cold fuel has the effect of introducing less compression, which lowers the hot spot density and increases the hot spot radius.

In Fig. 4.2 center frame, we compare the pressures among the entropy modified simulations and the corresponding experimentally inferred pressure. We observe that pressure is also sensitive to entropy enhancement and decreases as the entropy is increased. For the range of energies considered here, the hot spot densities and pressures come close to reaching their experimentally inferred values.

In Fig. 4.2 bottom frame, we compare the ion temperatures at maximum neutron time. When adding energy, we observe a slight decrease in ion temperatures at bang time. However, to facilitate ion temperature comparisons with experimentally inferred values, we present in Table 4.1 the burn weighted ion temperatures amongst the simulations conducted here and experiment N120321. We use the burn-weighted temperatures to approximate the nTOF (neutron Time of Flight) temperature calculation from the experiment, as all HYDRA simulations were run on the open network where the neutron transport module that could be used to estimate an nTOF calculation in HYDRA is unavailable. Typically, nTOF simulated temperatures are lower than the burn-weighted ones. Burn-weighted temperatures are calculated as an integral over time and space of the neutrons created multiplied by the temperature. We then divide by the total yield to get the overall burn-weighted temperature. We see that the burn weighted temperatures show a decreasing trend under modest amounts of added entropy.

In Table 4.1 we observe the trends of other experimentally relevant values under an increase in the adiabat. The neutron yield is calculated from the burn module with alpha deposition turned off. The areal density (ρr) is a burn weighted value, where the density is first integrated over the DT fuel region and then weighted by the yield calculated during that timestep. The DSR is directly calculated from the areal density using the common relation DSR = $\rho r/21$ [29]. The adiabat is calculated using the relation in Eq. 1. Finally, we also

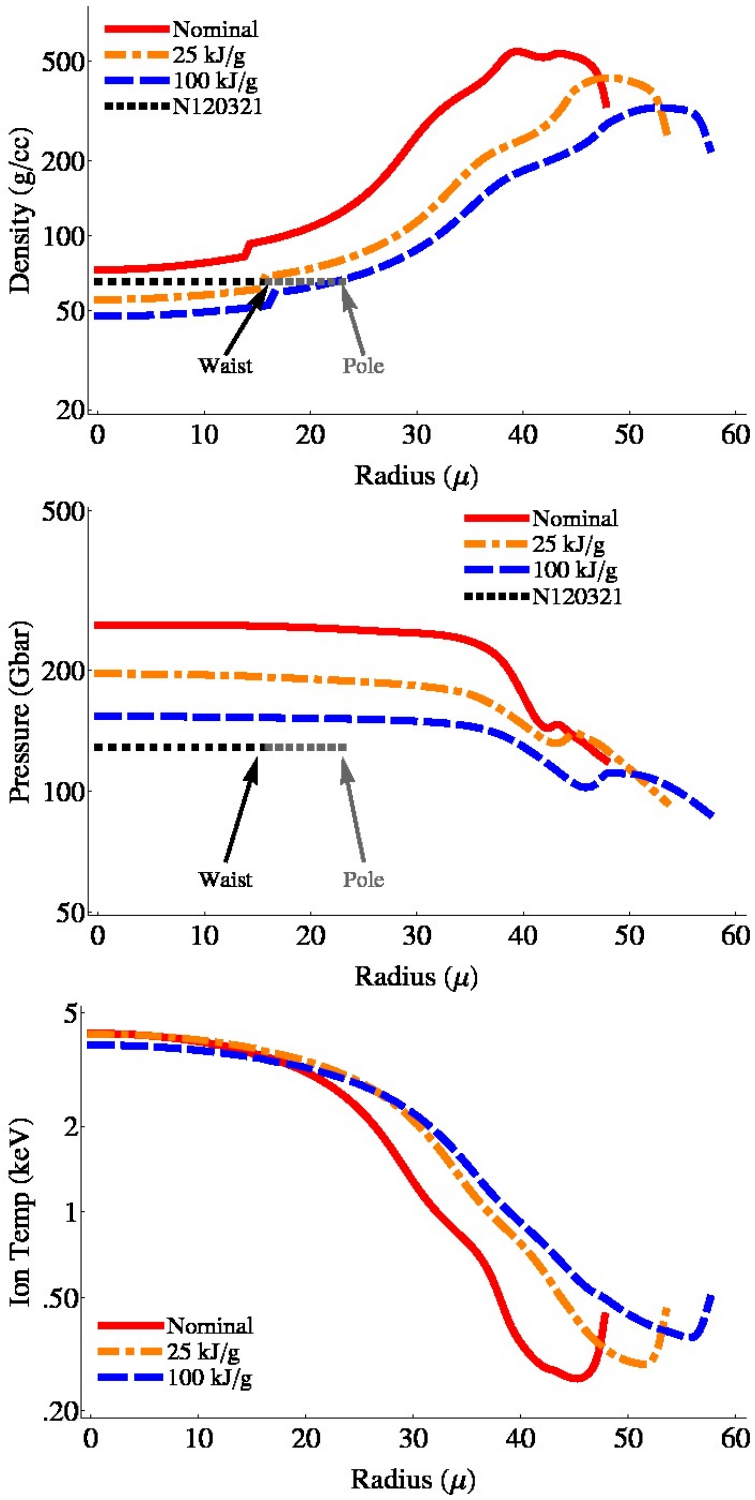

Figure 4.2: Post shot simulations of N120321 with added entropy to the cold shell. Top frame: Densities, Center frame: Total Pressure, Bottom frame: Ion Temperatures. Comparisons to the nominal simulation and experimental values for shot N120321 are shown [8]. The experimental waist and (larger) pole radii are shown separately.

Table 4.1: Experimental quantities and those observed in the simulations with various amounts of added entropy. Neutron yields, Down Scatter Ration (DSR), Burn weighted ion temperature, Total DT fuel areal density ρr, Adiabat and Burn Width are compared between entropy modified simulations and experiment.

Run (Name)	Yield (10^{14})	DSR (%)	T_i (keV)	ρr (g/cm^2)	Adiabat	Burn Width (ps)
N120321 [17, 8]	4.2	$6.26 \pm 0.46\%$	3.07 ± 0.14			136 ± 24
N120321 - Nominal	19.33	4.67%	2.95	0.98	≈ 1.50	123.8
N120321 - 25 kJ/g	16.85	3.69%	2.89	0.78	≈ 1.70	127.9
N120321 - 50 kJ/g	14.40	3.53%	2.80	0.74	≈ 1.85	135.7
N120321 - 100 kJ/g	12.62	3.22%	2.74	0.68	≈ 2.30	154.0

present the burn widths for the simulations in Table 4.1. The burn width or full width half maximum is defined as the time period during which at least 50% of the maximum neutron production rate is observed. The bang time is not included in Table 4.1. In all N120321 simulations, nominal and entropy enhanced, we observed the bangtime to be within a few picoseconds of 23.00ns, slightly larger than the experimental value of $22.91 \pm .04$ns. However, we note that adding entropy has the effect of flattening out the burn and thus causing the burn to begin earlier in time, with the bangtime behaving more like a random variable with a small variance. Defining the beginning of the burn as the point at which at least 50% of the maximum neutron production rate is first observed, we see a trend from 22.92ns for the nominal case to 22.89ns for the 100kJ/g case.

High foot experiments tend to observe higher temperatures than the low foot shots presented here [58]. The fact that we do not meet this observed experimental trend could be a result of additional physical relationships between the high foot drive and ion temperatures,

such as a stronger shock in the the high foot implosions. Since these are not present when simply adding energy to increase the adiabat, we don't expect to see the same relationship. We believe the decrease in ion temperature under addition of entropy is a result of the hot core compressing less in the modified entropy simulations. Since energy is only added to the cold DT fuel, the temperature of the hot core decreases as we add additional entropy. In some variables, DSR and total yield for instance, we see downward trends, consistent with that observed in high-foot experiments [58]. In other variables, burn-weighted temperatures and bang times, the trend we observe through added entropy is not the same as that observed in the high foot experiments. Relative to the low foot shot in question, N120321, we observe improvements in neutron yield, densities and pressures, with the burn width staying in the experimental error bars. However in the other variables, our modified simulations produce values which diverge from the experimental values. This fact suggests additional effects such as mix, 2D and 3D effects, asymmetries and other incomplete physical models play a role. The success of positive trends in some of the experimental quantities is, in the authors' opinions, suggesting of a role to play by the adiabat in the cold shell. We believe that further investigation into this avenue is warranted and could help contribute to future improvements in the comparison of simulation to experiment.

4.2 FLASH simulations

Using FLASH we conduct 1D simulations of the RT deceleration phase only, initialized off of the nominal HYDRA simulation, run without preheat. To account for the added energy, we add energy at the time of initialization into the DT ice regions of the capsule and the time dependent boundary conditions taken from HYDRA. Since the simulations are only of the deceleration phase, we use a Lagrangian boundary point that represents the edge of the DT ice region.

In Fig. 4.3 we present a companion figure to Fig. 4.2 which shows the impact the added energy has on the 1D hot spot thermodynamics. FLASH shows relatively good agreement

with HYDRA for the base case when simulated for this short 500 picosecond interval representing the deceleration phase. The main discrepancy in the FLASH simulations is the elevated temperatures which cause diagnostics such as those compared in Table 4.1 to be far away from their experimental counterparts. Thus, as expected, FLASH is not able to perform better with regard to diagnostics than HYDRA and so we focus solely on the trends present in the parameter study of added energy. The added energy in FLASH was done by increasing the ion temperature variable by a specified quantity (20eV, 40eV) which produce a roughly similar effect to the 25 kJ/g and 50 kJ/g energy added to the HYDRA simulations.

The trends observed in the FLASH simulations are qualitatively consistent with those in HYDRA and thus similar conclusions can be made through the FLASH simulations even with the reduced physics model present. The main conclusion we can draw from the plots is that the change in the adiabat through a preheating mechanism can produce thermodynamic changes in the hotspot that would create a reduced neutron yield and bring simulations closer to the observed experimental quantities.

We conclude from this analysis that by focusing on the trends present in on-off A/B comparisons carried out in the remainder of this dissertation, FLASH will be successful in representing how observed trends would fare in simulations run in a similar fashion in HYDRA. Since the source code for HYDRA is not available to the authors, the added functionality we are interested in exploring can only be implemented in an open source software package like FLASH. It is the opinion of the authors that the qualitative analysis presented in this section verifies that trends observed in FLASH should result in similar trends in other simulation codes like HYDRA.

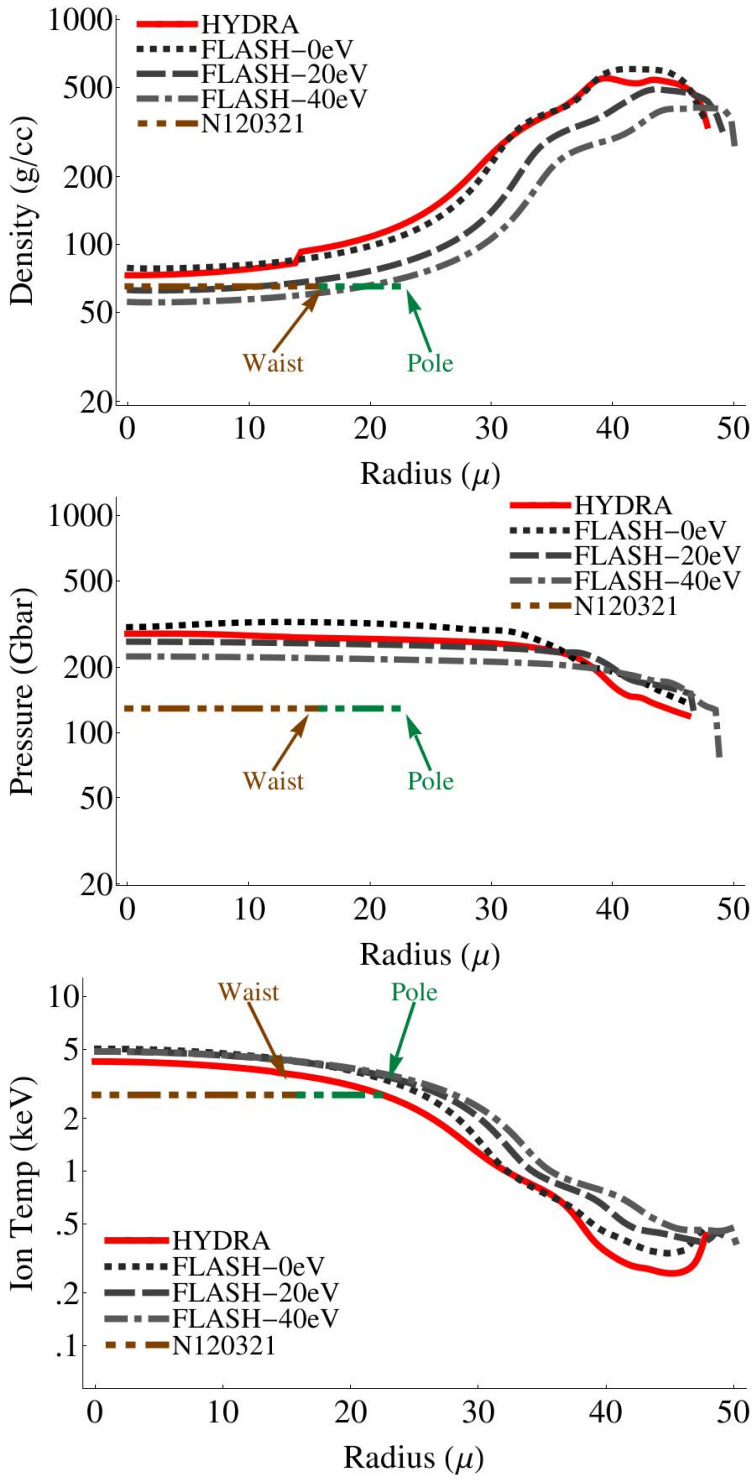

Figure 4.3: 1D FLASH simulations of N120321 with added energy to the cold shell region at initialization. Top frame: Densities, Center frame: Total Pressure, Bottom frame: Ion Temperatures. Comparisons to the nominal HYDRA simulation and experimental values for shot N120321 are shown [8]. The experimental waist and pole radii are shown separately.

Chapter 5

1D Simulations

In the prior section, Sec. 4.2, we saw that FLASH was able to reproduce a study conducted in HYDRA to show that modifications to the adiabat in the cold shell resulted in trends towards lower neutron yields and better agreement between simulation and experimental observables. This persisted across both FLASH and HYDRA despite differences in their computational models. In this chapter we start our study of 1D simulations earlier in FLASH, at the beginning of the RM phase, around 14.5ns. As we are now relying on FLASH to simulate a longer time frame where radiation physics has a larger role in the driving forces, FLASH's reduced computational model will have a more apparent impact on the late time thermodynamics and thus any diagnostic quantities. In addition, the approach used for modeling of the boundary conditions has a more significant effect over the extended simulation time. As the location of the Lagrangian boundary point moves in the FLASH simulation, it is then reset to match the location of the associated Lagrangian point in the HYDRA simulation. Thus it is not tracking a Lagrangian point relative to FLASH. As the FLASH simulation calculates larger velocities in the early stages the computational region extends allowing for more CH to remain in the shell as there is no physical model to allow for FLASH to ablate this material. Thus, we get more mass remaining in the shell (upwards of 20%) at bang time and more inertia, causing slightly more compression than the companion HYDRA simulation. Thus, our FLASH simulations are no longer a good model for shot

N120321, but are instead more representative of the ICF regime as a whole. Additional boundary conditions were explored to attempt to improve the modeling, but this approach was found to be most consistent with the dynamics of the HYDRA simulation across the 1D and 2D runs. Since we are mainly concerned with numerical effects and mixing, which are sensitive to the dynamics, this approach to modeling the boundaries was chosen.

For this reason, our focus in the rest of this work is on A to B comparisons where we turn on or off an additional computational model and determine its impact in the ICF regime. As these models (Front tracking and mass diffusion) require modifications to the source code, our only vehicle for these studies is FLASH.

One of the major concerns for Eulerian based numerical models is that as material is advected across the boundary between computational cells, an unphysical numerical diffusion process occurs. Many approaches are used to remedy this from adaptive mesh refinement (AMR) schemes [2] to interface reconstruction methods like volume of fluids (VOF) [55]. Unlike the other methods, front tracking, which we use for our studies here, completely eliminates the unphysical numerical diffusion.

To investigate the resulting benefit for ICF like simulations using an Eulerian computational framework, we conduct two sets of 1D calculations, one using the base FLASH configuration (referred to as F-BASE) and one using the base FLASH configuration with front tracking enabled at the DT-ablator interface (referred to as F-FT). We find two main results.

1. Due to the convergent nature of ICF simulations, numerical diffusion on reasonable 3-dimensional Eulerian grids ends up extending over a meaningful fraction of the computational domain remaining at bangtime, from $\approx 2\%$ on the finest grids considered here in 1D to $\approx 15\%$ on the coarsest grids. A mitigation strategy to prevent this numerical diffusion is desired to allow for qualitatively correct solutions and front tracking is shown to accomplish this on all grids.

2. When front tracking is added to remove numerical mass diffusion, the effects of physical mass diffusion can be studied. We find that the addition of an ICF applicable mass diffusion model shows no meaningful length scales when added on top of FLASH and front tracking, emphasizing that for a physically realistic ICF simulation there should be little to no mass diffusion, whether numerical or physical.

5.1 Pseudo-1D vs. Pure 1D

In its current iteration, the FTAPI does not support a 1D configuration. Since we are interested in comparing 1D physics, the F-FT runs were all run in a 2D configuration with 8 computational cells in the theta direction and an initialization profile that is a function of radius only. We refer to this as a pseudo-1D simulation. In theory, these pseudo-1D runs should be identical to a corresponding pure 1D simulation, as only 1D physics is present in the computational model. However, a few factors contribute to make these runs differ slightly. In the pure 1D simulations, since there are no computational cells in the theta direction, there are no theta velocities present. However, in the pseudo-1D simulation, small errors in the discrete representation of the geometric terms used in the radiation diffusion and thermal conduction implicit solvers produce small theta velocities during the simulation. These velocities are typically around four orders of magnitude smaller than the radial velocities and thus have a very minor effect on the simulation. These small velocities also cause small differences in the calculated timestep, which due to our time and space dependent boundary conditions, cause a slightly different representation of the state at the boundary. Since the boundary is the main driver for the simulation, this also contributes a minor difference. All of these minor errors contribute to a small, but not negligible difference, between a corresponding pure 1D simulation and pseudo-1D simulation.

To legitimize the comparisons that will be carried out between F-BASE simulations using a pure 1D configuration and F-FT simulations using a pseudo-1D configuration, a baseline for the errors between a corresponding pure 1D and pseudo-1D simulation needs

to be established. In Fig 5.1 we plot an F-BASE simulation using both the pure 1D and pseudo-1D simulation strategies at approximately bang time. The figure suggests that only minor differences arise between the two simulations and that direct comparisons between the two simulation strategies is meaningful. To quantify the extent of the differences, the two simulations were compared using a relative L_1 error, as in Eq. 3.8, where instead of an exact solution, the 1D simulation was used in place of the exact value in that formula. The relative L1 error was found to be 0.013 which equates to an average error of about 1% between a corresponding pure 1D and pseudo-1D simulation.

5.2 Mesh Convergence

With a baseline error between the pure 1D and pseudo-1D models determined, we analyze the convergence of the bang time density profile for the F-BASE simulation. In the left frame of Fig. 5.2 we plot four levels of mesh resolution. The coarse grid (blue, dot-dash) has a resolution of $\approx 0.50\mu$m, the medium grid (red, dash) has a resolution of $\approx 0.25\mu$m, the fine grid (green, solid) has a resolution of $\approx 0.167\mu$m and the very fine grid (dark gray, dotted) has a resolution of $\approx 0.125\mu$m. From the figure it appears that at a resolution of $\approx 0.25\mu$m the density is nearly converged. In addition, while the coarse grid has certainly not converged, structurally it appears similar to the converged solution. The key features that are different, i.e., the wave positions and peak densities in the cold shell, have an error of around 7% and around 12.5%, respectively.

Both of those errors improve in the coarse grid F-FT simulation, shown along with the FT medium grid simulation and the F-BASE very fine simulation in the right frame of Fig. 5.2. The peak density error between the F-BASE very fine solution and the F-FT coarse grid (0.5μm) simulation improves to $\approx 7.4\%$ from the $\approx 12.5\%$ on the comparable F-BASE coarse grid simulation. The location of the peak density position dramatically improves using the F-FT configuration from an $\approx 7\%$ error to $\approx 1.5\%$.

To assess the overall improvement, we again use the relative pointwise L1 error analysis

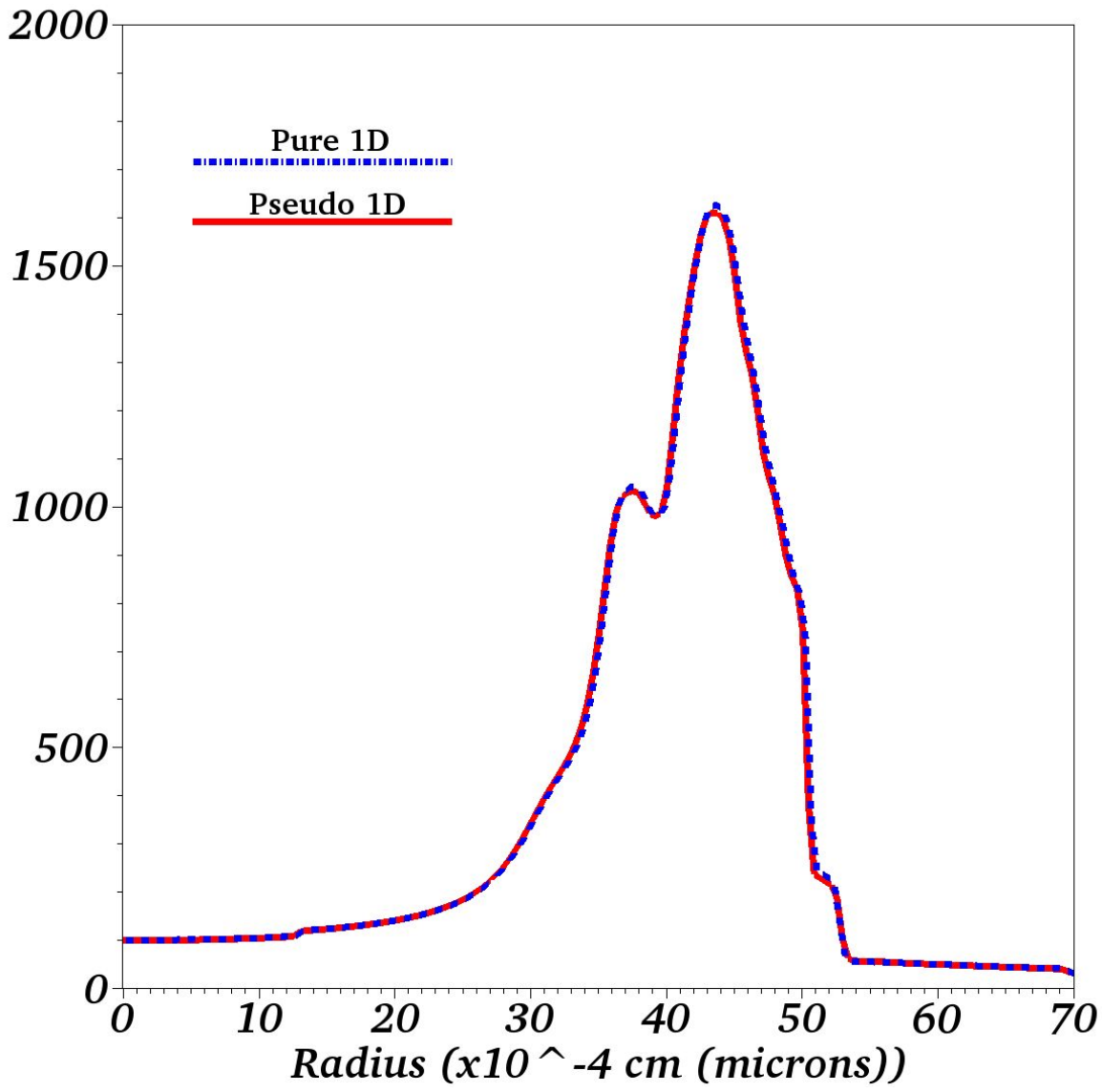

Figure 5.1: Fuel density profile for an F-BASE simulation at approximately bang time using both a pseudo-1D (red, solid) and pure 1D (blue, dashed) simulation strategy suggesting that these configurations can be interchanged with only minor errors. These simulations have a resolution of $\approx 0.42\mu$m per cell.

of Eq. 3.8 using the very fine F-BASE simulation as the "exact" solution. In Table 5.1 the convergence of the density for the F-BASE simulations are calculated. The convergence order recovers a nearly 3rd order convergence rate for the finest grid levels, matching the

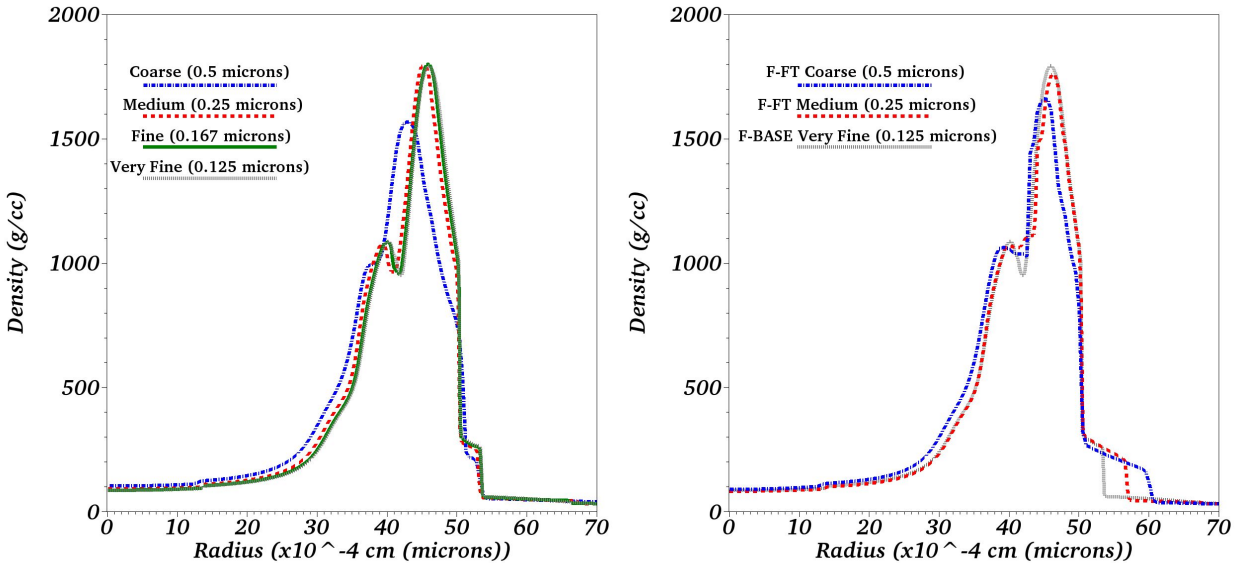

Figure 5.2: Fuel density profiles at approximately bang time. Left: Mesh refinement for the F-BASE simulations over 4 different resolutions. The solution appears converged using a grid resolution of $\approx 0.25\mu$m and results obtained using the resolution of $\approx 0.5\mu$m should still be meaningful. Right: Comparison of the $\approx 0.5\mu$m and $\approx 0.25\mu$m F-FT simulation to the very fine $\approx 0.125\mu$m F-BASE simulation. Improved agreement in the use of the coarse grid is obtained when front tracking is coupled into the FLASH solver. The F-FT and F-BASE simulations are converging to similar solution profiles.

underlying accuracy of the 3rd order PPM interior solver being used in FLASH. To compare the F-FT simulation on the coarsest grid, we calculate in Table 5.2 the error associated with both the F-BASE and F-FT simulations relative to the very fine F-BASE simulation. The first column quantifies the error over the entire domain, where the F-BASE simulation outperforms the F-FT simulation on average. However, a review of the right frame of Fig 5.2 shows that the major error between the F-FT and F-BASE simulations occurs in the wave furthest from the origin, behind the hot spot and cold shell, and thus not in a region of interest. With this in mind we reanalyze the error over the hot spot and cold shell regions only, from 0 to 50μm and tabulate the errors in the second column. As the figure suggests,

Table 5.1: Relative L1 errors for the density profile at bangtime for a mesh convergence study using F-BASE, taking the very fine grid solution as the "exact" solution. The solution appears to nearly converge at the medium grid relative to the key features desired. The convergence order once the solution has converged retains its 3rd order converge of the underlying interior PPM solver in FLASH.

Resolution	Relative L1 error	Convergence Order
F-BASE Coarse (0.50μm)	0.199	-
F-BASE Medium (0.25μm)	0.077	1.37
F-BASE Fine (0.167μm)	0.023	2.98

the coarse F-FT simulation has around a 10% error on average in the hot spot and cold shell regions, almost a 3× improvement over the similar resolution F-BASE simulation. From this analysis we identify two facts.

1. A resolution of $\approx 0.25\mu$m is needed to achieve near mesh convergence. In the capsule designs that are under study here, namely low foot NIC campaign capsules using a CH ablator, the design specs are for a capsule that is around 1150μm [29]. This implies that upwards of 5000 computational cells in the radial direction would be necessary to achieve that resolution. Certainly in 1D, that is not a problem. For 2D simulation, depending on the needed resolution in the angular direction and the availability of computational resources, this should also be fairly reasonable. However, in 3D, if we use the benchmark simulations of Clark et al. [18] as a guide, 1000 cells in both angular directions were used in their 3D simulations. Coupled with 5000 grid cells in the radial direction, that would be a requirement of 5×10^9 computational cells. Clark et al. reports that for their 3D HYDRA simulations, using a $400 \times 1000 \times 1000$ grid (they only need 400 cells since HYDRA is a Lagrangian code), $\approx 4.5 \times 10^6$ CPU-hours were needed to complete a single simulation.

Table 5.2: Relative L1 errors between the coarsest F-BASE and F-FT simulations relative to the F-BASE very fine solution profile. Over the entire domain (left column) the coarse F-BASE solution has improved agreement. When isolated to the area of interest (hot spot and cold shell), the F-FT solution drastically improves relative to the F-BASE solution, achieving a nearly 3× improvement in relative error.

	Entire Domain	Hot Spot and Cold Shell (0-50 μm)
Coarse F-BASE	0.199	0.270
Coarse F-FT	0.276	0.103

For high resolution 3D simulations carried out on Eulerian grids, we use the simulations carried out by Haines et al. [31], using Los Alamos National Lab's RAGE code [25] as a guide. Due to the cost prohibitive nature of a full 3D simulation, these simulations used a 2D-3D simulation strategy where the capsule is first simulated in 2D and then at the point when 3D physics become most important, the 2D simulation is rotated into 3D and completed. These simulations are of Omega capsules which are direct drive ICF experiments performed on the Omega laser in Rochester. These capsules are only around 450μm, about 2.5 times smaller than the NIF capsules discussed here. In addition, RAGE employs an AMR strategy for dynamic refinement of the computational grid around areas of interest. With all of these advantages, the 3D portion of these simulations still use over 1×10^9 computational cells using a base resolution of 0.5μm and refining as needed from there. These strategies can be used for a single production simulation, but for a full comprehensive parameter study or sensitivity analysis study, the requirements needed for a fully resolved 3D simulation is cost-prohibitive. This brings us to our second conclusion.

2. Even in 2D, a fully converged 5000 (or higher) × 1000 grid can be rather cost prohibitive and thus the ability to simulate with under resolved features is necessary to be able to

contribute meaningfully to the understanding of these ICF experiments. Consequently the need to develop effective computational strategies at coarser, non-converged grids that allow the capturing of important physical effects for the problem under study are beneficial. This emphasizes one of the benefits from the use of front tracking in the F-FT simulations, especially when used in an underresolved simulation. The coarse grid F-FT simulation does a better job of capturing the wave positions and has a smaller error in the peak density of the cold shell, relative to the converged F-BASE and F-FT solutions. Since the main focus of this work is to investigate mixing during hydrodynamical instabilities, the shock timings and wave speeds, as well as the density gradients and hot spot configuration are most important to that analysis. Thus, our strategy going forward is to use the F-FT simulations as a check on the convergent properties of the F-BASE simulation by doing A to B comparisons at the coarsest grid level. We believe this is justified by this analysis and would be an applicable strategy for other simulation codes using our designed API, with a reference implementation in FLASH described in Sec. 3.3 and code available at the website referenced therein.

5.3 Numerical Concentration Diffusion

The reason the F-FT simulations are better able to capture the converged solution is two fold. First, the tracked front can be thought of as an infinite resolution at the tracked surface and thus is the realization of infinite refinement in an AMR or mesh refinement process. This allows for the important dynamics at this interface to be completely resolved by the front tracking algorithm and thus an improvement in the simulation is observed. The second, which is a byproduct of the first, is the ability of front tracking to remove all numerical diffusion at a tracked front, similar to what occurs at every cell boundary in a Lagrangian formulation such as in HYDRA.

To emphasize the impact of this, in Fig. 5.3 we plot the normalized carbon concentration profiles at approximately bangtime for the F-FT coarse and various resolution F-BASE

simulations. With the exception of a slight change in position between the mesh refined F-FT simulations and the coarse grid plotted here, the coarse grid F-FT is a very good representation of the converged F-FT solution in the concentration variable. This is one of the primary advantages of front tracking, which for all mesh resolutions provides infinite resolution at the tracked discontinuity. The carbon concentration is a good representation of the fraction of ablator material in various areas of the capsule and is here normalized by the maximum carbon concentration at initialization of 42%. At our coarsest resolution of 0.5μm, numerical diffusion at the 20% carbon contour is $\approx 4.5\mu$m ($\approx 20\%$ of the compressed capsule at bang time) or about 9 grid cells. For the more refined simulations, similar relative distances of about 8-9 grid cells of numerical diffusion persist.

If the ablator material begins to diffuse into the cold shell region it can have two main effects. The first is an altering of the wave structure and compressibility as can be observed in Fig. 5.2 when comparing the F-BASE coarse grid with excessive numerical diffusion to the F-FT coarse grid with no numerical diffusion, which agrees much better on these two datapoints with the converged F-BASE simulations. The second will be explored in more detail in Chap. 6, but focuses on the fact that the deceleration phase RT instability has a much larger impact and more severe growth in the middle regions of the shell than at the fuel-ablator interface. Thus the further the ablator material diffuses inward, the more it is caught up in the strong RT instability and thrown forward towards the hotspot. As the design specifications of the NIC ICF capsules call for no more than 100ng of ablator material to be allowed to mix into the hotspot [29], it is important that any mixing observed in simulations be the result of a physical process. This will allow studies aimed at mix minimization.

5.4 Physical Concentration Diffusion

With front tracking in use and numerical diffusion removed from the contact discontinuity between the fuel and ablator, a physical diffusion model can be added to determine a

physical penetration of the ablator material into the DT fuel. We conduct a similar set of 1D FLASH simulations with the addition of front tracking and the physical mass diffusion model of Daligault [21], which we will refer to as F-FTMD.

In Fig. 5.4 we plot at bangtime, both the F-FTMD and F-BASE normalized carbon fractions as a function of radius for the 0.5μm resolution simulations. The addition of a physical mass diffusion model allows a small amount of diffusion at this fuel-ablator interface, but it is minor compared to the numerical diffusion present in the untracked simulation. We find that no meaningful difference is observed between our F-FT and F-FTMD simulations with regard to important observables such as density and temperature in the hotspot. As a result, we choose to exclude mass diffusion from our 2D studies carried out here. A more in depth study on the sensitivity to mass diffusion and other transport terms is the focus of ongoing work.

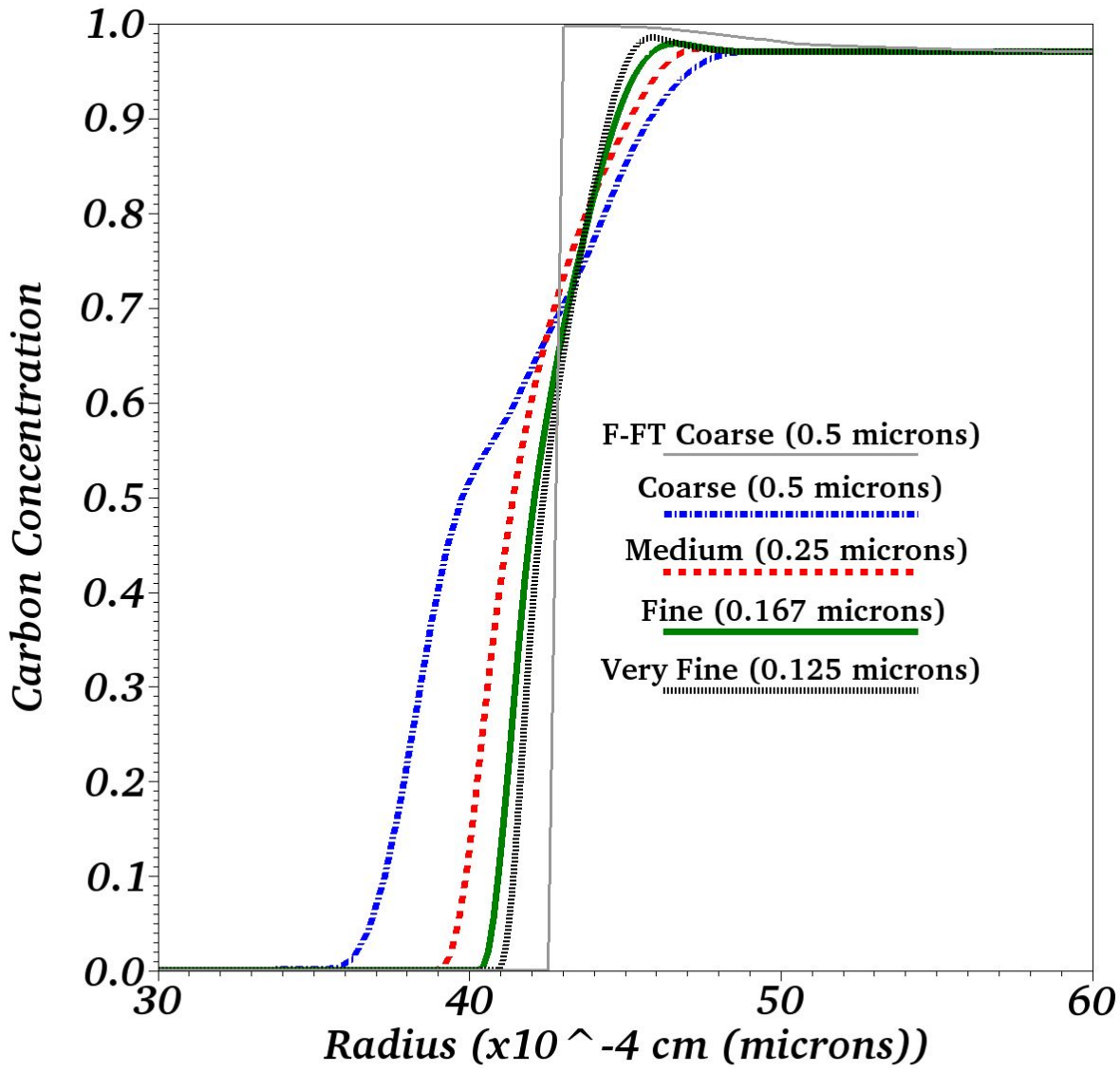

Figure 5.3: Carbon concentration as a function of radius for our 1D F-BASE mesh refinement study overlayed against the F-FT coarse grid solution. At the coarsest grid (blue, dot-dash) of $\approx$ 0.5μm, numerical concentration has resulted in about a 20% penetration distance relative to the size of the capsule at bang time. As the mesh is refined the medium grid $\approx$ 0.25μm (red, dashed), fine grid $\approx$ 0.167μm (green, solid) and very fine $\approx$ 0.125μm (black, dotted) grid maintain a consistent 8-9 grid cells of numerical mass diffusion persists. The front tracking solution on all grids (gray, solid), here the coarse grid solution, maintains the sharp discontinuity as a key feature of its algorithm.

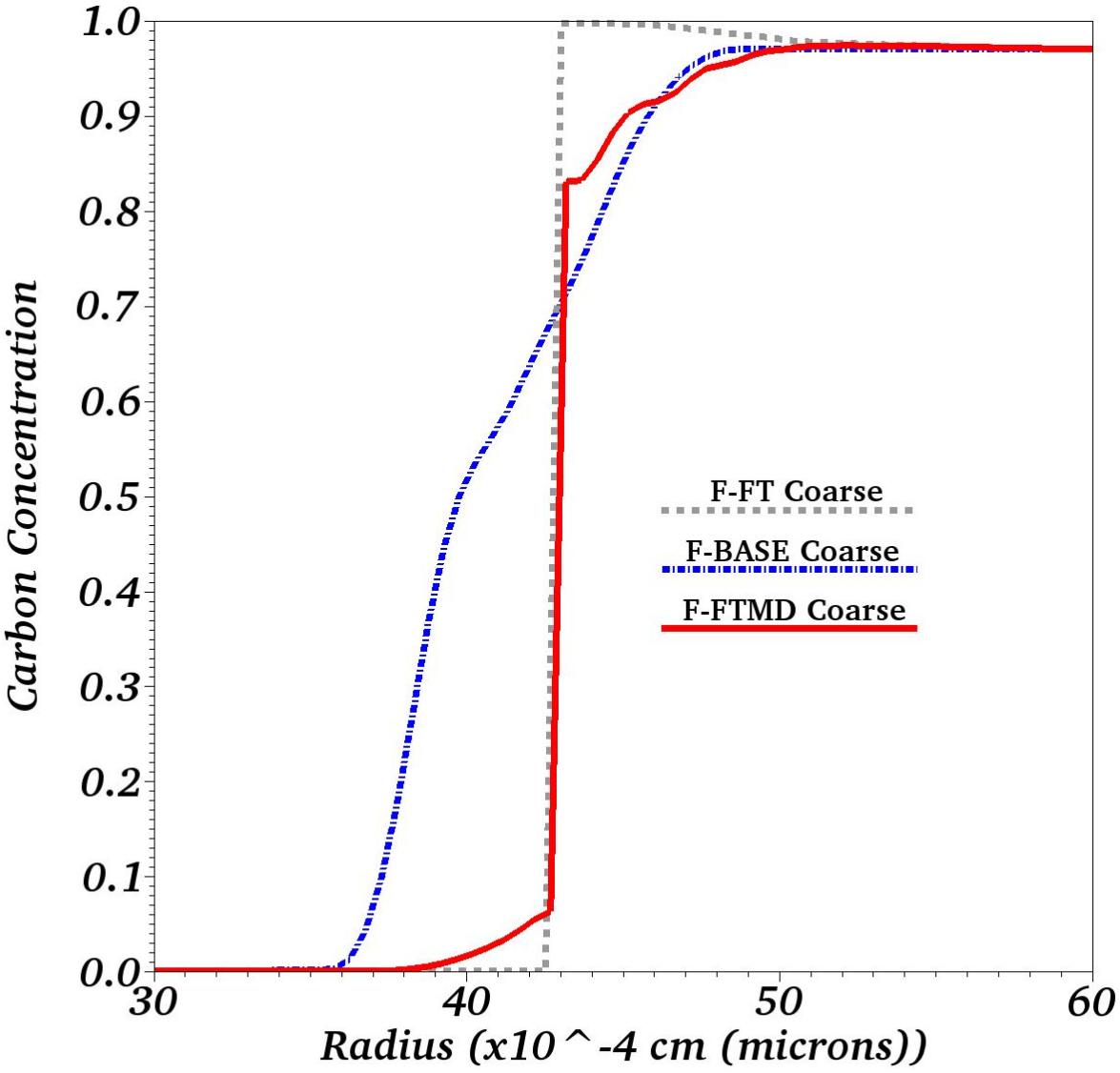

Figure 5.4: Normalized carbon concentration as a function of radius for the 1D F-BASE (blue, dot-dash) and 1D F-FTMD (red, solid) simulations at the coarsest grid ($\approx 0.5\mu$m). The physical mass diffusion produces a slight amount of mix across the tracked front, producing a slight elevation in the carbon percentage in neighboring cells. Relative to numerical mass diffusion, this has very little significance and shows very little impact on the overall simulation observables.

Chapter 6

2D Simulations

To fully study the interfacial instabilities and their impact on ICF capsules, multi-dimensional simulations seeded with perturbations are needed. While 3D simulations would be ideal, as discussed in Sec. 5.2, the computational cost for running a single simulation at a meaningful resolution can be prohibitive. Thus, we choose to study axially symmetric 2D simulations in a spherical geometry, which will allow us to explore the impacts of Front Tracking while exploring a variety of parameters and mesh levels. To conduct these 2D simulations, we use the University of Chicago rad-hydro code FLASH [23] in 2D spherical geometry. Each mesh cell represents an r-theta (polar angle) wedge, which is revolved around the z-axis (assumed symmetric in the azimuthal angle). As all of our simulations range from 0 to π in theta coordinates, when revolved under the assumption of azimuthal symmetry, they represent the entire spherical capsule. Our main conclusions are as follows.

1. During the RM phase, a latent capsule acceleration is present which acts as a stabilizing force on the perturbations. Therefore at the fuel-ablator interface, no meaningful growth is experienced. While the perturbation is stabilized, there is still vorticity that has been deposited as a result of the shock passage and when the interior ice-gas perturbations are increased, the excess vorticity overcomes the stabilization for the inner parts of the capsule.

2. For the late time deceleration phase, we find only a minor impact on the growth of

the instabilities and the resulting hot spot thermodynamics with the addition of front tracking at the fuel-ablator interface. We do find a significant sensitivity in the instability growth and hot spot thermodynamics to increased vorticity in the problem. This results from larger initial perturbations at the ice-gas interface which lower the overall distribution creating larger low temperature regions and smaller high temperature regions. These effects would have negative consequences with regard to performance of the capsule. This suggests that while the design of NIF capsules is stable and no single effect is responsible for the degradation of performance observed in the experiments, the design is near a performance cliff. The combined effects of multiple instability drivers along with those such as surface defects and ablation instabilities which are not modeled here, can couple to push the capsule past the edge and allow excess mixing of ablator material into the hotspot. This is consistent with the observations of Clark et al. [18] where multiple combined degradation effects are needed to get simulations near agreement with specific experiments.

3. We also find that the use of a buoyancy-drag model to predict 3D instability growth from an input 1D simulation dataset during the RT deceleration stage does a good job of picking up the approximate growth of the instabilities. The model is slightly overpredictive but captures the main trajectory of growth and should be a good guide for analyzing 1D simulations.

6.1 Initial Perturbations

The 2D simulations are similar to the 1D simulations discussed in Chap. 5 but include initial perturbations seeded at both the DT-ablator and DT ice-gas interfaces. The simulations begin at a time equivalent to $\approx$ 14.5ns in the experiment, which is before the shocks have passed over either perturbed interface where we seed the perturbations. Thus simple perturbations of the constant states on either side of a material interface are needed. To

generate the perturbations, we choose random amplitudes (A_i), mode numbers (B_i) and phases (C_i) for spherical harmonics ($Y^0_{B_i}$) with a range of Legendre mode numbers between 8 and 30. Since these are 2D simulations, the perturbations are 1-dimensional and thus a choice of $\phi = 0$ is used for the spherical harmonics. The sum of these randomly generated spherical harmonics are then used to form the base perturbation S_p (See Eq. 6.1).

$$S_p = \sum_i^N A_i Y^0_{B_i}(\theta + C_i, \phi) \tag{6.1}$$

S_p is then scaled so that the root mean square (RMS) of the perturbation has the desired amplitude. To accomplish this, a scaling parameter k, which is the RMS of S_p is computed (Eq. 6.2) and the new scaled amplitudes $a_0 * A_i/k$ are used to produce a series S^*_p (Eq. 6.3) which has the RMS = a_0.

$$k = \sqrt{\frac{1}{\pi}\int_0^\pi S_p^2 d\theta} \tag{6.2}$$

$$S^*_p = a_0 \sum_i^N \frac{A_i}{k} Y^0_{B_i}(\theta + C_i, \phi) \tag{6.3}$$

This approach to seeding of the initial perturbations allows us to study the broadband mix at a lower range of mode numbers, but does not include specific capsule features such as the tent and fill tube which have recently been areas of focus for ICF simulations [18]. We also do not include more specific tuning to the as shot perturbations, as are carried out in Clark et al.'s [18] simulations, which include using diagnostics taken from the actual N120321 capsule right before the experiment was carried out. While this approach certainly leads to improved modeling of a specific shot for comparisons of diagnostics, it is not necessary for the analysis carried out here. In this study we are not focused on obtaining agreement with the experiment, but instead in better understanding how the addition of effects such as front tracking interact with the baseline mixing in simulations that do not include these effects.

6.2 Richtmyer-Meshkov Phase Mixing

The first stage of the simulation that interests us is the time between the first shock passage over the DT-ablator interface and the beginning of the deceleration from the build up of pressure in the core of the compression. We refer to this phase as the Richtmyer-Meshkov (RM) phase, as the growth of instabilities are largely governed by the shock passage across the material interfaces, i.e. an RM unstable configuration. This lasts approximately 7ns in the N120321 experiment, from a physical time of $\approx$ 15.3ns to $\approx$ 22.6ns. There are two shock passages across the interfaces, one from the weaker first shock and the second from the coalesced 2nd, 3rd and 4th shocks, which combine before shocking either of the interfaces.

In this section we show that there is a latent acceleration in the capsule during the RM phase which works to counter instability growth. We investigate across a range of simulations with different configurations (F-BASE vs F-FT) and different initial perturbations (low mode numbers, nominal perturbations and increased initial amplitudes) to understand the competing effects between deposited vorticity by shock passage and the stabilizing acceleration.

In a standard RM simulation, an interface is typically shocked, at which point vorticity is deposited at the interface and the initial perturbations, which are compressed during shock passage begin to grow [71]. At that point, there are typically no other forcings in the simulation, as gravity, which may create the conditions for a more dominant RT instability to take effect, is left out of RM simulations. However, in our ICF simulations, that is not the case. In Fig 6.1 left, we plot the total pressure $P_{tot} = P_{ion} + P_{ele} + P_{rad}$ as a function of time at the Lagrangian boundary point used to drive our implosion. As discussed in Sec. 3.2.1, this data has been exported from a 1D HYDRA run taken at a fixed Lagrangian cell, representing approximately the edge of the first layer of ablator material. For most of the time covered by the RM phase, the pressure continues to rise at the edge of the simulation domain, except for a few isolated dips caused by shock waves and reflected waves crossing over it. This makes sense in the context of low foot ICF experiments where the laser driver is

used to produce multiple shock waves of increasing strength. The temperature and pressure in the hohlraum continue to rise through the RM phase of the implosion [29]. In addition, N120321 is classified as a "o-coast" shot [17], which implies that it is designed to switch straight from the laser driven acceleration phase to the deceleration phase. The deceleration phase is responsible for the strong increase in pressures at the boundary at late time, which is coming from the outward moving stagnation shock as opposed to inward moving waves during the RM phase. The lack of a coasting period was designed to limit the instabilities and a different shot which did have a coasting phase, may have a different pressure profile at the boundary we have used. The impact of this increasing pressure at the boundary is that a small but latent inward acceleration in the capsule is generated. The acceleration profile for the boundary point is shown in the right frame of Fig 6.1. This acceleration is acting from the heavier ablator material to the lighter DT fuel and thus represents an RT stable configuration. This has a stabilizing effect on the interface and its perturbations, which helps to limit and damp out any growth that would of been induced by a standard RM configuration.

To study the impact of this stabilizing effect we begin by analyzing a 2D F-BASE (no Front Tracking or mass diffusion models coupled in) simulation with perturbations initialized at both the ice-gas and fuel-ablator interfaces. The RMS for these perturbations are both chosen to be 1μm. A perturbation of 1μm at the ice-gas interface is consistent with the expected size of the perturbations in the ICF experiment for N120321 [16]. For the fuel-ablator interface, a nominal perturbation is $\approx$ 200nm and so this represents a slightly larger perturbation than may be found in the experiment for this interface. We will refer to the 1μm perturbation at both interfaces as our nominal perturbation going forward. The resolution for this simulation and the others discussed here are 2000×100, which represents a grid cell size of $\approx 0.5\mu$m for the radial direction. In the theta direction, 100 cells provides a resolution of approximately 7 cells for the smallest wave lengths in the initial perturbation and approximately 25 cells for the largest wavelengths. In lieu of higher mesh resolution

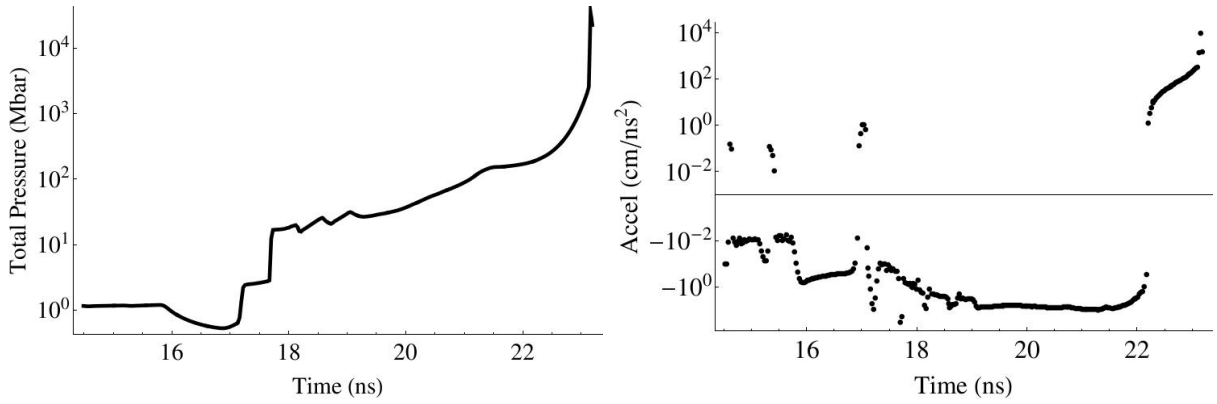

Figure 6.1: Pressures (left) and accelerations (right) at the time dependent boundary point used to drive our FLASH simulations. The edge of the simulation domain is a Lagrangian tracked point in the middle of the CH shell. Pressures slowly increase for the majority of the simulation causing a latent inward acceleration during the RM phase which produces a stabilizing effect on the instability growth during this time.

simulations, we will use the comparisons to the front tracked solution as a measure of determining if the solution is converged. The front tracked solution had around a 10% error in the 1D simulation study over the area of interest, which we feel should be sufficient to study the hot spot thermodynamics and ablator mix.

In Figs. 6.2 and 6.3 we plot a series of four plots showing the progression of the growth of the instabilities during the RM phase. The plots are presented in the $r-\theta$ plane to allow for magnification of the perturbations which are not easily observed in the cartesian plane. In Fig. 6.2 top, the initial perturbations in black contour lines are overlayed on the density grid. Two distinct perturbations are present and the initial location of the first shock can be observed at approximately 955μm, where the plot switches to the dark red color. In Fig. 6.2 bottom, the simulation is at $\approx$ 17.5ns, midway between the passage of the first shock and the second shock across the fuel-ablator boundary. The initial perturbation has been compressed by the first shock and is not growing as one would of expected for an RM instability. This is due to the stabilizing effect of the acceleration.

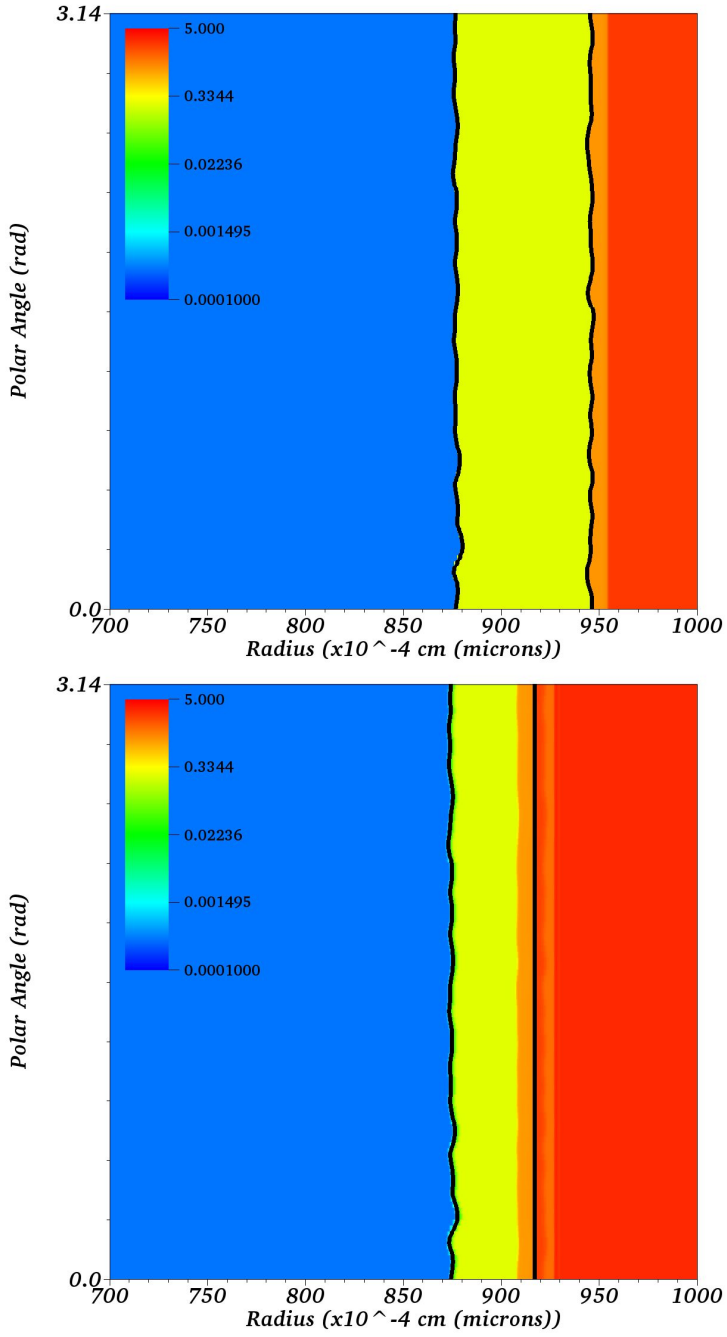

Figure 6.2: Contour plots of density in $r - \theta$ space, with black contour lines representing the ice-gas and fuel-ablator interfaces. Top: Initial conditions for the F-BASE nominal perturbation. Bottom: Midway between the first and second shocks interacting with the outer interface and before the first shock has interacted with the inner ice-gas interface. A post-shock stabilization of the perturbation due to a latent inward acceleration of the capsule has diminished the perturbation at the ice-gas interface.

In Fig. 6.3 top, we have progressed to $\approx$ 21ns, about 2ns after both interfaces have been shocked by the coalesced final shock wave. The fuel-ablator interface still has no instability present as the stabilizing acceleration has been the dominant driver on that interface. The ice-gas interface on the other hand shows a perturbation similar to its initial state. This is a function of multiple dynamics occurring in the simulation. The first is that the inner interface is closer to the inward moving shock, which when it crossed through the interface refracted and is now distorted. The reverberation of the transverse waves between the shock and inner contact [6] are adding vorticity to the ice-gas interface which helps strengthen the driver for the perturbation growth. The ice-gas interface acts as a stop gap, weakening transverse waves that try to reach the fuel-ablator interface and thus the overall vorticity is larger at this inner interface. Since there is vorticity present at these interfaces, deposited when the shock waves interacted with them, in the absence of a stabilizing mechanism, there would be sufficient mechanisms to allow the perturbations to grow. Thus a balancing effect between these two forces results in seemingly random ripples which come and go on the interfaces. Thus at this particular time the interface happens to be at a point where perturbations have developed slightly. At later frames this will subside and then grow again, in an almost random fashion. Finally in Fig. 6.3 bottom, we are at the approximate end of the RM phase, where maximum implosion velocity is reached. At this stage in the implosion the capsule has about a factor of 6 compression and the perturbations at the fuel-ablator interface are approximately of the same order as the initial perturbation. The ice-gas interface has had its perturbations suppressed again by the lingering acceleration. From this 2D F-BASE simulation there appears to be only a minor change in the initial perturbation amplitudes over the range of mode numbers and for the broadband mix studied here during the RM phase. This suggests that no meaningful broadband mix or growth occurs during this phase and that the size of the initial perturbations at the beginning of the RT phase is comparable to those that are initially seeded.

We now examine the RM phase of the same simulation using a 2D F-FT configuration,

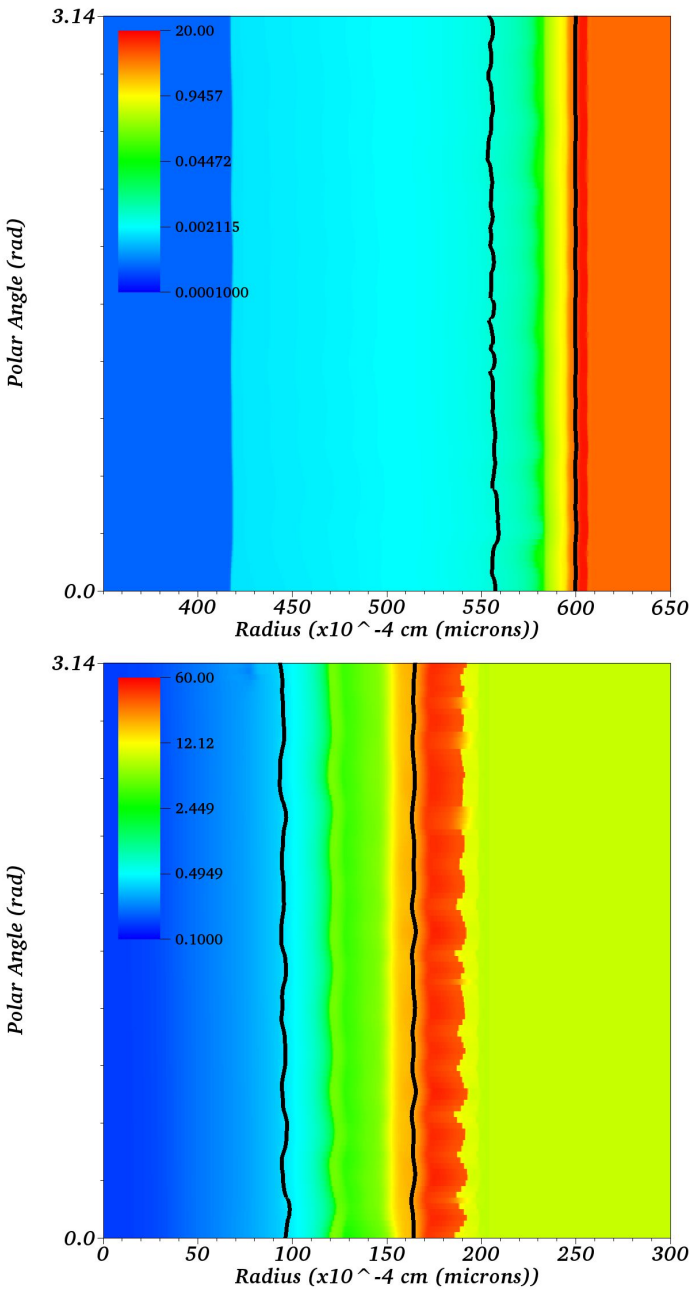

Figure 6.3: More contour plots of density for the F-BASE nominal perturbation simulation. Top: $\approx$ 2ns after the final shock has interacted with both interfaces. The outer DT/CH interface (right contour line) is still stabilized and the inner ice-gas interface (left contour line) is experiencing random ripple growth, due to the competition between deposited vorticity and the stabilization effect. Bottom: End of RM phase, approximately where the capsule has achieved maximum implosion velocity. Both interfaces have experienced minimal instability growth due to the RM phase stabilizing latent acceleration.

which adds only front tracking to the model. In Fig. 6.4 we again overlay the interfaces in black on the density grid in $r - \theta$ space. This frame is taken near maximum implosion velocity at the end of the RM phase. It is directly comparable to Fig. 6.3 bottom. We see hardly any difference in the perturbation growth between both the F-FT and F-BASE simulations. The suppression of the instability growth during the RM phase as a result of the lingering acceleration does not interact in any meaningfully different way with the tracked front simulation.

To complete this analysis, we show in Fig. 6.5 four more simulations at the end of the RM phase. The top row represents simulations using the F-BASE configuration and the bottom row the same simulation using the F-FT configuration. The left column are low mode simulations, where only mode numbers 6-12 were seeded at initialization with as manufactured amplitudes. The right column are simulations where the initial perturbation was increased by $5\times$ at the DT ice-gas interface (referred to as "strong" simulations). The low mode simulations tell largely the same story as the nominal perturbation simulations from above. The strong simulations however, show some significant perturbations at the end of the RM phase. We first focus on the bottom left corner, the F-FT strong configuration. In this simulation a slightly amplified signal is present at the front tracked fuel-ablator interface, but for the most part this is not significantly different than the nominal perturbation from Fig. 6.4. The inner ice-gas interface however, which is where the initial perturbations were amplified, shows quite a bit of growth as a result of the RM phase. The top left corner shows the same strong simulation this time using the F-BASE configuration, without the use of front tracking. The ice-gas interface is mostly similar to the F-FT simulation, as neither has a tracked front at this contact so the dynamics are largely the same. For the outer fuel-ablator boundary there is a meaningful perturbation, which is different from the largely stabilized instability of the F-FT simulation.

To account for this we focus on the dynamics generated by the stronger initial perturbation at the ice-gas interface. A stronger initial perturbation results in additional vorticity

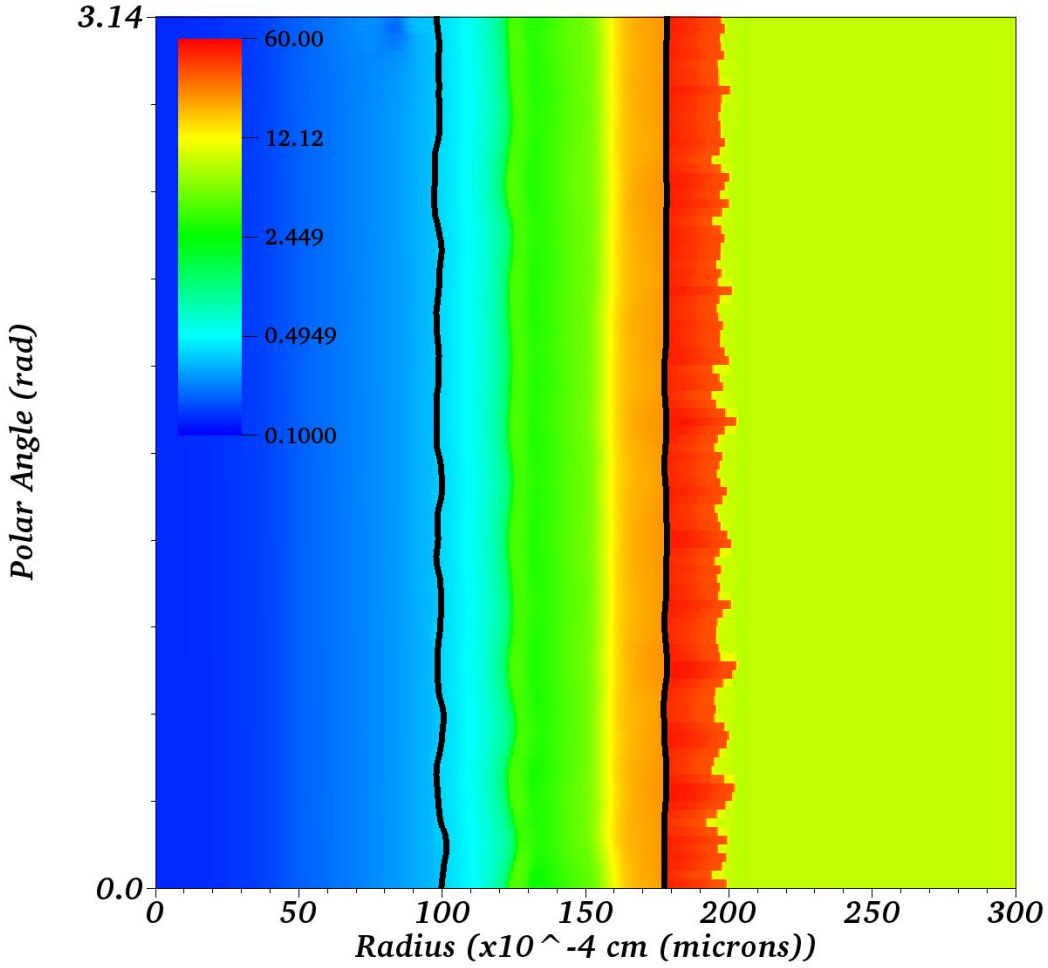

Figure 6.4: Contour plot of the F-FT nominal perturbation simulation at the end of the RM phase. This figure can be compared directly to the companion F-BASE simulation in Fig. 6.3 bottom. No meaningful difference in the perturbations is apparent at the end of the stabilization phase. This suggests that the addition of front tracking at the fuel-ablator interface has little to no effect on the perturbation growth of the DT/CH interface and no coupling effect to the untraced ice/gas interface, since it is dominated by a stabilizing RM phase latent acceleration profile in the capsule.

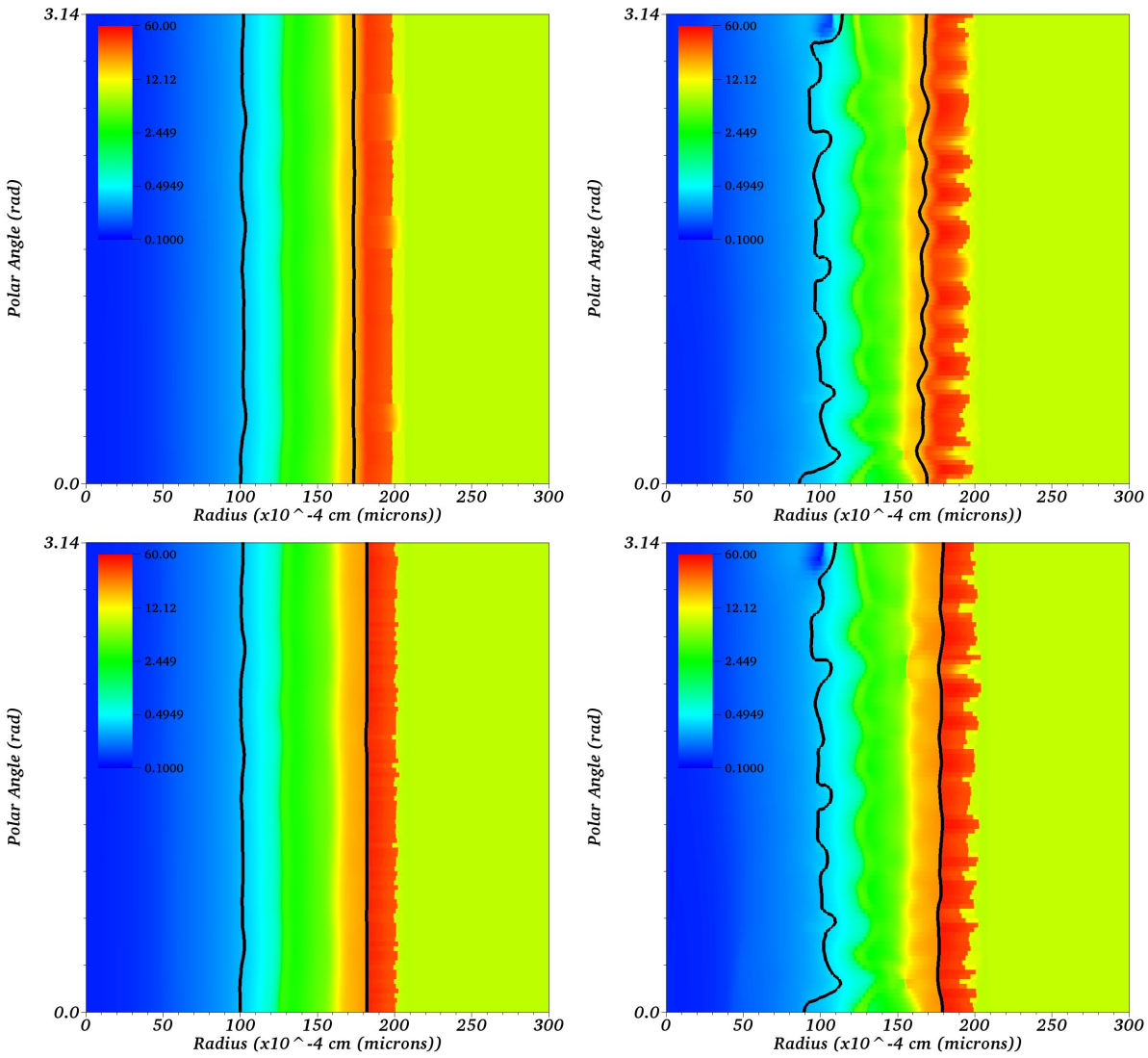

Figure 6.5: Contour plots at the end of the RM phase. The top row represents F-BASE configurations and the bottom row F-FT configurations. The left column are low mode simulations, only initialized with mode numbers 6-12. The right column are strong perturbations, where the ice-gas interface initial amplitude is 5 $\times$ the nominal amplitude. For the low mode simulations (left column) the interfaces are completely stabilized and the impact of FT has no effect. For the strong simulations (right column) notable growth has occurred at the interior ice-gas interface. The stronger initial perturbation adds more vorticity to the dynamics allowing the inner interface to overcome the stabilizing effect. The top right F-BASE simulation also shows slightly amplified mixing relative to the companion F-FT simulation in the bottom right.

deposited at the interface and generated by the ricocheting transverse waves. This results in about a factor of two increase in the vorticity present for the strong simulation relative to the nominal initial perturbation. For the ice-gas interface, this vorticity is enough to overcome the stabilizing effect especially towards the latter end of the RM phase, when the stabilizing acceleration for this interior interface has largely dissipated. The stronger vorticity from the shock contact interaction continues to be carried back towards the fuel-ablator interface through reflected waves. This interaction between the two interfaces provides enough rotational energy to overcome the stabilization effects at the outer interface as well, allowing some increased instability growth at the more crucial fuel-ablator contact. For the corresponding F-FT strong simulation, we argue that the reason the instability growth does not show up as significantly at the fuel-ablator interface is due to the same reasons front tracking has been able to perform better relative to experimental growth rates in past validation studies of RT growth [27]. The growth of these instabilities is driven by the density gradients at the interface. Allowing for numerical diffusion, the density gradients smooth out and the local Atwood number decreases, resulting in reduced growth [24]. The stabilization effect is governed by the same density gradient. Since the front tracking maintains a sharp gradient at the interface, its local Atwood number is larger and thus the stabilization effect is amplified, limiting the amount of instability growth the added vorticity can produce.

Overall, the RM phase instability at the tracked front fuel-ablator interface is largely stabilized by the latent acceleration in the capsule. Additional simulations not shown here were run with different random sets of perturbations, stronger initial perturbations at both interfaces and different sets of initial and boundary conditions, representing Lagrangian points at different locations in the ablator region. Over this parameter study, there was no significant difference to those simulations presented here, where the only parameter that seems to have an impact on instability growth is the initial perturbation amplitude for the ice-gas interface. In typical RT and RM simulations where front tracking has shown a meaningful impact on instability growth, the impact has been observed relative to the

growth rates and since we have minimal growth here, we would expect to see no meaningful difference between the tracked and untracked simulations.

6.3 Deceleration Phase Rayleigh-Taylor Phase Mixing

The primary instability growth occurs during the deceleration phase where a stagnation wave works its way against the compression of the capsule. The deceleration works to push the light hot DT core into the cold DT shell, causing an RT unstable configuration. This phase lasts from the time the capsule experiences maximum implosion velocity through bang time, when the maximum neutron production rate is achieved. For N120321, this lasts around 500 picoseconds.

6.3.1 Numerical Concentration Diffusion

We begin our analysis by examining the impact the numerical diffusion at the DT fuel-ablator interface has upon the late stage instability growth. The simulations discussed here are the same 2000×100 simulations discussed in Sec. 6.2. In Fig. 6.6 we plot the normalized carbon fractions for 4 simulations at bang time. The top row consists of F-BASE simulations with both the nominal perturbation (top left) and strong perturbation (top right). The bottom row is the same simulation using the F-FT configuration. We also show two temperature contours, representing the boundary of the 2 keV (black) and 5 keV (gray) regions at bang time. It is immediately apparent that a major qualitative difference exists between the tracked and untracked simulations. As was the case in the 1D simulations in Sec. 5.3, as a key feature of the front tracking algorithm, numerical diffusion is prevented at a tracked interface. The resulting diffusion in the top frames is purely the result of numerical diffusion at this coarsest grid level of $\approx 0.5\mu$m as these simulations are run without the coupled mass diffusion model. Comparing the top left (nominal) to the top right (strong), we see that the enhanced instability growth at the interior regions

of the capsule in the right frame has resulted in the carbon concentration being pulled further inward. This extra instability growth has also lowered the temperature in the inner regions of the core, completely eliminating the 5 keV region. Some impact from the front tracking can be observed on the temperature contours comparing the top row to the bottom. However, this change, resulting in larger regions of higher temperature regions and slightly more symmetric regions is minor when compared to the more drastic impact of the larger perturbations (comparing the left column to the right).

To further examine the penetration of the ablator material from the coupling of instability growth and numerical diffusion, we plot in Fig. 6.7 the contour position of the ablator material (using carbon as a surrogate) for the F-FT simulation at the 5% and 25% contour levels. Bang time is between 23.10 - 23.12ns for all the simulations considered here. The left frame shows the locations of the contours for the nominal perturbations and the right frame for the strong perturbation initialization. Up until just before bang time, the nominal and strong perturbations show little difference in the distance of the numerical diffusion penetration. However, in the final 100 picoseconds before bangtime, the excess perturbation growth in the strong configuration begins to pull the ablator material further inward.

To quantify the penetration observed at bangtime, in Table 6.1 we calculate the radius of the 5%, 25% and FT contour (where FT represents the companion F-FT simulation which has no numerical diffusion) and the resulting penetration fraction, defined as the ratio of the difference between the contour and the front tracking contour with respect to the front tracking contour. The 5% contour is strongly impacted by the instabilities, being pulled upwards of 15% further into the core than the 1D profile for the numerical diffusion. In the strong perturbation, this effect is amplified and the 25% contour also sees a strong effect, being pulled nearly 20% of the way into the core from the front tracked position. As a reference point, we note that the hot spot boundary, defined as the 2 keV contour from the associated 1D simulation is at $\approx 28\mu$m, resulting in the 5% contour from the strong perturbation being pulled into the hot spot region.

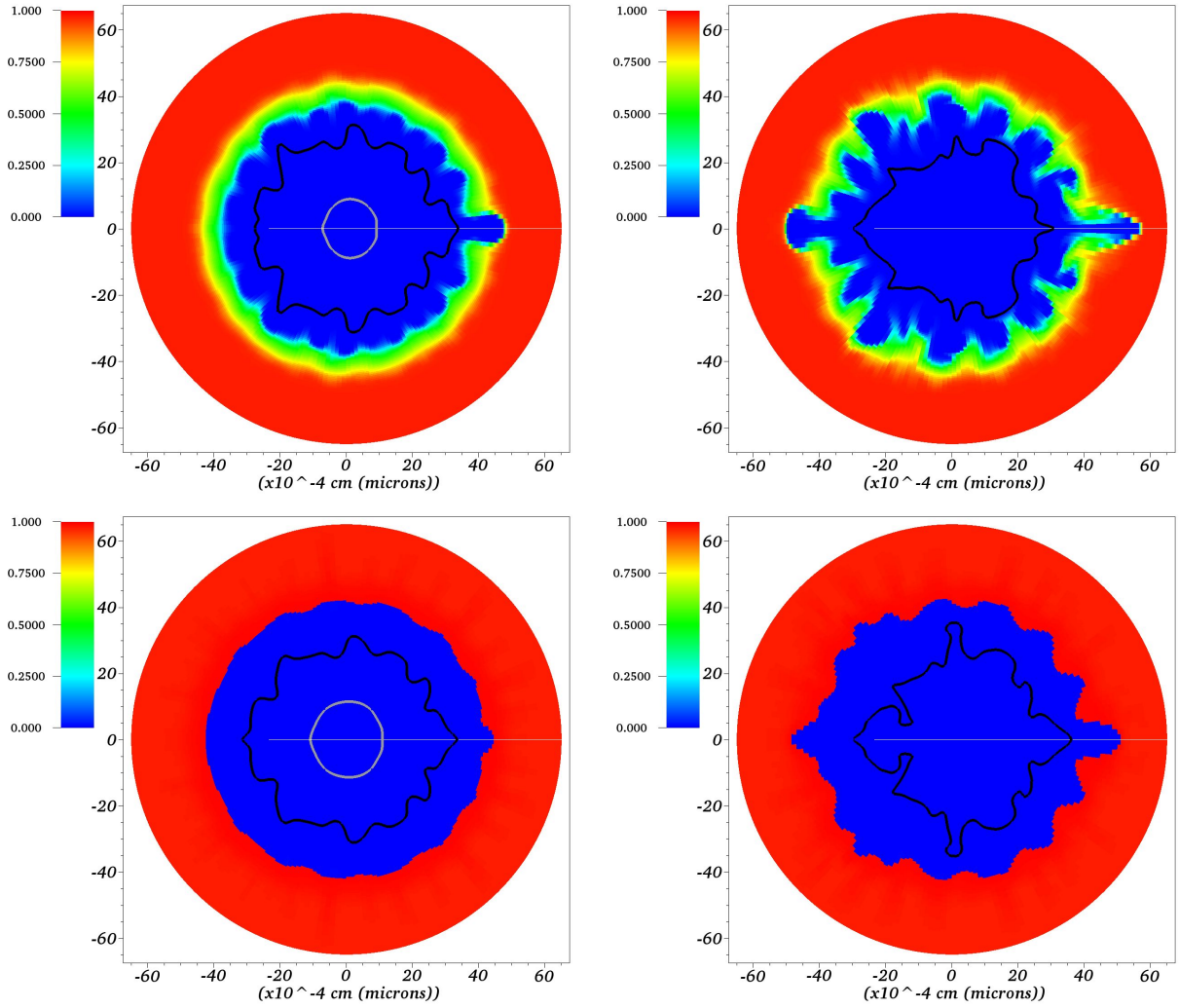

Figure 6.6: Normalized carbon concentrations for the F-BASE nominal (top left), F-BASE strong (top right), F-FT nominal (bottom left) and F-FT strong (bottom right) simulations. Front tracking completely removes this numerical artifact while the F-BASE simulations are susceptible to the strong RT growth amplifying the penetration distance of the numerical diffusion. The 2 keV ion temperature (black) and 5 keV (gray) contours are also shown. The stronger initial perturbation (right) completely removes the high temperature 5 keV region at bangtime.

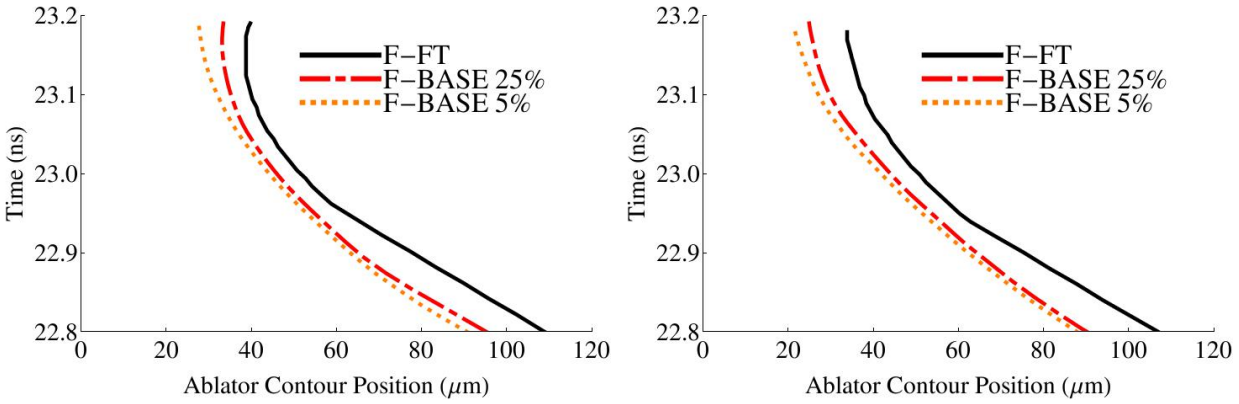

Figure 6.7: Time dependence of the furthest penetration for the 5%, 25% and F-FT contour of ablator material in the last 300 picoseconds of the implosion. Bang time is between 23.10ns and 23.12ns for all simulations. Left: Nominal perturbation. Right: Strong perturbation. The stronger growth in the strong perturbation case causes a drastic increase of the contour positions in the last 100 picoseconds or so before bangtime. Only the F-FT solution, which completely removes this numerical artifact is physically accurate.

Table 6.1: Contour radius and penetration fraction for the ablator material resulting from numerical diffusion in the coarse F-BASE simulations compared to the position of the fuel-ablator interface in the associated front tracked simulation which has no numerical diffusion. The strong instabilities during the deceleration phase amplify the 1D numerical diffusion effects to pull the ablator material further into the inner regions of the capsule, crossing the $\approx 28\mu$m hot spot radius from the associated 1D simulation.

	Nominal Perturbation		Strong Perturbation	
Contour	Contour Radius	Penetration Fraction	Contour Radius	Penetration Fraction
F-BASE 5%	31.0μm	21.03%	25.9μm	28.68%
F-BASE 25%	34.6μm	12.02%	28.6μm	21.36%
F-FT	39.3μm	-	36.4μm	-

As we observed in Sec. 5.4, when numerical diffusion is prevented through the use of front tracking and replaced with a physical mass diffusion model, no meaningful diffusion of the ablator material is observed. Thus the diffusion effect is purely a numerical artifact. While increased resolution in the F-BASE simulations would certainly mitigate this effect somewhat, the strength of the RT instabilities can still amplify even mostly suppressed diffusion. Thus, there is a clear need for mitigation strategies for numerical diffusion in Eulerian simulations. This is an undesired effect that has the potential to contaminate the solution. Front tracking is a straightforward way to remove this diffusion completely, whereas AMR and interface reconstruction methods may still allow some numerical diffusion, which may get caught up in these instability cliffs in the regions just near the fuel-ablator boundary. It can be inferred that with stronger instabilities, which may come from unmodeled physical processes here such as the ablation front instabilities or individual surface defects, that the only true way to prevent the numerically diffused ablator material from being amplified is to completely remove it with the use of a front tracking strategy.

6.3.2 Hot Spot Thermodynamics

To complete the study of the RT deceleration phase we focus on the two main inputs to neutron yield calculations, the temperature and density at bang time. We do not calculate yields directly as FLASH does not have Monte Carlo neutron transport capabilities or other sophisticated burn models. Instead we focus on the trends observed across our parameter study of simulations, identifying the impact of front tracking and stronger initial perturbations.

In Fig 6.8 we display a pseudocolor plot of density with contour lines representing increasing temperatures, from 1 keV stepping to 5 keV as the solid contour lines move inward. The top half are the 2D simulations which are compared with the 1D simulations in the bottom half of each figure. The 2 keV contour is representative of the edge of the hotspot and the 5 keV temperature shows the size of the hot core region in the 1D simulation. The

top frame represents the F-BASE simulation and the bottom frame the companion F-FT simulations where both of these are using the nominal initialization. Overall, we notice a slightly less perturbed capsule and as a result, slightly larger regions of higher temperature in the F-FT simulation. The instability growth at the fuel-ablator interface is negligible for these simulations and thus no real impact for front tracking is observed there. It is not clear if the slight differences between front tracking and the untracked version are solely the impact of numerical diffusion present in the untracked F-BASE simulation or additional effects that may be masked by this phenomenon. Further studies with additional refinement would be needed to examine that in more detail. Overall, it appears that front tracking has a minor impact on the bangtime thermodynamics when used at the fuel-ablator boundary. This may simply be a surrogate for a converged solution, as we observed in Sec. 5.2 and note that these regions are also larger in the associated F-FT 1D simulation. We conclude that front tracking's main contribution is with regard to the removal of numerical diffusion at the fuel-ablator interface. These simulations show no meaningful impact on the thermodynamics from the fuel-ablator mix, and thus emphasize that to allow the amount of ablator material that is present in the experiments to make its way into the hotspot, it would appear to be from a here unmodeled cause. We point to ablation front instabilities [60] as a leading hypothesis to explain this phenomenon.

In Fig 6.9 we plot the same set for the strong initial perturbations at the DT ice-gas interface. We observe a strong effect on the final configuration of the capsule with these initial conditions. The more deformed hot spot has drastically reduced the regions of highest temperature (completely removing the 5 keV contours) and created a much more asymmetric hotspot which are both negative indicators with respect to overall neutron yield. Front tracking again has a minor impact on the thermodynamics, with the regions of high temperature increasing slightly and the density profiles mostly unchanged. Again, we believe this is a surrogate for a converged solution. The impact of the numerical diffusion may again be responsible for the slightly larger perturbations in the non-front tracked solution, but

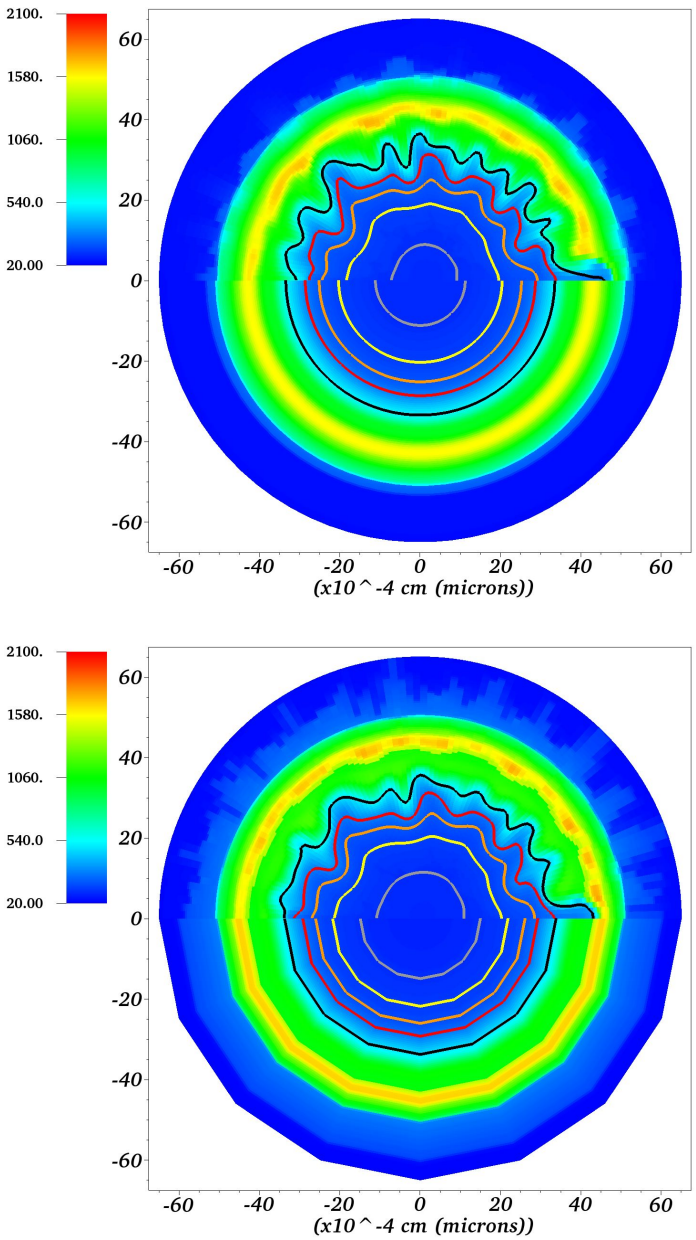

Figure 6.8: Density profile (colorbar) and temperature contours (1 - 5 keV, solid lines as you move inward) for the bangtime configurations of the nominal perturbation capsules. Top half are the 2D simulations compared with the 1D simulations in the bottom half of each figure. Structurally, the F-BASE (top) and F-FT (bottom) simulations largely agree with regard to these important observables. The tracking at the outer fuel-ablator interface, demarcated by the higher density (red) regions outside of the mixing region, has a small impact on the thermodynamics, most likely representing a closer to converged solution.

more refined simulations using the F-BASE configuration would be needed to definitively answer that. The main takeaway from the late time is that there is indeed a strong sensitivity in the thermodynamics to increased rotational energy in the configuration. Here that was accomplished with increased perturbations at the ice-gas interface, but other mechanisms such as 3D effects and ablation instabilities could be a surrogate for that as well. As the mixing is increased, it is more likely that small perturbations at the fuel-ablator interface get pulled into the inner regions of the capsule and degrade the neutron yield as observed in the experiments.

6.4 Buoyancy-Drag Model

In this section we explore the use of the well known buoyancy-drag model [10] for RT and RM instability growth and apply it to the late time deceleration phase. As inputs, the model requires a 1D profile, taken from a coupling into our 1D simulations. As output, the model produces a predicted growth of the spikes based on the 1D flow conditions. We compare this model to our 2D simulations and examine the efficacy of the model for the ICF regime.

6.4.1 Model Description

The buoyancy-drag model is an Ordinary Differential Equation (ODE) developed as a phenomenological model to represent the evolution of the leading edges of the mixing fronts in both RM and RT instabilities. It has a long history of validation against RM and RT experiments [54] and is commonly used as a comparison for RM and RT numerical simulations [10]. There are multiple forms of the model [57, 9] and in our analysis we will use the one proposed by Cheng et al. [10], presented in Eq. 6.4.

$$\frac{dV_i}{dt} = (-1)^i A(t) g(t) - (-1)^i C_i \frac{1-(-1)^i A(t)}{2} \frac{V_i^2}{|Z_i|}, \qquad i = 1, 2 \tag{6.4}$$

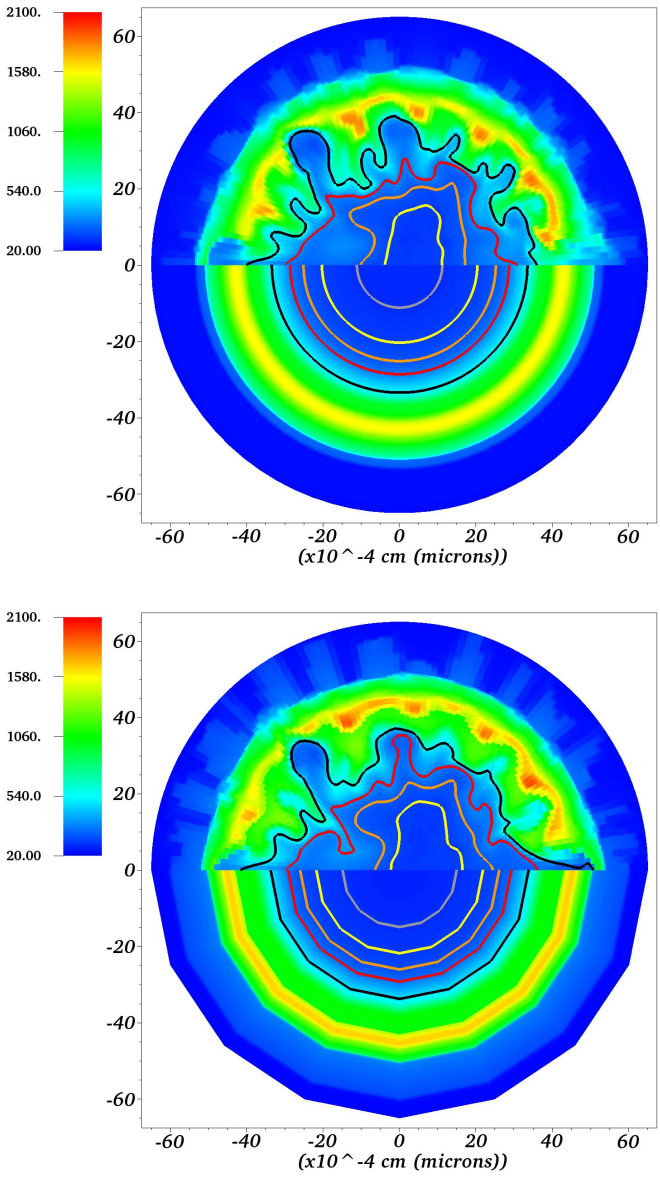

Figure 6.9: Density profile (colorbar) and temperature contours (1 - 5 keV, solid lines as you move inward) for the bang time configurations of the strong perturbation capsules. Top half are the 2D simulations compared with 1D simulations in the bottom half of each figure. Top: F-BASE, Bottom: F-FT. Stronger initial perturbations have resulted in enhanced mixing, deforming the hotspot and reducing regions of hot temperature (eliminating the 5 keV region) relative to the nominal perturbation (Fig. 6.8). Some qualitative differences exist in the hot spot shape between the top and bottom, but overall these effects are dwarfed relative to the change between the nominal perturbation (Fig. 6.8) and the strong perturbation here.

Here V_i is the velocity of the i^{th} edge of the mixing zone, $A(t) = \frac{\rho_i - \rho_i'}{\rho_i + \rho_i'}$ is the Atwood number, $g(t)$ is the acceleration, C_i is the drag coefficient and Z_i is the position of the i^{th} edge. C_i is set as follows from [9] with $k = 1$ and α_s set from α_b using the relations in Cheng et al. [9].

$$C_i = \frac{\frac{1}{\alpha_i} - 2 * (1 - (-1)^i A(t))}{2 * (1 - (-1)^i A(t))} \tag{6.5}$$

To use the buoyancy-drag model to predict the growth of the instability, we start with a 1D or pseudo-1D simulation. We couple the buoyancy-drag model into the simulation and have three free parameters which need to be set, a_0, v_0 and α_b, the initial amplitude, velocity of the perturbation and bubble growth rate, respectively. Using the Lagrangian position of the edge of the perturbation as predicted by the buoyancy-drag model at any given step, we calculate the local fluid acceleration from a time-derivative of the velocity at the Lagrangian point. To define the Atwood number, we calculate the minimum density and maximum density over a bounding box of computational cells covered by the perturbation at that given time with the addition of a 1μm buffer to allow for small random sensitivities in the simulation to dominate the effects. As one would expect and as is clear from Eq. 6.4, the buoyancy term $A(t)g(t)$ typically acts to increase the velocity of the perturbation and thus has the same sign as the penetration growth for that material. For simplicity, we then define $A(t) = \frac{\rho_H - \rho_L}{\rho_H + \rho_L}$ where ρ_H is the maximum density and ρ_L is the minimum density over the region. Our $g(t)$ in Eq. 6.4 is then set to the negative of the local acceleration, to ensure that the buoyancy term has the correct sign. This is consistent with Eq. 6.4, where $A(t)$ changes sign depending on which material is being considered. Our goal with the buoyancy-drag analysis is to capture the perturbation growth of the ablator material spike into the hot spot region.

6.4.2 RT Deceleration Phase

Using the buoyancy-drag model we predict spike penetration into the hot spot during the deceleration phase. Using the F-BASE simulation, we start tracking the Lagrangian point which represents the center of the mixing zone at 22.60ns, approximately the beginning of the deceleration phase. We use a starting amplitude of 1μm, based on the analysis from Sec. 6.2 that suggests the RM instability experiences a stabilizing RT acceleration which prevents the initial instabilities from growing. For the initial velocity, we arbitrarily choose $1.e-8$ cm/ns, which should have only a minor impact on the early time of the growth as the RT instability quickly becomes independent of its initial conditions [10].

In Fig. 6.10 we plot 3 curves, starting at three different locations in the capsule. The outermost curve (red, dot-dash) was initiated at a point representing the Lagrangian location of the 50% contour of the CH boundary at $t = 22.60$ in the 1D F-BASE configuration. The middle curve (blue, solid) was initiated at a mid point in the cold shell, which is designed to capture the strong instability growth observed in Fig. 6.8, which begins at the thermal gradient that develops at the edge of the hotspot, midway between the ice-gas and fuel-ablator interfaces. The innermost curve (gray, dotted) was initialized at the 50% concentration level representing the boundary between the ice and the gas. The dotted black line represents the edge of the 2 keV temperature contour at bangtime, used to represent the edge of the hot spot. The growth of the ablator material does not reach the edge of the hotspot, consistent with that predicted by the 2D simulations. The deformation of the hotspot from the 1D symmetry is a result of the growth of the instability at the thermal gradient, represented roughly by the middle curve. This growth causes spikes of colder material to push into the hot spot regions, causing asymmetries in the containment which degrades the capsule.

To examine the accuracy of the buoyancy-drag model we compare the model's spike penetration to a companion 2D simulation where we post-process the data to obtain the location of the spike tip. For the simulations, we compared both the F-BASE nominal perturbation

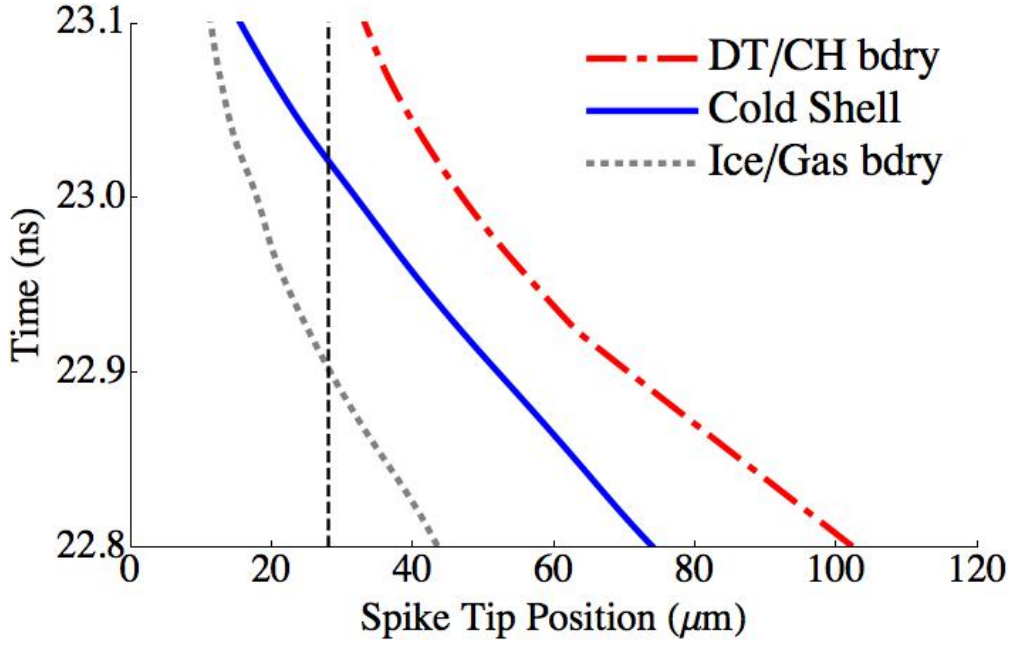

Figure 6.10: Buoyancy-Drag calculations of the RT deceleration phase. The outermost curve (red, dot-dash) begins at the fuel-ablator interface, the middle curve (blue, solid) begins at a point which is the main Lagrangian point for the instability growth observed in the 2D simulations and the inner curve (gray, dotted) begins at the ice-gas interface. The black dashed line represents the edge of the hotspot as determined by the 2 keV contour at bangtime. The most noticable growth occurs for the middle curve, causing spikes developing at this temperature gradient to penetrate inwards and cause the deformation of the hot spot from symmetry observed in the Fig. 6.8 and 6.9.

and the F-BASE strong perturbation to the buoyancy-drag model. In Fig. 6.11 we compare the F-BASE strong perturbation to the buoyancy-drag prediction for the DT/CH boundary. The 50% contour is calculated at each datapoint in the simulation and plotted against the buoyancy-drag mix model. Early time disagreement is due to the small growth encountered in the F-BASE strong perturbation during the RM phase. The nominal perturbation has a similar growth shifted slightly further out, to account for the stronger stabilizing effect in the nominal simulations. The 2D simulations agree relatively well with the buoyancy-drag prediction. During the final 100 ps or so before bangtime, the buoyancy-drag model over predicts the growth by about $5-10\%$ allowing it to catch up to the F-BASE strong perturbation. Overall the model does a good job of capturing the growth of the instability. A few contributing factors to the slight disagreements observed in the model can be a combination of the 2D vs 3D instability growth effects and the spherical geometry vs planar assumptions of the model. The 2D simulations should result in an overprediction by the 3D growth model and the spherical geometry should result in an underprediction, so to resolve these competing effects a more thorough study would be needed to fully explore potential improvements to the model. In its current form, the buoyancy-drag model described here should be a good predictor of instability growth in 3D simulations and the experiments.

The main concern for capsule performance is related to the ablator material flowing into the hotspot. While this does not occur from the nominal design specifications, since a stronger instability is present as we move inward from the initial fuel-ablator interface, any perturbation of the 1D location of that interface is at risk for getting caught up in the strong thermal instability and being carried into the hotspot. We use the buoyancy-drag model to test a range of Lagrangian points inside the cold shell to determine how large of a perturbation would be necessary to achieve a CH spike that would penetrate into the hotspot. In Fig. 6.12 we plot the same 1D position for the DT/CH boundary along with two additional Lagrangian points, one that represents an 11μm perturbation (blue, solid) which just reaches the hot spot boundary at bang time and a 16μm perturbation from the DT/CH

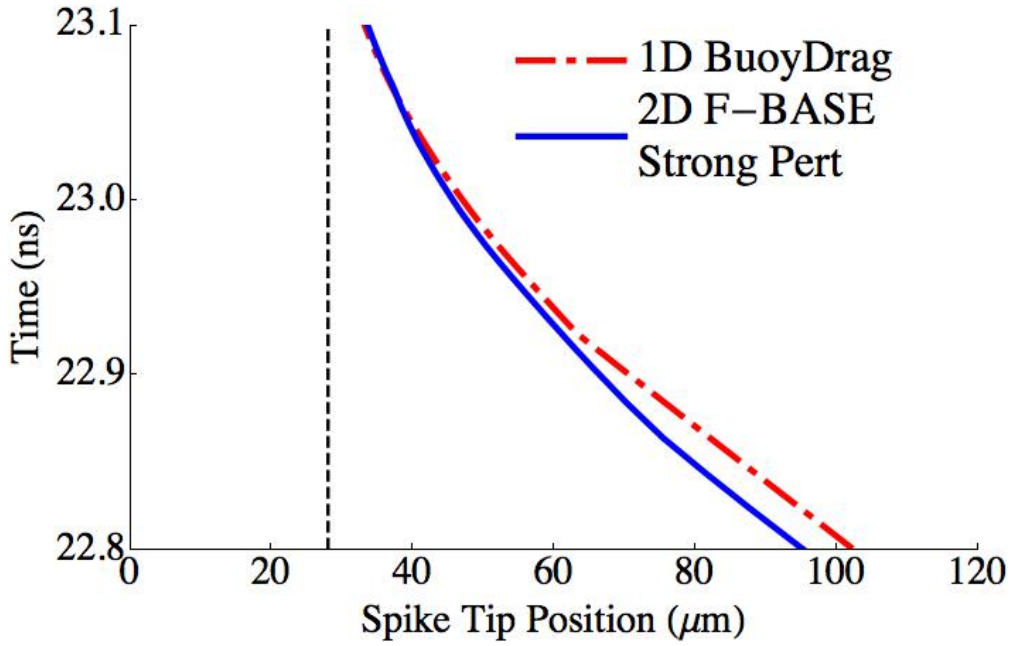

Figure 6.11: Buoyancy-Drag calculations of the RT deceleration phase (red, dot-dash) plotted against the 2D FBASE strong simulations' (blue, solid) observed growth of the fuel-ablator instability. The black dashed line represents the edge of the hotspot as determined by the 2 keV contour at bangtime. Relatively good agreement is observed with the strong simulation over-predicting the early time growth due to lingering effects from the RM phase and the buoyancy-drag model slightly over-predicting the late time growth. Overall the buoyancy-drag model appears to predict the instability growth well.

boundary, which eclipses the hot spot boundary. As we observed a large stabilization of the interface during the RM phase, the simulations don't observe a large enough perturbation for this to occur. Additional effects that are unmodeled here, such as the ablation instabilities which carry through to the RM phase or surface defects which can cause jets of ablator material to propagate inward may be large enough to reach this size perturbation and deposit ablator material into the hot spot. Based on this, we argue that the NIF capsules sit on a performance cliff where small perturbations in the design specifications which can generate additional instability growth are at risk of having a coupled effect which causes a small perturbation of ablator material, which gets caught up in the stronger instability in the inner regions of the cold DT shell. This can then result in ablator material ending up in the hotspot, which is one of the key mechanism believed to be responsible for the lower performance in the NIC low foot capsules [43].

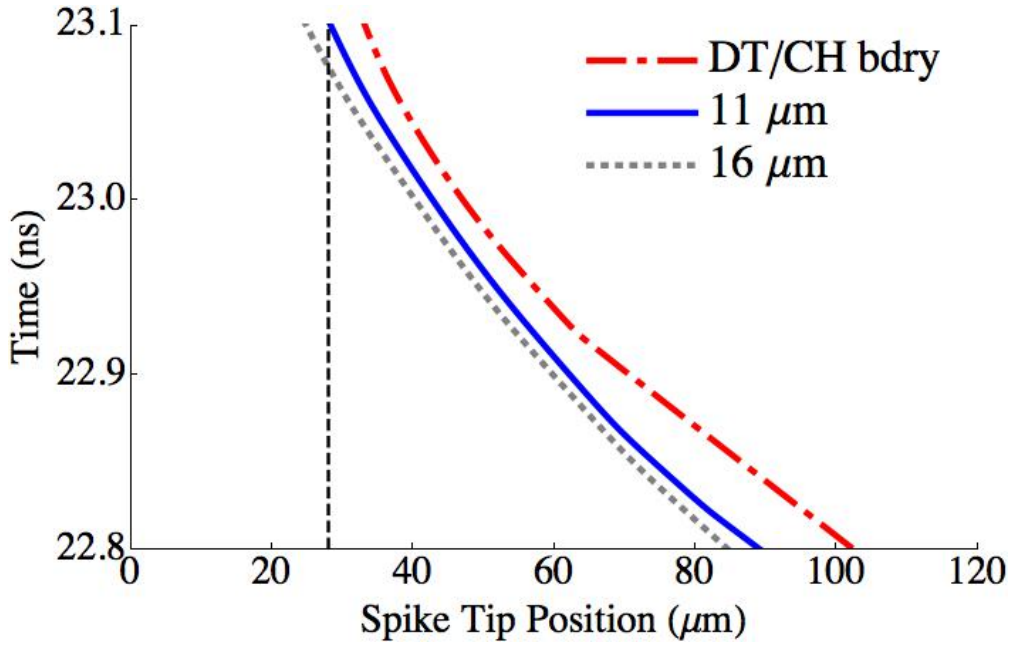

Figure 6.12: Buoyancy-Drag calculations of the RT deceleration phase. The outermost curve (red, dot-dash) begins at the fuel-ablator interface, the middle curve (blue, solid) begins at a point 11μm interior to the fuel-ablator interface and the inner curve (gray, dotted) begins at a point 16μm interior. The middle curve starts far enough inward that the stronger instability would pull ablator material from that position to approximately the hot spot boundary, represented by the black dashed line. With the 16μm perturbation, ablator material would eclipse the hotspot boundary and degrade the capsule performance.

Chapter 7

Conclusions

In this dissertation we studied the growth of hydrodynamic instabilities and the resulting mix during the ICF implosion process. We focused on whether the current modeling of the RT and RM instabilities could be improved with the use of a front tracking model as has been demonstrated for pure hydrodynamic instabilities of these types. To accomplish this we used the University of Chicago code FLASH and coupled in a front tracking algorithm through the use of an API (`http://fti.ams.stonybrook.edu/FTAPI.html`). With the addition of front tracking we compared on/off simulations in both one and two dimensions using a spherical geometry.

We found that the main benefit of front tracking lies in the enhanced numerics, whereas the typical numerical diffusion observed on Eulerian grids at steep concentration gradients are removed as a design feature in the front tracking algorithm. The numerical diffusion observed in the base FLASH simulations, without the use of front tracking was shown to be near an instability cliff, where if it penetrated too much it would get caught up in the strong RT instability and mixed inwards. At reasonable computational grids for 3D simulations, the observed numerical diffusion was large enough that this occurred in the 2D simulations.

Additional observations were that a latent acceleration during the RM phase led to a stabilization effect at the outer fuel-ablator interface and only with the impact of a stronger than nominal perturbation at the ice-gas interface was enhanced mixing able to be realized.

This emphasizes a strongly coupled effect between the inner ice-gas boundary and the strong thermal gradient that develops at the edge of the hot spot and is the main driver for RT deceleration phase growth.

As a result of the major growth occurring in the inner regions of the capsule, we found limited impact on the bang time thermodynamics due to tracking at the fuel-ablator interface. In 1D simulations, we added a mass diffusion model on top of the front tracking algorithm to model a physically consistent diffusion of ablator material and found that this had little to no effect. This emphasizes the importance of the numerical improvement of front tracking, preventing a qualitatively incorrect solution from numerical diffusion.

We also considered a buoyancy-drag model based on 1D simulation data to predict the spike penetration of ablator material into the hotspot. We coupled the model into the late time deceleration phase simulations to dynamically calculate local accelerations and Atwood numbers and the predicted mixing front. This model was compared to the 2D simulation data to determine the efficacy of this model typically used for standard RM and RT instabilities for the ICF regime studied here and found to have reasonable predictive capabilities but not perfect agreement, which we largely attribute to spherical effects not included in the buoyancy-drag model used. The model was used to analyze trajectories of ablator material that would be needed to contaminate the hotspot. This suggested that the NIC design is near a performance cliff where small perturbations in the as designed specifications or coupling effects between various instabilities drivers could cause the NIC low foot capsules to allow ablator material to enter the hot spot near bang time.

To expand on these studies, we enumerate a few outstanding questions.

1. We observed a slight suppression of the bang time instabilities with the use of front tracking which could be a mesh refinement effect, where the front tracking simulation is able to achieve a better converged solution than the companion untracked solution. Further studies with refinement in the F-BASE simulations would be necessary to fully investigate that phenomenon.

2. We observed little to no impact with the use of a physical mass diffusion model applicable to the ICF regime. A full sensitivity to mass diffusion as well as other physical transport quantities such as viscosity and thermal conduction is the focus of ongoing work, with the hopes of fully confirming the hypothesis that only thermal conduction plays an important role in the physics of ICF [73].

3. Our simulations here tracked only the outer fuel-ablator interface where little growth was observed. The impact of front tracking at the late time thermal gradient or the interior ice-gas interface is still an open question.

4. Lastly, our simulations only modeled from the RM phase onwards, missing out on any seeded instability growth from laser inhomogeneities and ablation front RT instabilities. There is experimental evidence [60] to suggest that these are a leading candidate for ablator mix into the hot spot and thus extended simulations or theoretical analysis that includes an effect based on these earlier instabilities would be of interest.

Bibliography

[1] P. Amendt, O. Landen, H. Robey, C. Li, and R. Petrasso, *Plasma barodiffusion in inertial-confinement-fusion implosions: Application to observed yield anomalies in thermonuclear fuel mixtures*, Physical Review Letters, 105 (2010), 115005.

[2] J. Bell, M. Berger, J. Saltzman, and M. Welcome, *Three-dimensional adaptive mesh refinement for hyperbolic conservation laws*, SIAM Journal on Scientific Computing, 15 (1994), pp. 127–138.

[3] R. Betti, M. Umansky, V. Lobatchev, V. N. Goncharov, and R. L. McCrory, *Hot-spot dynamics and deceleration-phase Rayleigh-Taylor instability of imploding inertial confinement fusion capsules*, Physics of Plasmas, 8 (2001), pp. 5257–5267.

[4] W. Bo, X. Liu, J. Glimm, and X. Li, *A robust front tracking method: Verification and application to simulation of the primary breakup of a liquid jet*, SIAM J. Sci. Comput., 33 (2011), pp. 1505–1524.

[5] T. R. Boehly, D. Munro, P. M. Celliers, R. E. Olson, D. G. Hicks, V. N. Goncharov, G. W. Collins, H. F. Robey, S. X. Hu, J. A. Morozas, T. C. Sangster, O. L. Landen, and D. D. Meyerhofer, *Demonstration of the shock-timing technique for ignition targets on the National Ignition Facility*, Physics of Plasmas, 16 (2009), 056302.

[6] M. Brouillette, *The Richtmyer-Meshkov instability*, Annual Review of Fluid Mechanics, 34 (2002), pp. 445–468.

[7] A. Casner, V. Smalyuk, L. Masse, A. Moore, B. Delorme, D. Martinez, I. Igumenshev, L. Jacquet, S. Liberatore, R. Seugling, C. Chicanne, H. Park, and B. Remington, *Design and implementation plan for indirect-drive highly nonlinear ablative RayleighTaylor instability experiments on the National Ignition Facility*, High Energy Density Physics, 9 (2013), pp. 32 – 37.

[8] C. Cerjan, P. T. Springer, and S. M. Sepke, *Integrated diagnostic analysis of inertial confinement fusion capsule performance*, Physics of Plasmas, 20 (2013), 056319.

[9] B. Cheng, J. Glimm, and D. H. Sharp, *Density dependence of Rayleigh-Taylor and Richtmyer-Meshkov mixing fronts*, Phys. Lett. A, 268 (2000), pp. 366–374.

[10] B. Cheng, J. Glimm, and D. H. Sharp, *Dynamical evolution of the Rayleigh-Taylor and Richtmyer-Meshkov mixing fronts*, Phys. Rev. E, 66 (2002), pp. 1–7.

[11] B. Cheng, T. Kwan, Y.-M. Wang, and S. Batha, *Scaling laws for ignition at the National Ignition Facility from first principles*, Phys. Rev. E, 88 (2013), 041101.

[12] B. Cheng, T. Kwan, D. Wilson, Y. Wang, and S. Batha, *Effects of instabilities and adiabat in NIF experiments*. 14th International Workshop on the Physics of Compressible Turbulent Mixing, 2014.

[13] B. Cheng, T. J. T. Kwan, Y.-M. Wang, and S. H. Batha, *On thermonuclear ignition criterion at the National Ignition Facility*, Physics of Plasmas, 21 (2014), 102707.

[14] B. Cheng, T. J. T. Kwan, Y.-M. Wang, F. E. Merrill, C. J. Cerjan, and S. H. Batha, *Analysis of NIF experiments with the minimal energy implosion model*, Physics of Plasmas, 22 (2015), 082704.

[15] I.-L. Chern, J. Glimm, O. McBryan, B. Plohr, and S. Yaniv, *Front tracking for gas dynamics*, J. Comput. Phys., 62 (1986), pp. 83–110.

[16] D. S. Clark, S. W. Haan, and J. D. Salmonson, *Robustness studies of ignition targets for the National Ignition Facility in two dimensions*, Physics of Plasmas, 15 (2008), 056305.

[17] D. S. Clark, D. E. Hinkel, D. C. Eder, O. S. Jones, S. W. Haan, B. A. Hammel, M. M. Marinak, J. L. Milovich, H. F. Robey, L. J. Suter, and R. P. J. Town, *Detailed implosion modeling of deuterium-tritium layered experiments on the National Ignition Facility*, Physics of Plasmas, 20 (2013), 056318.

[18] D. S. Clark, M. M. Marinak, C. R. Weber, D. C. Eder, S. W. Haan, B. A. Hammel, D. E. Hinkel, O. S. Jones, J. L. Milovich, P. K. Patel, H. F. Robey, J. D. Salmonson, S. M. Sepke, and C. A. Thomas, *Radiation hydrodynamics modeling of the highest compression inertial confinement fusion ignition experiment from the National Ignition Campaign*, Physics of Plasmas, 22 (2015), 022703.

[19] P. Colella and H. M. Glaz, *Efficient solution algorithms for the Riemann problem for real gases*, Journal of Computational Physics, 59 (1985), pp. 264 – 289.

[20] J. P. Dahlburg, D. E. Fyfe, J. H. Gardner, S. W. Haan, S. E. Bodner, and G. D. Doolen, *Three-dimensional multimode simulations of the ablative Rayleigh-taylor instability*, Physics of Plasmas, 2 (1995), pp. 2453–2459.

[21] J. Daligault, *Practical model for the self-diffusion coefficient in Yukawa one-component plasmas*, Phys. Rev. E, 86 (2012), 047401.

[22] G. Dimonte, D. L. Youngs, A. Dimits, S. Weber, M. Marinak, S. Wunsch, C. Garasi, A. Robinson, M. J. Andrews, P. Ramaprabhu, A. C. Calder, B. Fryxell, J. Biello, L. Dursi, P. MacNeice, K. Olson, P. Ricker, R. Rosner, F. Timmes, H. Tufo, Y.-N. Young, and M. Zingale, *A comparative study of*

the turbulent Rayleigh-Taylor instability using high-resolution three-dimensional numerical simulations: The Alpha-Group collaboration, Physics of Fluids, 16 (2004), pp. 1668–1693.

[23] B. Fryxell, K. Olson, P. Ricker, F. X. Timmes, M. Zingale, D. Q. Lamb, P. MacNeice, R. Rosner, J. W. Truran, and H. Tufo, *FLASH: An adaptive mesh hydrodynamics code for modeling astrophysical thermonuclear flashes*, Astrophysical Journal, Supplement, 131 (2000), p. 273.

[24] E. George and J. Glimm, *Self similarity of Rayleigh-Taylor mixing rates*, Phys. Fluids, 17 (2005), pp. 1–13. Stony Brook University Preprint SUNYSB-AMS-04-05.

[25] M. Gittings, R. Weaver, M. Clover, T. Betlach, N. Byrne, R. Coker, E. Dendy, R. Hueckstaedt, K. New, W. R. Oakes, D. Ranta, and R. Stefan, *The RAGE radiation-hydrodynamic code*, Computational Science & Discovery, 1 (2008), 015005.

[26] J. Glimm, M. Graham, J. Grove, X. Li, T. Smith, D. Tan, F. Tangerman, and Q. Zhang, *Front tracking in two and three dimensions*, Computers & Mathematics with Applications, 35 (1998), pp. 1 – 11.

[27] J. Glimm, D. H. Sharp, T. Kaman, and H. Lim, *New directions for Rayleigh-Taylor mixing*, Phil. Trans. R. Soc. A, 371 (2013), 20120183.

[28] W. Goldstein and R. Rosner, *Workshop on the science of fusion ignition on NIF*, LLNL Rep. No. LLNL-TR-570412, Lawrence Livermore National Laboratory, 2012.

[29] S. W. Haan, J. D. Lindl, D. A. Callahan, D. S. Clark, J. D. Salmonson, B. A. Hammel, L. J. Atherton, R. C. Cook, M. J. Edwards, S. Glenzer, A. V. Hamza, S. P. Hatchett, M. C. Herrmann, D. E. Hinkel, D. D. Ho, H. Huang, O. S. Jones, J. Kline, G. Kyrala, O. L. Landen, B. J. MacGowan, M. M. Marinak, D. D. Meyerhofer, J. L. Milovich, K. A. Moreno, E. I. Moses, D. H. Munro, A. Nikroo, R. E. Olson, K. Peterson, S. M. Pollaine, J. E. Ralph, H. F. Robey, B. K. Spears, P. T. Springer, L. J. Suter, C. A. Thomas, R. P. Town, R. Vesey, S. V. Weber, H. L. Wilkens, and D. C. Wilson, *Point design targets, specifications, and requirements for the 2010 ignition campaign on the National Ignition Facility*, Physics of Plasmas, 18 (2011), 051001.

[30] J. D. Hager, *Rayleigh-Taylor Experiments in Materials and Conditions Relevant to Ignition in Inertial Confinement Fusion*, PhD thesis, University of Rochester, 2011.

[31] B. M. Haines, F. F. Grinstein, and J. R. Fincke, *Three-dimensional simulation strategy to determine the effects of turbulent mixing on inertial-confinement-fusion capsule performance*, Phys. Rev. E, 89 (2014), 053302.

[32] M. C. Herrmann, M. Tabak, and J. D. Lindl, *A generalized scaling law for the ignition energy of inertial confinement fusion capsules*, Nucl. Fusion, 41 (2001), p. 99.

[33] D. G. Hicks, B. K. Spears, D. G. Braun, R. E. Olson, C. M. Sorce, P. M. Celliers, G. W. Collins, and O. L. Landen, *Convergent ablator performance measurements*, Physics of Plasmas, 17 (2010), 102703.

[34] C.-S. Huang, M. C. Kelley, and D. L. Hysell, *Nonlinear Rayleigh-Taylor instabilities, atmospheric gravity waves and equatorial spread*, Journal of Geophysical Research: Space Physics, 98 (1993), pp. 15631–15642.

[35] O. Jones, R. Rygg, R. Tomasini, D. Eder, A. Kritcher, J. Milovich, L. Peterson, C. Thomas, M. Barrios, R. Benedetti, T. Doeppner, T. Ma, S. Nagel, A. Pak, J. Field, N. Izumi, S. Glenn, R. Town, and D. Bradley, *A new symmetry model for hohlraum-driven capsule implosion experiments on the NIF*, Journal of Physics: Conference Series, 688 (2016), 012042.

[36] T. Kaman, *Rayleigh-Taylor Turbulent Mixing Simulations*, PhD thesis, Stony Brook University, 2012.

[37] J. Kane, R. P. Drake, and B. A. Remington, *An evaluation of the Richtmyer-Meshkov instability in supernova remnant formation*, The Astrophysical Journal, 511 (1999), p. 335.

[38] R. Kaufman, *Software Tools for Stochastic Simulations of Turbulence*, PhD thesis, State University of New York at Stony Brook, 2014.

[39] R. Kaufman, H. Lim, and J. Glimm, *Conservative front tracking: the algorithm, the rationale and the API*, Bulletin of the Institute of Mathematics, Academia Sinica New Series, 11 (2016), pp. 115–130.

[40] Y. T. Lee and R. M. More, *An electron conductivity model for dense plasmas*, Physics of Fluids, 27 (1984), pp. 1273–1286.

[41] H. Lim, J. Iwerks, J. Glimm, and D. H. Sharp, *Nonideal Rayleigh-Taylor mixing*, PNAS, 107(29) (2010), pp. 12786–12792.

[42] J. Lindl, *Development of the indirect-drive approach to inertial confinement fusion and the target physics basis for ignition and gain*, Physics of Plasmas, 2 (1995), pp. 3933–4.

[43] J. Lindl, O. Landen, J. Edwards, E. Moses, and N. Team, *Review of the National Ignition Campaign 2009-2012*, Physics of Plasmas, 21 (2014), 020501.

[44] J. D. Lindl, P. Amendt, R. L. Berger, S. G. Glendinning, S. H. Glenzer, S. W. Haan, R. L. Kauffman, O. L. Landen, and L. J. Suter, *The physics basis for ignition using indirect-drive targets on the National Ignition Facility*, Physics of Plasmas, 11 (2004), pp. 339–491.

[45] Lord Rayleigh, *Investigation of the character of the equilibrium of an incompressible heavy fluid of variable density*, in Scientific Papers, vol. II, Cambridge Univ. Press, Cambridge, England, 1900, p. 200.

[46] S. P. Lyon and J. D. Johnson, *SESAME: The Los Alamos National Laboratory equation of state database*, LANL Rep. No. LA-UR-92-3407, Los Alamos National Laboratory, 1992.

[47] N. H. Magee, J. Abdallah, Jr., R. E. H. Clark, J. S. Cohen, L. A. Collins, G. Csanak, C. J. Fontes, A. Gauger, J. J. Keady, D. P. Kilcrease, and A. L. Merts, *Atomic Structure Calculations and New Los Alamos Astrophysical Opacities*, in Astrophysical Applications of Powerful New Databases, S. J. Adelman and W. L. Wiese, eds., vol. 78 of Astronomical Society of the Pacific Conference Series, 1995, p. 51.

[48] M. M. Marinak, G. D. Kerbel, N. A. Gentile, O. Jones, D. Munro, S. Pollaine, T. R. Dittrich, and S. W. Haan, *Three-dimensional HYDRA simulations of National Ignition Facility targets*, Physics of Plasmas, 8 (2001), pp. 2275–2280.

[49] J. Melvin, H. Lim, V. Rana, B. Cheng, J. Glimm, D. H. Sharp, and D. C. Wilson, *Sensitivity of inertial confinement fusion hot spot properties to the deuterium-tritium fuel adiabat*, Physics of Plasmas, 22 (2015), 022708.

[50] E. E. Meshkov, *Instability of the interface of two gases accelerated by a shock wave*, Fluid Dynamics, 4 (1969), pp. 101–104.

[51] D. Mihalas and B. Mihalas, *Foundations of Radiation Hydrodynamics*, Oxford Univ. Press, New York, 1984.

[52] K. Molvig, E. Vold, E. Dodd, and S. Wilks, *Nonlinear structure of the diffusing gas-metal interface in a thermonuclear plasma*, Physical Review Letters, 113 (2014), 145001.

[53] R. M. More, K. H. Warren, D. A. Young, and G. B. Zimmerman, *A new quotidian equation of state (QEOS) for hot dense matter*, Physics of Fluids, 31 (1988), pp. 3059–3078.

[54] R. V. Morgan, R. Aure, J. D. Stockero, J. A. Greenough, W. Cabot, O. A. Likhachev, and J. W. Jacobs, *On the late-time growth of the two-dimensional Richtmyer-Meshkov instability in shock tube experiments*, Journal of Fluid Mechanics, 712 (2012), pp. 354–383.

[55] W. Noh and P. Woodward, *SLIC (simple line interface calculation)*, in Lecture Notes in Physics, Proceedings of the Fifth International Conference on Numerical Methods for Fluid Dynamics, A. I. van de Vooren and P. J. Zandbergen, eds., vol. 59, Springer-Verlag, New York, 1976, pp. 330–340.

[56] J. H. Nuckolls, *Early steps toward inertial fusion energy (IFE) (1952 to 1962)*, LLNL Rep. No. UCRL-ID-131075, Lawrence Livermore National Laboratory, 1998.

[57] D. Oron, L. Arazi, D. Kartoon, A. Rikanati, U. Alon, and D. Shvarts, *Dimensionality dependence of the Rayleigh-Taylor and Richtmyer-Meshkov instability late-time scaling laws*, Physics of Plasmas, 8 (2001), pp. 2883–2889.

[58] H. S. Park, O. A. Hurricane, D. A. Callahan, D. T. Casey, E. L. Dewald, T. R. Dittrich, T. Doppner, D. E. Hinkel, L. F. B. Hopkins, S. L. Paper, T. Ma, P. K. Patel, B. A. Remington, H. F. Robey, and J. D. Salmonson, *High-adiabat high-foot inertial confinement fusion implosion experiments on the National Ignition Facility*, Physical Review Letters, 112 (2014), 055001.

[59] V. Rana, H. Lim, J. Melvin, B. Cheng, and D. H. Sharp, *Length scales for turbulent mixing with applications to ICF implosions*, Phys. Rev. E, (2016). LANL preprint LA-UR-12-21555; Submitted.

[60] B. A. Remington, L. J. Atherton, L. R. Benedetti, L. Berzak-Hopkins, D. K. Bradley, D. A. Callahan, D. Casey, P. M. Celliers, C. J. Cerjan, D. S. Clark, E. L. Dewald, T. R. Dittrich, S. N. Dixit, T. Dppner, D. H. Edgell, M. J. Edwards, R. Epstein, J. Frenje, M. Gatu-Johnson, S. Glenn, S. H. Glenzer, G. Grim, S. W. Haan, B. A. Hammel, A. Hamza, D. Hicks, W. W. Hsing, O. Hurricane, N. Izumi, O. S. Jones, M. H. Key, S. F. Khan, J. D. Kilkenny, J. L. Kline, G. A. Kyrala, O. L. Landen, S. L. Pape, J. D. Lindl, T. Ma, B. J. MacGowan, A. J. Mackinnon, A. G. MacPhee, N. B. Meezan, J. D. Moody, E. I. Moses, A. Nikroo, A. Pak, T. Parham, H.-S. Park, P. K. Patel, R. Petrasso, J. Pino, J. Ralph, K. Raman, S. P. Regan, H. F. Robey, J. S. Ross, B. K. Spears, V. A. Smalyuk, P. T. Springer, L. J. Suter, R. Tipton, R. Tommasini, R. P. Town, and S. V. Weber, *Hydrodynamic instabilities and mix studies on NIF: predictions, observations, and a path forward*, Journal of Physics: Conference Series, 688 (2016), 012090.

[61] R. D. Richtmyer, *Taylor instability in shock acceleration of compressible fluids*, Comm. Pure Appl. Math., 13 (1960), pp. 297–319.

[62] J. R. Rygg, O. S. Jones, J. E. Field, M. A. Barrios, L. R. Benedetti, G. W. Collins, D. C. Eder, M. J. Edwards, J. L. Kline, J. J. Kroll, O. L. Landen, T. Ma, A. Pak, J. L. Peterson, K. Raman, R. P. J. Town, and D. K. Bradley, *2d x-ray radiography of imploding capsules at the National Ignition Facility*, Phys. Rev. Lett., 112 (2014), 195001.

[63] Y. Saillard, in Proceedings of Inertial Fusion Sciences and Applications 2001, Paris, 2002, Elsevier, pp. 192–196.

[64] J. Sanz, J. Garrier, C. Cherfils, B. Canaud, L. Masse, and M. Temporal, *Self-consistent analysis of the hot spot dynamics for inertial confinement fusion capsules*, Phys of Plasmas, 12 (2005), 112702.

[65] D. H. Sharp, *An overview of Rayleigh-Taylor instability*, Physica D, 12 (1984), pp. 3–18.

[66] D. She, R. Kaufman, H. Lim, J. Melvin, A. Hsu, and J. Glimm, *Front tracking methods*, preprint submitted to Elsevier, (2016).

[67] G. Sod, *A survey of several finite difference methods for systems of nonlinear hyperbolic conservation laws*, J. Comput. Phys., 27 (1978), p. 1.

[68] J. M. Stone and T. Gardiner, *The magnetic Rayleigh-Taylor instability in three dimensions*, The Astrophysical Journal, 671 (2007), p. 1726.

[69] H. Takabe and A. Yamamoto, *Reduction of turbulent mixing at the ablation front of fusion targets*, Phys. Rev. A, 44 (1991), pp. 5142–5149.

[70] G. I. Taylor, *The instability of liquid surfaces when accelerated in a direction perpendicular to their planes I*, Proc. R Soc. London A, 201 (1950), pp. 192–196.

[71] B. Thornber, D. Drikakis, D. L. Youngs, and R. J. R. Williams, *The influence of initial conditions on turbulent mixing due to Richtmyer-Meshkov instability*, Journal of Fluid Mechanics, 654 (2010), pp. 99–139.

[72] E. L. Vold, A. S. Joglekar, M. I. Ortega, R. Moll, D. Fenn, and K. Molvig, *Plasma viscosity with mass transport in spherical inertial confinement fusion implosion simulations*, Physics of Plasmas, 22 (2015), 112708.

[73] C. R. Weber, D. S. Clark, A. W. Cook, D. C. Eder, S. W. Haan, B. A. Hammel, D. E. Hinkel, O. S. Jones, M. M. Marinak, J. L. Milovich, P. K. Patel, H. F. Robey, J. D. Salmonson, S. M. Sepke, and C. A. Thomas, *Three-dimensional hydrodynamics of the deceleration stage in inertial confinement fusion*, Physics of Plasmas, 22 (2015), 032702.

[74] C. R. Weber, D. S. Clark, D. Cook, L. E. Busby, and H. F. Robey, *Inhibition of turbulence in inertial-confinement-fusion hotspots by viscous dissipation*, Phys Rev E, 89 (2014), 053106.

[75] Q. Yang, J. Chang, and W. Bao, *Richtmyer-Meshkov instability induced mixing enhancement in the scramjet combustor with a central strut*, Adv. in Mech. Eng., 6 (2014), 614187.